2018

3D printing approaches for guiding endothelial cell vascularization and migration

BOSTON UNIVERSITY

COLLEGE OF ENGINEERING

Dissertation

3D PRINTING APPROACHES FOR GUIDING ENDOTHELIAL CELL VASCULARIZATION AND MIGRATION

by

DANIEL CHENG

B.S., Brown University, 2010
M.S., Boston University, 2016

Submitted in partial fulfillment of the

requirements for the degree of

Doctor of Philosophy

2018

Approved by

First Reader

Christopher S. Chen, M.D., Ph.D.
Professor of Biomedical Engineering
Professor of Materials Science and Engineering
Boston University, College of Engineering

Wyss Institute for Biologically Inspired Engineering
Harvard University

Second Reader

Alice E. White, Ph.D.
Professor and Chair of Mechanical Engineering
Professor of Materials Science and Engineering
Professor of Biomedical Engineering

Third Reader

Joyce Y. Wong, Ph.D.
Professor of Biomedical Engineering
Professor of Materials Science and Engineering

Fourth Reader

Darren Roblyer, Ph.D.
Assistant Professor of Biomedical Engineering

Fifth Reader

Jagesh V. Shah, Ph.D.
Associate Professor of Health Sciences and Technology
Associate Professor of Medicine
Associate Professor of Systems Biology
Harvard Medical School

Assistant Professor, Renal Division
Brigham And Women's Hospital

DEDICATION

I dedicate this work to my mother and father, Carin and Philip Cheng.

ACKNOWLEDGMENTS

I would like to thank all those who have aided me in any way toward the writing of this dissertation. My advisor Chris Chen, for his mentorship, advice, and for fostering a stimulating research environment and lab culture. Jordan Miller, for mentoring me when I first joined the lab and for making me interested and excited about our work. Jeroen Eckymans, for advising and guiding my research, and for helping with writing. Rachael Jayne, Alessio Tamborini, and Greco Song for collaborating and helping with experiments. All the Chen lab members for scientific support and for creating a great and friendly work environment. Meghan Thommes for all her support, both academically and personally.

3D PRINTING APPROACHES FOR GUIDING ENDOTHELIAL CELL VASCULARIZATION AND MIGRATION

DANIEL CHENG

Boston University College of Engineering, 2018

Major Professor: Christopher S. Chen, M.D., Ph.D., Professor of Biomedical Engineering, Professor of Materials Science and Engineering, Boston University, College of Engineering; Wyss Institute for Biologically Inspired Engineering, Harvard University

ABSTRACT

3D printing technology is rapidly advancing and is being increasingly used for biological applications. The spatial control of 3D printing makes it especially attractive for fabricating 3D tissues and for studying the role of geometry in biology. We utilized two different types of 3D printing to engineer vascularized tissues with complex vascular architectures, to use engineered vasculature to treat ischemia, and to study directional endothelial cell migration on curved wave topography.

To engineer 3D tissues, perfusable vascular networks must be embedded within the tissue to supply nutrients and oxygen to cells. 3D-printed sugar filaments have previously been used as a cytocompatible sacrificial template to rapidly cast vascular networks. We improved upon the 3D-printed sugar method and used it to fabricate complex vascular geometries that were not previously possible, such as a branched channel geometry, with controlled fluid flow through the channels. We also integrated an approach utilizing vascular self-assembly to generate thick tissues with dense, capillary-scale vessel networks. The vascularized tissues fabricated using 3D-printed sugar successfully integrated with a host vasculature upon implantation and restored perfusion

in two different animal models of ischemia.

Cell migration critical to numerous biological processes can be guided by surface topography. However, fabrication limitations constrain topography studies to geometries that may not adequately mimic physiological environments. Direct Laser Writing (DLW) provides the necessary 3D flexibility and control to create well-defined curved waveforms similar to those found in physiological settings, such as the lumen of blood vessels. We found that endothelial cells migrated fastest along square waves, intermediate along triangular waves, and slowest along sine waves and that directional cell migration on sine waves decreased at longer sinusoid wavelengths. Interestingly, inhibition of Rac1 decreased directional migration on 3D sine waves but not on 2D micropatterned lines, suggesting that cells may utilize different molecular pathways to sense curved topographies. Our study demonstrates that DLW can be employed to investigate directional migration on a wide array of surfaces with curvatures that are unattainable using conventional manufacturing techniques.

TABLE OF CONTENTS

LIST OF TABLES

LIST OF FIGURES

LIST OF ABBREVIATIONS

ADSC ..... Adipose Derived Stem Cell

CAD ..... Computer-Aided Design

DLW ..... Direct Laser Writing

EC ..... Endothelial Cell

ECM ..... Extracellular Matrix

FA ..... Focal Adhesion

FAK ..... Focal Adhesion Kinase

FGF ..... Fibroblast Growth Factor

FN ..... Fibronectin

HLF ..... Human Lung Fibroblast

hNDF ..... Human Neonatal Dermal Fibroblast

HUVEC ..... Human Umbilical Vein Endothelial Cell

MII ..... Myosin II

MLCK ..... Myosin Light Chain Kinase

MSC ..... Mesenchymal Stem Cell

NMMII ..... Non-Muscle Myosin II

PCL ..... Polycaprolactone

PDLGA ..... Poly(d-lactide-co-glycolide)

PDMS ..... Poly(dimethylsiloxane)

PI3k ..... Phosphoinositide 3-kinase

VEGF ..... Vascular Endothelial Growth Factor

CHAPTER ONE: Introduction

1.1: 3D-Printing for biological applications

3D printing technology has developed rapidly over the past decade causing its usage in a wide range of industries including biomedical research and development to increase. 3D printing enables the rapid prototyping and iteration of complex 3D designs that are difficult or impossible to make using conventional manufacturing approaches. The term 3D printing typically refers to additive layer-by-layer manufacturing, and encompasses a number of different fabrication techniques. Print structures are typically programmed using computer-aided-design (CAD) programs that are then converted to machine code to control movement of the 3D printer.

Two major types of 3D printing are either extrusion-based or stereolithography-based printing. In extrusion-based systems, a computer controls the extruder movement within a 3D volume to deposit an exudate, or ink, layer-by-layer to form a 3D structure. In stereolithography, a laser is focused into a volume of photocurable material, causing the selective volume of material to undergo crosslinking and polymerize into a solid, termed a voxel. The laser focal spot is then moved throughout the photoresist to form a connected solid structure. Both types of 3D printing are able to produce more complex structures at higher resolution as 3D printing technology and printing materials advance.

3D printing is particularly attractive for biomedical research and medical device design because it offers precise control over the spatial placement of materials or cells. 3D printing has already seen commercial and clinical use in the fabrication of medical

devices and has increasingly been used by research groups for tissue engineering applications incorporating live cells.[1] 3D printing has also been used to create 3D *in vitro* platforms for studying cell biology in a more physiologically accurate environment, and is especially conducive to studying the effects of varying 3D geometries. An increasing amount of research shows that cells behave differently in a 3D environment, yet a great deal of biological studies have been conducted in 2D settings. 3D printing and other fabrication technologies are enabling *in vitro* biological studies that more closely mimic the natural *in vivo* environment that cells experience.

The goal of the tissue engineering field is to create tissues, and eventually organs, that can be implanted in a patient to replace a diseased or damaged tissue and restore normal function. Organs contain complex 3D structures composed of multiple cell types whose functional interplay is still not well understood. Engineered tissues may not need to fully mimic the structure of native tissues, but they will need to at least provide some basic functional improvement over the dysfunctional tissue they are meant to replace. 3D printing is an attractive approach towards the long-term tissue engineering goal, but as of now can only build relatively simple tissues lacking much of the complex multi-cellular architecture present *in vitro.* Of particular interest to the medical field, CAD models generated using medical imaging technology such as computed tomography (CT) can be used with 3D printing to customize print architectures specific to an individual patient's anatomy. The rapid and precise fabrication and the customization of print geometries make 3D printing a promising technology for personalized medicine and for the generation of tissues or organs to replace diseased or damaged tissue. As 3D printing

technologies continue to advance and become more commercially available, it may see increasing use for both *in vitro* and *in vivo* studies of biology.

1.2 Vascular tissue engineering

The vascular system supplies the necessary nutrients and oxygen critical to the survival of all cells in living tissues. The vasculature is composed of branching networks of blood vessels lined with endothelial cells through which blood is pumped. The formation and maintenance of complex blood vessel architectures is governed by the migration of endothelial cells during development. Endothelial cells form a monolayer of cells lining blood vessels that acts as a non-thrombogenic and semi-selective barrier between the blood in the vessel and the outside tissue. Permeability of the endothelial monolayer is affected by a number of factors including shear flow of blood in the vessel and the presence of mural cells such as pericytes and smooth muscle cells.[2–4] Vascular permeability modulates diffusion of nutrients, immune cells, and other materials from the bloodstream into the surrounding tissue. Excessive permeability can lead to endothelial cell dysfunction, edema, and swelling. Although different supporting cell types are present in different biological contexts, including smooth muscle cells, pericytes, or fibroblasts, a monolayer of endothelial cells is present in every vessel throughout the body. The vital function and ubiquity of endothelial cells make them a critical focus of research in the field of vascular biology.

A major challenge in the creation of 3D tissues is the construction of perfusable tissues to supply nutrients and oxygen to cells within the tissue and to remove waste

products. Due to diffusion limitations, cells more than a few hundred microns away from perfused vasculature within a tissue will become necrotic.[5] To engineer artificial tissues thicker than the diffusion limit, vascular networks must be embedded throughout the tissue. Thick vascularized tissues are not only desirable to engineer tissue and eventually organ replacements, but can also be used to study cell biology in 3D *in vitro* models that more accurately recapitulate the *in vivo* environment. The ideal goal of vascular tissue engineering is to engineer a vascularized tissue that can supply nutrients to all cells within the tissue volume and can rapidly integrate with a host vasculature upon implantation to establish perfusion.

Aside from tissue replacement applications, engineered vasculature can be used to replace or repair blocked or damaged vasculature in patients with vascular disease or damage. Ischemic cardiovascular disease is a leading cause of mortality worldwide and although it has traditionally been treated through large artery bypass surgery, this treatment cannot restore damaged microvasculature. Thus, engineered vascular constructs that can stimulate vascular regrowth may be useful as an alternate or additional treatment to restore perfusion to more cells throughout a tissue.

The approach to creating 3D vascular networks *in vitro* can generally be categorized as either top-down or bottom-up. The top-down approach is to pre-pattern defined vascular networks before introducing cells while the bottom-up approach is to seed cells in a matrix or scaffold and allow the cells to self-organize into vascular networks. An advantage of the top-down strategy is that the preformed vasculature can immediately supply oxygen and nutrients to surrounding cells, largely mitigating cell

hypoxia and death. Furthermore, studies have shown that a pre-organized vascular architecture may improve vascular integration and anastomoses when implanted in a host.[6] However, current fabrication methods using a top-down approach can be time consuming, especially for larger tissues, and cannot produce vessels at the scale of physiological capillaries, which can be as small as 3 μm.[1] Constraints on the ability to fabricate vessels at the scale and density of physiological capillary networks limit the capability of top down approaches to supply nutrients to cells that are not in close proximity to the pre-fabricated channels.

In the bottom-up approach, cells throughout the tissue can simultaneously self-organize to form a dense capillary-scale vascular network at a fraction of the effort required for top-down patterning. This self-assembled network may eventually attain a sufficient density to reach all cells throughout the tissue, but the networks take days to weeks to form and thus cannot prevent immediate cell death in the core of a cell-laden tissue. Furthermore, self-organized networks lack an overall organizational hierarchy and may not efficiently regulate blood flow in larger tissues.[7] Fabrication technology and our understanding of cell biology is rapidly advancing to meet many of the challenges in vascular tissue engineering, but ultimately a combination of both top-down and bottom-up approaches may be useful to engineer multiscale vascular networks to perfuse large tissues.

1.2.1 Top-down approaches to vascular network formation

A number of groups have fabricated vasculature *in vitro* using soft lithography to generate endothelialized channels in microfluidic devices. Nguyen *et al.* created layers of PDMS that were fixed together to form a mold.[8] Two parallel needles were inserted into the mold and type-I collagen was cast, then the needles were removed to leave open channels in the collagen gel. These channels could be seeded with endothelial cells and were used to study angiogenic sprouting in a 3D *in vitro* platform. Zhang *et al.* used a similar method of layer-by-layer assembly and PDMS molding to create a microfluidic device with a hierarchical branching vessel architecture.[120] Zheng *et al.* used soft lithography to pattern microvessels in collagen gels to study the effects of pericytes on vascular permeability as well as thrombosis in their patterned vessels.[10] Although these models were useful for studying cell biology and biological processes such as angiogenesis or as platforms for drug screening *in vitro,* they are not suitable for tissue engineering applications due to material and scaling constraints.

3D printing has recently seen increasing use in tissue engineering due to its scalability and precise 3D spatial control. To use 3D printing with living cells, researchers must use materials and conditions that are biocompatible and that satisfy the required material properties necessary for printing. Early methods focused on the direct bioprinting of living cells in a suspension of viscous material.[11–18] Although initial attempts often struggled with issues of low cell viability due to cell handling during printing, recent technological advances have significantly improved this process.[19] Kolesky *et al.* were able to directly print human mesenchymal stem cells (hMSCs)

suspended in a gelatin-fibrinogen matrix while retaining high cell viability.[11] Li *et al.* printed rat hepatocytes embedded in a 2:1:1 gelatin:sodium alginate:chitosan solution simultaneously with rat adipose derived stem cells (ADSC) in a 2:1:1 gelatin:alginate:fibrinogen solution.[20] The ADSCs were printed with an open cylinder geometry to form 400 μm diameter channels and were surrounded by a mesh of hepatocytes to model a vascularized liver tissue. However, direct bioprinting using this method could only print vascular channels as cylinders oriented in the vertical direction. It is impossible to print open channels with other geometries or aligned in the horizontal plane that are embedded in larger tissues unless the channels are able to immediately support the weight of the tissue around them or there is some type of support scaffold to prevent channel collapse.

Although direct bioprinting has shown some success, these approaches are limited by printer resolution and the choice of material. Cells must be suspended in a biocompatible material, kept within a controlled temperature range, and the printing process must be limited to prevent cell death from high shear stress or long printing times. Although the direct bioprinting approach may not be suitable for more sensitive cell types or complex vascular structures, it could be used in conjunction with other methods to produce 3D tissues with multiple cell types placed in precise spatial patterns to mimic physiological architectures. Technological advances and the development of new printing materials may also address a number of the current limitations in the future.

A recently developed strategy to generate vascularized tissues is to use a sacrificial material that can be 3D printed in a pre-designed vascular architecture,

encapsulated in some ECM material, and then removed to leave hollow vasculature. This strategy was first demonstrated by Miller *et al.* using 3D-printed sugar-carbohydrate filament networks.[21] Sugar was heated to become molten liquid and extruded from a glass syringe under pneumatic pressure control while a computer-controlled motorized stage spatially controlled the sugar extrusion in 3D to precisely pattern sugar filament geometry. Upon extrusion, the sugar rapidly cooled and hardened, retaining its printed structure. The printed filaments were used as a mold around which to cast an extracellular matrix (ECM) hydrogel, and then the sugar was dissolved and evacuated from the network (Figure 1.1). Once the sugar was removed, the original printed network was left as hollow channels embedded within the ECM. This network was then seeded with endothelial cells that attached to the channel walls to form an endothelialized vascular network. Some of the major benefits of this method were that the sugar was cytocompatible, allowing cells to be seeded in the ECM; that a wide range of natural and synthetic ECM materials could be used for the bulk material; and that vascular network architectures could be controlled through 3D printing. Furthermore, using a sacrificial material avoided the direct printing of cells and reduced cell-handling time which could be detrimental to cell viability. The carbohydrate-glass 3D-printed networks showed efficacy in enhancing the viability of liver hepatocytes seeded within the surrounding ECM at physiologic densities *in vitro*, and have since been directly grafted into a rat circulation to restore perfusion in a hind limb ischemia model.[21,22]

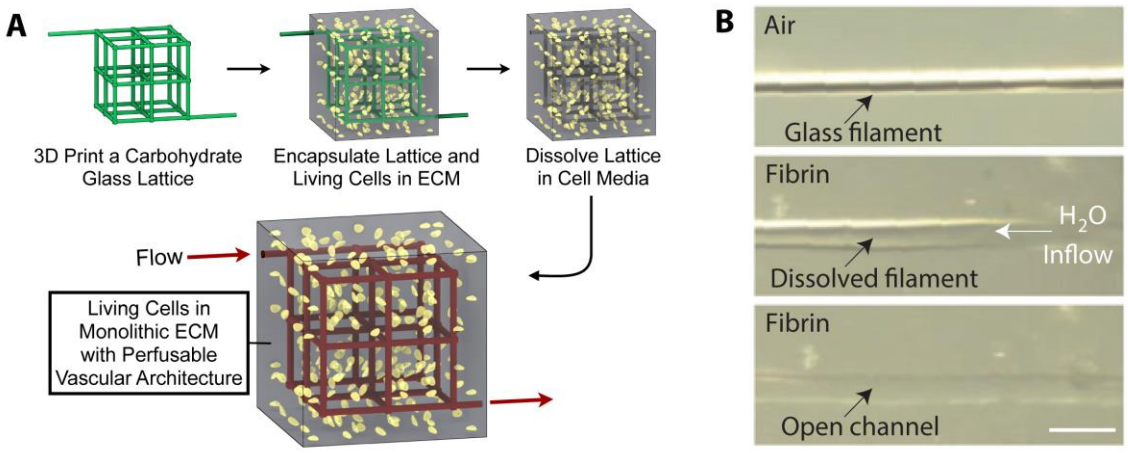

Figure 1.1: **A**) Schematic overview. An open, interconnected, self-supporting carbohydrate-glass lattice is printed to serve as the sacrificial element for the casting of 3D vascular architectures. The lattice is encapsulated in ECM with (or without) living cells. The lattice is dissolved in minutes in cell media without damage to nearby cells. The process yields a monolithic tissue construct with a perfusable vascular architecture that matches the original lattice. **B**) A single carbohydrate-glass fiber (200 µm diameter, top) is encapsulated in a fibrin gel. Following ECM crosslinking, the gel and filament are immersed in aqueous solution and the dissolved carbohydrates are flowed out of the resulting channel (middle). Removal of the filament yields an open perfusable channel in the fibrin gel (bottom, scale bar, 500 µm).[21]

Other groups have used different sacrificial materials to mold vasculature with similar approaches. Bertassoni *et al.* used agarose as a sacrificial molding material to create vessels in photocrosslinkable hydrogels.[23] Abaci *et al.* 3D-printed alginate molds to create vascularized skin constructs that they implanted cutaneously in mice to treat

skin wounds.[24] Kolesky *et al.* utilized Pluronic F-127 which transitioned from a gel to a fluid upon cooling to 4 °C.[11] The printed Pluronic networks were encapsulated within a gelatin-fibrin matrix containing hMSCs and suspended human neonatal dermal fibroblasts (HNDFs) then cooled to remove the sacrificial material leaving hollow 400 μm diameter vascular channels.[25] This process allowed for precise spatial control of multiple cell types that could generate complex tissue architectures, but printing a tissue on the scale of an organ would take multiple days using this method.

One other top-down approach to creating vasculature is the use of photodegradable biomaterials and a spatially-controlled laser to selectively etch away 3D regions of the material, creating perfusable vessel structures. While this approach is able to produce high resolution structures and has shown promise *in vitro*, it is currently limited for translational use by its scalability and the availability of compatible photodegradable biomaterials which could later be used for implantation.[26–28] Aside from the eventual translational potential, top-down approaches enable study of the effect of vascular geometry on the survival and function of cells in 3D tissue constructs. However, the long-term stability and remodeling of prevascularized constructs after implantation remains largely unstudied.

1.2.2 Bottom-up approaches to vascular network formation

Bottom-up approaches to fabricating vasculature predominantly rely on cells' ability to form vasculature through vasculogenesis, the formation of new blood vessels from individual endothelial cells or endothelial progenitor cells. Endothelial cells

randomly seeded throughout a 3D ECM hydrogel will spread and self-assemble with nearby cells into multicellular networks, eventually forming lumenized vessels. It is thought that the lumens form from the fusing of vacuoles as cells join together.[29] This phenomena was first described in 1988 by Kubota *et al.* and has since been found to be modulated by a number of factors including endothelial cell type, ECM material, and the presence of additional supporting cell types in co-culture.[3,30,31] Although the mechanism is not fully understood, fibroblasts[32,33], pericytes[34,35], or MSCs[36] in co-culture with ECs regulate vascular formation and the resultant function of vessels. HUVECs co-cultured with mural cells in a collagen hydrogel form more stable and connected capillary networks than networks composed of endothelial cells alone, an effect that is at least partially due to mural cell production of paracrine factors.[31,37] Chen *et al.* found that HUVECs and fibroblasts randomly seeded in a fibrin gel formed vascular networks and that these prevascularized gels anastomosed and were perfused with blood faster than non-prevascularized gels upon implantation.[38] Other studies have added growth factors, such as vascular endothelial growth factor (VEGF) or fibroblast growth factor (FGF), to stimulate vascular formation.

Recent studies have utilized microfluidic platforms where vasculogenesis is stimulated using either mural cells or growth factors to form vascular networks in an ECM located between microfluidic channels.[32,33,35,36] These microfluidic platforms have the added benefit of patterned microfluidic channels that anastomose to the vasculogenic networks to introduce direct flow into the engineered vasculature. These microfluidic vascular platforms are most useful for *in vitro* studies of cell biology, such as the

mechanisms involved in vasculogenesis and in vessel function, or for assessing drug efficacy and cytotoxicity in a controlled setting. It is difficult to scale the microfluidic devices to create larger tissues, and the PDMS used must be removed if the vascularized tissues are to be implanted, which can be challenging.

The bottom-up approach is able to produce dense vasculature within a time of days or weeks, but the resulting vasculature is unorganized and resembles tumor vasculature more than the hierarchical branching vasculature seen in healthy tissues. Furthermore, a vascular network composed solely of small capillary vessels is inefficient for distributing flow within a tissue.[7] It is not well understood how external cues will guide vascular remodeling in engineered constructs upon implantation but for any engineered vascular networks to survive at all *in vitro*, they must first integrate into the host vasculature and become perfused.

1.2.3 Host-implant vascular integration

Tissues thicker than the diffusion limit must rapidly integrate with the host's vasculature upon implantation to achieve perfusion in order for embedded cells to survive. The engineered vasculature can be connected to the host vasculature either by direct surgical connection or through cell-driven anastomoses induced by the host and/or the implant. Surgical connection is mostly restricted to large-scale vascular grafts such as arteries, as capillary networks are often too small to perform surgery on. Sooppan *et al.* described a surgical technique to directly graft vascularized constructs fabricated using the previously described 3D-printed sacrificial sugar method into a rat femoral artery.[22]

After surgery the engineered constructs became perfused with blood and were able to partially restore perfusion to an ischemic hind limb. Zheng *et al.* were able to surgically anastomose engineered branched vascular networks with rat femoral vessels using surgical cuffs and found that most of the vessels became perfused.[39] Although some larger engineered vessels can be directly sutured into the host, this process is technically difficult and requires materials with strong mechanical properties that are compatible with surgery. Furthermore, surgical connection may not be feasible for treating host tissues that have no larger vessels to connect with.

Rather than surgical anastomoses, microvascular implants have largely relied on vascular integration through natural anastomoses. Levenberg *et al.* found that endothelial cells seeded randomly on a polymer scaffold and transplanted into mice underwent vasculogenesis and formed microvessels that contained mouse blood when explanted, indicating they had anastomosed to the host vasculature.[40] Koike *et al.* found that ECs and fibroblasts seeded together in a collagen gel formed perfused vascular networks within two weeks and survived for a year post-implantation. Notably, implants without the addition of fibroblasts did not become perfused.[41] Although the presence of supporting cells types seems to enhance anastomoses, the precise mechanism remains unclear. Other groups have attempted to promote ingrowth of host vasculature by including pro-angiogenic factors such as VEGF or FGF in the implant.[42,43] However, neither co-culture of supporting cell types or angiogenic factors are able to generate immediate perfusion of the tissue upon implantation and thus may not be sufficient to prevent cell necrosis within the core of thick tissue constructs on their own. Future

studies are needed to better understand what factors affect vascular integration with a host to enhance our ability to generate functional tissue implants.

Recent work by Baranski *et al.* found that endothelial cells patterned into geometrically defined "cords", cylindrical collagen structures with embedded ECs, were able to enhance vascular invasion and integration into a mouse upon implantation. Interestingly, perfusion and functional performance of cells in the cords was dependent on the parallel channel cord geometry, as randomly seeded EC constructs showed significantly decreased perfusion by host blood.[6,44] These results suggest that an organized vascular network fabricated through a top-down approach may enhance implant-host anastomoses and that there may be some optimum geometry for rapid vascular integration.

1.2.4 Effects of flow in the vasculature

Once a prevascularized implant has anastomosed with the host vasculature, flow is introduced into the engineered vessels. Fluid flow in the vascular system has been shown to regulate endothelial cell function including cell morphology, migration, permeability, and thrombogenicity.[4,45,54,46–53] The architecture of the vasculature affects fluid flow and is optimized to minimize cost of construction during development while meeting the diffusion requirements for cells in the surrounding tissue.[7] Vascular geometries such as branches and curved vessels have a higher incidence of atherosclerosis due to disturbed flow patterns leading to endothelial cell dysfunction, however the exact molecular mechanisms involved are not fully understood.[55]

Furthermore, both shear flow and transendothelial interstitial flow have been shown to induce angiogenic sprouting.[50–52,54]

A number of microfluidics platforms have been developed to study the effects of flow *in vitro,* but due to limitations in fabrication or model complexity, some aspects of physiological accuracy must be sacrificed. Many previous *in vitro* models seed cells on 2D substrates or in 3D PDMS microfluidic channels that are much stiffer than native tissues and do not present a porous ECM environment that allows interstitial flow.[56] Furthermore, flow rates are not always well controlled and the rectangular cross sections present in most microfluidics lead to non-physiologic flow profiles.[56] To better understand how engineered tissue will integrate into a host vasculature, more studies of the effects of flow on the function and remodeling of engineered vasculature is needed.

1.2.5 Treatment of ischemia using tissue-engineered vasculature

Although a major focus of vascular tissue engineering is on maintaining the viability of cells within an engineered tissue, there is also a need for treatments to induce revascularization of diseased or damaged tissue *in vivo.* Ischemia is the lack of blood flow to a tissue resulting in inadequate oxygen and nutrient supply, potentially causing tissue necrosis if left untreated. Ischemia can be caused by a number of vascular diseases or trauma leading to vascular occlusion, commonly by thrombi or atherosclerotic plaques.[57] Patients with ischemia are most commonly treated using arterial bypass grafts, but severe cases can necessitate limb amputation.[58] Furthermore, regions of ischemia may not be fully addressable by large-caliber artery grafts and some patients cannot undergo

traditional bypass surgery due to comorbidities.[59] Engineered constructs that stimulate the generation of new blood vessels offer an additional method to treat ischemic patients that could further enhance blood perfusion through the generation of capillary-scale vasculature.

1.3 Effect of 3D environments on cell behavior

Aside from its uses in tissue engineering, 3D printing is also useful for *in vitro* studies of cell biology. Although studies of cells in 2D cell culture have vastly increased our understanding of cell biology, cells behave differently in 3D environments. Cells *in vitro* are embedded in a 3D extracellular matrix (ECM) that presents a number of external chemical and physical cues such as the presence of adhesion ligands or the 3D topography of the ECM. The spatial localization of these cues is significantly different in 3D environments, leading to changes in cell behavior and signaling pathways. Cell shape[60], focal adhesion assembly[60], differentiation[61–64], gene expression[61], and migration[65–67] can all be affected by the physical properties and dimensionality of their extracellular environment. Furthermore, 3D environments drastically change the way cells generate and experience forces and undergo mechanotransduction, which is known to affect a wide array of cell functions.[68,69]

Cells experience a multitude of cues from their external environment, but studying cells *in vivo* is challenging due to difficulty in imaging and monitoring dynamic cellular processes, high variability, and high expense for animal models. In order to explicitly understand cell behavior, researchers have sought to create 3D *in vitro* models

that closely recapitulate specific biological niches. Adhesive, mechanical, and soluble factors can then be more easily controlled and varied to study their effects on cells. *In vitro* models have not only been extremely useful in studying cell biology, but have recently gained usage as more accurate, less costly drug toxicity screening platforms. These "lab-on-a-chip" platforms could provide more accurate results than traditional 2D cell culture at a fraction of the cost of animal studies. 3D *in vitro* models are not only more physiologically accurate, but certain biological phenomena cannot occur in a 2D environment. For example, angiogenesis, the formation of new blood vessels from preexisting vessels, requires a 3D cylindrical vessel from which endothelial cells can sprout to form new lumenized vessels. A variety of different approaches, including 3D printing, have been used to fabricate 3D platforms for studying cell biology.

1.4 Cell migration

Cell migration plays a central role in a large variety of biological processes including early embryonic development, immune cell trafficking and surveillance, angiogenesis and blood vessel remodeling, cancer metastasis, and tissue repair.[70–72] When cells migrate, they typically move over and across ECM, the polymerized fibrous scaffolds that provide the physical structure of our bodies. In order to migrate, cells form protrusions at their leading edge to extend forward in their environment. The protrusions are driven by actin polymerization within the cell and can be either broad lamellopodia or smaller, sharp filopodia. These protrusions form integrin-mediated focal adhesions with the ECM, anchoring the cell to the ECM and allowing it to pull itself forward by

contracting. Adhesions are subsequently disassembled at the cell rear, detaching the cell and allowing the cell body to move forward.[73] This continuous cyclical process of extension, adhesion formation, contraction, and retraction of the trailing edge describes the main process by which cells migrate through their environment.

1.4.1 Directional migration

Directional migration is the ability of cells to persistently move in a single direction or towards a single point, as opposed to random-walk migration. Directional migration allows rapid cell movement between two points that can be both beneficial, as in the directional migration of cells during wound closure, or harmful, as in the case of directed cancer cell migration out of a tumor. A better understanding of the mechanisms driving directional migration will enable us to modulate cell migration and promote the desired outcome.

A number of external cues have been shown to induce directional migration including soluble chemokine gradients (chemotaxis)[74,75], substrate-bound adhesion sites (haptotaxis)[76], substrate stiffness or mechanics (durotaxis)[77], electric fields (electrotaxis)[78], or surface topography (contact guidance)[79]. Although each of the external stimuli are different, in all cases of directional migration, cells become polarized to form a protrusive cell front and a contractile rear that is persistently maintained in a constant direction during migration.

1.4.2 Molecular mechanisms of directional migration

During directional migration, a cell responds to external cues that lead to polarization of the actomyosin cytoskeleton in the cell. This process involves a huge array of molecular pathways in the cell and is still not fully understood, but some of the major molecular components have been established. Three of the major molecular drivers in directional migration are non-muscle myosin II (NMMII), which forms contractile actomyosin bundles at the cell rear and locally inhibits protrusion initiation; phosphoinositide 3-kinase (PI3k), which regulates a number of pathways involved in actin cytoskeletal remodeling in cell migration; and Rac1, which locally concentrates actin polymerization and lamellipodial protrusion to the cell front.[70,80]

1.4.2.1 Myosin

Myosins are motor proteins that are responsible for actin-based motility in cells. Through ATP hydrolysis, myosin generates contractile force along actin filaments to generate movement in the cell. Three functional isoforms of myosin exist: MIIA, MIIB, and MIIC, as defined by their heavy chain isoform. MIIA and MIIB are commonly found in migrating cells and have been shown to promote localized actomyosin bundling at the cell rear to form stable adhesions.[81] In the "molecular clutch" hypothesis of cell motility, myosin II (MII) contractility drives constant retrograde actin flow away from the leading edge of the cell. If integrins on the cell surface form focal adhesions with the ECM, these linking proteins act as a physical anchor between the ECM and the actin cytoskeleton undergoing retrograde flow. When this "molecular clutch" engages with the ECM, the

myosin motors generate traction forces transmitted through the actin cytoskeleton to move the cell within the ECM.[82]

The formation, size, and stability of focal adhesions is also regulated by cell contractility and loss of myosin II contractility results in immediate adhesion disassembly.[83,84] Cell migration speed is dependent on a balance of cell contraction and adhesion and has shown a biphasic response to increasing adhesion strength, with the fastest migration occurring when cells have an intermediate level of adhesion to the ECM.[84] For directional migration to occur, cell protrusion and adhesion to the ECM must be limited to a single persistent direction, or else the cell will generate traction and migration in multiple directions. In motile cells, myosin has been shown to preferentially localize to the rear of the cells but in nonmotile cells it is isotropically distributed, implying the lack of cell motility is due to the isotropic traction force distribution.[85]

1.4.2.2 PI3k

Phosphatidylinositol-4,5-bisphosphate 3-kinase (PI3k) is an enzyme family involved in cell growth, proliferation, differentiation, motility, and survival. PI3k is associated with a number of signaling cascades linking cell-surface receptors to actin cytoskeletal dynamics and cell migration.[80] PI3k has been demonstrated to regulate chemotaxis by recruiting actin filaments to the area of the cell sensing the highest concentration of chemoattractant.[86,87] Neutrophils with inhibited PI3k move more slowly than wild-type cells and have defects in adhesions and actin polarization.[88] Pankov *et al.* found that if PI3k was inhibited in fibroblasts on 2D surfaces, cells lost their ability for

chemotaxis. However, in the absence of a chemoattractant, PI3k inhibition did not affect the directionality of cell migration but did decrease cell migration speed.[89] Directionality" was used to measure the persistent directional migration of cells and was quantified as the linear distance a cell traveled divided by the total distance traversed by the cell. PI3k has also been shown to regulate endothelial cell migration during angiogenesis, the formation of new blood vessels from pre-existing vessels.[87,90] These studies show that PI3k plays an important role in chemotaxis and other cell sensing and directional migration-related pathways.

1.4.2.3 Rac1

Rac1 is a member of the Rho family of GTPases, many of which are involved in actin dynamics, cell protrusions, and migration.[89,91,92] Active Rac1 locally stimulates Arp2/3-mediated actin polymerization to produce lamellar extension and forward migration of the cell.[93] Rac1 colocalizes spatiotemporally with focal adhesion formation at the leading edge of migrating cells as protrusions form and cells migrate forward.[93] Pankov *et al.* found that inhibiting Rac1 in cells on 2D surfaces significantly increased the directionality of migration through a reduction in peripheral lamellae formation, constraining cell migration to persist in the direction of the initial protrusion..[89] Thus, the local restriction of Rac1 activation to the leading edge of the cell leads to cell protrusion, polarization, and persistent directional migration. If Rac1 activity in a cell is either too high or too low it can induce too many or too few cell protrusions respectively, leading to a loss of cell motility.[89,94] Interestingly, MII locally restricts Rac1 activation, limiting cell

protrusions at the rear and periphery of the cell and further establishing cell polarity with a protrusive cell front and a non-protrusive, contractile cell rear.[95]

1.4.3 Effect of dimensionality on cell migration

The molecular mechanisms of directional cell migration may also be affected by the physical properties of the ECM. Interestingly, cells cultured on flat strips of micropatterned fibronectin (FN), a major ECM component, seem to mimic the phenotype and migration speeds of cells in a 3D matrix.[96] As such, a number of studies have used flat FN lines as a simplified model of a 3D fibrillar environment where cell adhesion to the ECM is physically constrained. On flat FN lines, the myosin II inhibitor blebbistatin reduced fibroblast cell migration speed, whereas Rac1 inhibition increased directional migration and migration speed.[89,96] A subsequent study on flat FN lines showed that blebbistatin treatment may inhibit migration by causing a dissociation in the linkage between integrins and focal adhesion proteins, disturbing the ability of the cell to generate traction forces.[83]

Although studies of cells on flat substrates have greatly advanced our understanding of cell migration, cell migration can be substantially altered in a 3D environment and may have different contributing molecular pathways.[97] While cells on 2D surfaces are able to migrate freely into surrounding areas, cells in a 3D matrix must navigate through a porous ECM either through cell deformation or proteolytic cleavage of the surrounding matrix. A 3D environment presents different mechanical properties and different spatial distributions of cell-adhesive ligands, modulating integrin-mediated

cell anchoring sites to the ECM and subsequent cell adhesion and spreading.[98] Furthermore, the molecular composition, structure, and function of cell-matrix adhesions is altered in 3D matrices compared to 2D.[99] Notably, Rac expression decreases for cells in a 3D FN matrix compared to a 2D surface, indicating that dimensionality affects Rac expression.[89] This decrease in Rac activity also corresponded to an increase in directional migration. To advance our understanding of how the 3D ECM affects cell migration, researchers have sought to develop novel biomaterials and simplified *in vitro* models where individual properties of the ECM, such as substrate chemistry, mechanical stiffness, or physical topography, can be independently tuned.

1.5 Contact guidance

Contact guidance describes the phenomenon whereby a physical topography induces the polarization, elongation, and preferential migration of cells in the direction parallel to aligned topography features. Cells' ability to align parallel to a ridge topography was first discovered in 1914, and since then, the presence of contact guidance has been catalogued in a number of cell types including fibroblasts, neurons, osteoblasts, myoblasts, epithelial cells, and endothelial cells.[79,100–102] This effect has also been observed *in vitro* where breast cancer cells actively reorganize collagen fibers surrounding a tumor, creating aligned fiber networks that guide cells to travel outward from the tumor and metastasize into surrounding tissue.[103–105] To study this effect in a more controlled setting, researchers have patterned various topographies to study their effect on cell migration *in vitro*. Modulating cell migration speed and direction using

topography could be valuable for designing biomedical devices where rapid cell repopulation is critical, such as vascular stents where an endothelial cell monolayer is necessary for proper vascular barrier function and prevention of thrombosis. A major advantage of topography as a cellular control mechanism is that it is purely physical and does not change the biochemistry of the implant environment.[106]

1.5.1 Effects of contact guidance on cell alignment

Cells exhibit contact guidance on a wide variety of substrate materials and feature sizes ranging from tens of nanometers to hundreds of microns.[79,107,108] The most predominantly studied type of topography is a square wave or aligned ridge topography. In general, on aligned square waves the degree of cell alignment parallel to the topography increases with shorter wavelengths or increasing amplitude.[100,101,115–123,102,108–114] Fibroblast cells aligned to ridges with an amplitude as small as 35 nm or width as small as 100 nm, similar in size to the width of a single collagen fibril (~30-100 nm), but cells did not align to ridges with dimensions below this threshold.[124] Below this minimum threshold cells may sense an essentially flat surface, and thus did not align to the topography. There also seems to be a maximum threshold for amplitude above which cells no longer sense a difference in topography. The maximum amplitude threshold may be the point where cells can no longer make contact with the troughs of the square wave and may differ depending on cell size or contractility.[125] Increasing square wave width reduces the physical constraint on cell spreading, allowing it to spread in the perpendicular direction. Once the ridge width increases too far beyond the cell width,

cells will only sense a flat surface and thus will spread isotropically.

1.5.2 Effects of contact guidance on cell migration

In studies of cell migration on topographies, cells typically migrated faster on square waves than on flat surfaces.[107,126–128] Cell migration speed generally decreased on longer wavelength square waves, but varying amplitude has given conflicting results for different studies, possibly due to differences in experimental setup or cell type.[107,128] As the square wave width increases, cells elongate less, spread out more, and migrate less directionally. This effect is similar in 2D where Li *et al.* showed that bovine aortic endothelial cells migrated faster on flat collagen strips that were 15 μm wide as compared to 60 or 30 μm wide strips.[128] To study the effect of varying 3D topography dimensions, Kaiser *et al.* fabricated ridges from a titanium alloy and varied ridge width, spacing, and height from 5 to 30 μm. They found that 3T3 fibroblasts migrated fastest on the 5 μm wide patterns but were not able to establish clear trends on the effects of varying the other dimensions due to confounding variables.[129] On patterned flat fibronectin lines with widths ranging from 1 to 40 μm, fibroblast cells migrated fastest on the 2.5 μm wide patterns at 2-3 times the migration speed of cells on flat surfaces.[96] While flat lines are used as a simplified model of topography and the findings generally agree with other studies, it is unclear whether the optimal dimensions for enhancing migration speed are the same in 3D settings or for different cell types.

Recent studies have used newer, often technology-driven, fabrication methods to study the effects of more complex topographies on cells.[106,126,130–132] Using an anisotropic

topography pattern with varying spacing between ridges, Kim *et al.* found that fibroblasts tended to migrate towards the region with an intermediate ridge spacing, and that cells on the intermediate spacing region migrated fastest.[126] This study implies that there may be an ideal dimensionality for topographies to enhance cell migration speed. Further studies by Kim *et al.*, Mai *et al.*, and Jeon *et al.* used anisotropic topographies presenting multidirectional cues in the form of rectangular grid patterns. When presented with rectangular grid geometries, cells tended to align and migrate along the axis of the long side of the rectangle, but did not align if both sides of the rectangle were the same length.[130–132] These studies indicate that cells are able to integrate multidirectional topographical signals and that the aspect ratio of the topographies is important. There have also been a number of studies which have used aligned posts, pillars, or other geometries to study cell adhesion and topography effects.[106,130,141,133–140] Greater understanding of how more complex geometries affect cell migration could inform strategies for optimizing the design of implants or tissue engineering architectures.

1.5.3 Underlying mechanisms of contact guidance

There are two major non-mutually exclusive hypotheses on the underlying mechanism of contact guidance. One is that spacing between aligned features acts as a barrier preventing cells from crossing between ridges. Xia *et al.* patterned FN islands with varying ellipticity (elongation), alignment, and inter-island spacing and found that cells orientated and migrated preferentially in the direction of the smallest interisland spacing as opposed to the direction of elongation of individual elliptical FN islands.[93]

However, elongation of the FN islands did have some effect and the results may not translate to a 3D model. Ray *et al.* patterned topographic ridges with different spacing between the ridges and found that cells no longer aligned when the spacing was five times that of the ridge width.[125] However, cells were able to form focal adhesions within the space between the raised ridges (the troughs), so this result may just be a product of cells spreading on the wider flat surfaces between the ridges. The spacing between ridges does not act as an absolute barrier for cells to cross, but cells' response to topography can be described as a probabilistic reaction that is dependent on topography feature dimensions. If contact guidance were determined only by topography spacing, one would expect that aligned wave topographies with shorter wavelengths would have less cell alignment since cells could more easily cross between ridges to spread in the perpendicular direction. However, cells on shorter wavelengths tend to become more elongated in the parallel direction and less spread in the perpendicular direction instead.

Another hypothesized underlying cause of contact guidance is the regulation of focal adhesion (FA) area by physical topography.[142] FA assembly is initiated by integrin attachment to the appropriate ECM ligands that leads to the recruitment of FA proteins such as paxillin. Blocking integrin attachment eliminates cell alignment and the directional migration of cells on topography.[143,144] FA proteins mechanically link integrins that are anchored to the ECM to the cell's actin cytoskeleton and are critical for force transduction in the cell, including during cell migration.[145] As cells spread and elongate parallel to topography, FAs, actin fibers, and microtubules align within the cell, stabilizing cellular forces along the axis of elongation. Interestingly, Oakley and Brunette

observed that for cells seeded on aligned topographies, microtubules oriented first, followed by actin and lastly FAs.[101]

As FAs mature they elongate, primarily in the direction of actin stress fibers in the cell, allowing them to bear higher cellular tension forces.[102] Balaban *et al.* found that both the FA size (elongation) and shape (ellipticity) were correlated with the magnitude and direction of forces that cells exerted on a surface patterned with a micro-pit topography.[146] On aligned wave topographies, the proportion of aligned FAs increased compared to a flat surface but the increased degree of alignment varied with ridge width and density.[102,108,126,128,143] These results demonstrate that the cell's ability to form FAs and transmit traction forces are regulating the contact guidance response.

It is hypothesized that the limited width of ridge topography physically constrains FA elongation in the perpendicular direction but since there is no constraint in the parallel direction, cells on the topography have proportionally more parallel-oriented FAs.[125,147] FA alignment and elongation parallel to the topography may lead to anisotropic force distribution and to cell polarization.[108,125,143,146] Doyle *et al.* showed that cells on flat ECM lines had higher protrusion rates and higher adhesion stability than cells on flat surfaces where cell adhesion wasn't restricted to the width of a patterned line.[83] On fabricated polymer fiber networks, cell focal adhesion formation localized to the 3D fiber surface. Altering the geometry of the fiber network from isotropic to anisotropic generated polarized cells that aligned parallel to the fibers.[148] Kubow *et al.* observed that cells formed continuous sequential adhesions parallel to aligned fibers, causing cell protrusions to persist in the direction of individual local fibers and contributing to overall

cell alignment.[149] Although the exact mechanism of FA regulation of contact guidance is still unknown, these studies show that physical constraint of FA formation through environmental topography can lead to cell polarization and contact guidance.

1.5.4 Molecular mechanisms of contact guidance

To undergo any type of directional migration, cells must balance protrusive and contractile forces. Although topography has been known to induce directional migration for decades, the molecular mechanisms involved are still not well understood. A number of the molecular components involved in generating the cytoskeletal forces necessary for directional migration are also involved in the cellular response to topography including actin[150,151], myosin II[152], integrins[153], and focal adhesion kinase[120,140]. The field has largely presumed that directional guidance by 2D adhesive patterns and by topographic features occur via a common mechanism, but mechanism studies of cells on topography are still somewhat lacking.

Myosin II is a major regulator of cell contractility and is necessary for cell polarity on a flat surface, but is not necessary for contact guidance.[125,130,143,154,155] In general, myosin II inhibition reduces the effect of topography on cells, but does not decrease contact guidance to the level of cells on a flat control surface.[130] There have been some differing reports as to the magnitude at which MII inhibition reduces contact guidance, but these may be due to differences in experimental design or cell type. Since myosin is inherently involved in the cell's ability to migrate, it is difficult to deconvolve the effects of myosin inhibition on directed migration from the effect on migration in

general.

Wang *et al.* showed that the MII inhibitor blebbistatin reduced MDA-MB-231 breast cancer cell migration speed but did not significantly affect directionality at low dosage on aligned ridge topographies.[144] Thus, MII may have a larger effect on overall cell migration speed rather than the directional response to topography. Furthermore, this result implies that topography-guided migration may enable cancer cells to migrate directionally out of a tumor even if cell contractility that normally drives cell migration is inhibited. Kubow *et al.* found that individual protrusions of a cell locally align parallel to topography regardless of the topography orientation, and that this alignment occurs even under MII inhibition.[149] However, to induce overall cell polarization, a majority of the individual cell protrusions had to be aligned, which only occurred if the underlying topography features were aligned. MII inhibition studies show that cells are able to respond to topography even with impaired mechanosensitivity, indicating that myosin contractility is not the driving mechanism underlying contact guidance, although it seems to play a role in the process.

Other studies have shown that cell alignment to topography requires the Rho/ROCK pathway [156,157], but that other Rho GTPases like Cdc42 and myosin light chain kinase (MLCK), which enables myosin binding to actin filaments, are not necessary.[130,154] Wang and Schneider showed that in MDA-MB-231 breast cancer cells, inhibiting MLCK slightly reduced directionality while inhibiting ROCK had a larger effect, but neither reduced overall migration speed.[144] 3T3 fibroblasts normally migrated faster on microposts than flat surfaces, but migration speed did not increase when Focal

Adhesion Kinase (FAK), a major regulator of FA signaling, was knocked out.[152] Gerecht *et al.* found that actin disrupting agents attenuated the alignment of human embryonic stem cells on ridge topographies.[151] Actin is the main cytoskeletal component in the cell for transmitting tensional forces during spreading and migration, so it remains unclear whether actin plays a specialized role in contact guidance or whether the observed effect was due to a more general disruption of cell mechanotransduction.

Rac1 plays a central role in regulating directional migration on flat surfaces, but its role in contact guidance has not been well studied. On flat ECM patterned islands, FA formation at the leading edge of cells colocalizes spatiotemporally with Rac1 activation, indicating a role of Rac1 in FA regulation.[93] Rajnicek *et al.* found that blocking Rac1 using a custom peptide did not affect corneal epithelial cell elongation or directional migration on aligned square waves.[158,159] However, this study used quartz substrates with no ECM coating, likely affecting the ability of cells to undergo integrin attachment and form focal adhesions.

1.5.5 Effect of cell type on contact guidance

Although almost all cell types have displayed the effect of contact guidance, the magnitude of this effect and the relevant topography dimensions that elicit an effect vary between cell types. Recent studies have shown that these differences may be related to differences in contractility between cell types and the primary mode of cell migration, mesenchymal or amoeboid. Most cells utilize mesenchymal migration, which is the type of cell migration consisting of a leading protrusive edge and a contractile rear. Amoeboid

migration is a type of migration driven by actin-rich pseudopods that is thought to be independent of integrin adhesions and is exhibited in Dictyostelium amoeba, lymphocytes, leukocytes, dendritic cells, and some cancer cells.[160] Cells undergoing mesenchymal migration respond more strongly to topography, while cells that undergo amoeboid migration have a lowered response fidelity.[125,144] It is thought that the decrease in contact guidance is a function of lower cell contractility and adhesion to the ECM. In support of this theory, amoeboid cells migrated with increased directionality on topography if contractility was enhanced or if integrins were activated.[144] Ray *et al.* also showed that cell types with higher E-cadherin expression, a cell-cell adhesion molecule, had less cell elongation and directional migration on topography.[160] They theorized that the tensional forces between cells competed with or disrupted the anisotropic force distribution that topography normally induced in cells. This is further supporting evidence that anisotropic forces caused by cell-ECM interaction regulate the contact guidance response, but a direct causal relationship has yet to be established. Better understanding of the precise molecular mechanisms of topography-guided directional migration will enable researchers to realize how complex external cues affect cellular behavior.

1.5.6 Fabrication methods for studying contact guidance

Most studies of the effects of topography on cells have used a form of lithography to fabricate the structures, but others have used methods such as chemical or physical etching, electrospinning, or micromachining.[161,162] Although traditional lithography

methods have been useful for a great deal of work, the types of structures that can be made and the available feature resolution is limited. For soft lithography, which often uses poly(dimethylsiloxane) (PDMS) molded off a silicon wafer master made using photolithography, the feature resolution is limited to the micron range below which the PDMS elastomer does not maintain structural integrity.[79] The limitations of traditional fabrication methods have constrained topography studies to use predominantly square-shaped waveforms composed of flat surfaces and sharp edges, which are not commonly present in physiological settings.

More recently, studies have begun using stereolithography and two-photon absorption lithography for generating topographies. Both of these processes are forms of 3D printing which utilize a laser beam focused into a volume of photoresist to undergo layer-by-layer addition. The laser initiates the formation of a solid through photopolymerization within the focal volume, resulting in an ovoid-shaped solid known as a voxel. The laser focus can then be moved using either a piezo-controlled stage or galvo-scanning mirrors within the volume of photoresist to create complex geometries that are not possible using other techniques.

Direct laser writing (DLW) is a recently-developed form of stereolithography that offers complete 3D spatial control to produce virtually any user-programmed surface with sub-micron resolution. A femtosecond-pulsed laser is typically used to provide the high light intensity needed for two-photon absorption, but at a lower average energy than non-pulsed lasers, avoiding overheating of the photo-curable material. Two photon absorption occurs at half the wavelength of the laser, so the printing material must be

transparent at the laser wavelength and absorbent at half the laser wavelength. Since DLW prints a solid structure within a volume of photocurable liquid that can act as a support during the printing process, printed structures do not have to initially support their own weight upon printing as they have to for extrusion-based printing. The nanometer-scale 3D spatial control of DLW and the recent development of new systems and materials has made it an increasingly popular tool to study the effects of 3D microenvironments in biology and cell migration.[96,131,163–165]

1.5.7 Effects of curved topography on cells

Although most studies have used square waveform-shaped topography, there have been some studies of the effects of curved topography using various fabrication methods. Song *et al.* used X-ray lithography to fabricate sinusoidal waves and found that T-cells migrated preferentially within the troughs of the waves, more so for waves with a shorter wavelength.[165] However, the effect of topography may be different for T-cells that undergo amoeboid migration, which is thought to be adhesion and integrin independent, as compared to cells that utilize mesenchymal migration.[160,166] Bettinger *et al.* used spin-coated sucrose coupled with standard soft lithography to produce aligned curved wave structures and found that bovine aortic endothelial cells aligned parallel to the waves, however these patterns did not have well-defined or uniform curvature.[119] Guvendiren *et al.* utilized defined hydrogel swelling to pattern various curved topographies[167] and other studies have used polymer buckling or deformation to fabricate curved surface topographies.[143,168–171] Although these studies show that aligned curved surfaces are able

to illicit the contact guidance response, many of the fabrication methods were not well controlled, producing curved structures that were not easily reproducible and did not have well-defined or customizable dimensions. Given the prominence of curved features in native tissues, such as cylindrical blood vessel lumens, a deeper understanding of how cells sense and respond to such features will be important to further elucidate.

CHAPTER TWO: 3D Printing Enables Fabrication of Complex Vascular Geometries and Thick Densely-Vascularized Tissues

2.1 Introduction

One of the major challenges in the field of tissue engineering is the creation of vascularized tissues to supply nutrients and oxygen to cells and to remove waste products. Due to diffusion limitations, cells more than a few hundred microns away from vasculature in a tissue will become necrotic.[5] To engineer larger tissues and eventually organs, the field must develop a method to embed vasculature within 3D tissues so that blood flow can access the entire tissue volume. The vasculature must be rapidly perfusable to supply nutrients to cells throughout the tissue and perfusion must be sustained for long-term function in tissues that are implanted into a host. The ability to generate tissues with spatially-controlled vascular patterning is not only useful for tissue replacement, but will also enable studies of cell biology in more physiologically accurate *in vitro* platforms.

There are two major strategies for patterning vasculature in engineered tissues, either top-down or bottom-up. The top-down approach is to pre-fabricate vasculature in tissues prior to introducing cells. This prevascularization approach creates vessels that provide immediate nutrient supply once cells are introduced to the tissue, but is often limited by the capability and resolution of the fabrication method used. Recent approaches have utilized 3D printing technologies to generate larger tissues with organized vasculature, either by printing a scaffold, printing a sacrificial material to mold

vasculature, using photodegradable materials and spatially-controlled laser ablation, or by directly printing live cells.[21,23–28] In addition to perfusing an engineered tissue, recent studies have shown that organized vascular geometries can improve vascular integration upon implantation into a host.[6,172] Although top-down approaches have shown promise, the current fabrication methods can be time consuming, especially for larger tissues, and cannot produce vessels at the scale of physiological capillaries, which can be as small as 3 μm.[1]

The bottom-up approach to vascular engineering typically utilizes the inherent ability of endothelial cells (ECs) to spontaneously self-organize from single cells to form multicellular vascular networks, a process known as vasculogenesis. The vasculogenesis-driven approach has the benefit of enabling the formation of high-density capillary-scale vessels simultaneously throughout a tissue construct, often without much need for complicated engineering. Most of these methods have utilized ECs or EC progenitor cells in addition to either chemical growth factors or supporting cell types, such as fibroblasts or pericytes, to increase the speed and robustness of vasculogenesis.[30–33,35,36] The final capillary-scale networks formed are dense enough to supply nutrients to all cells throughout a thick tissue and have been able to last up to a year when implanted in mice, but they lack organization and can resemble a dense tumor vasculature network.[28,41] Furthermore, this bottom-up approach alone cannot be used for engineering larger tissues as the vascular networks take a few days at minimum to form and thus cannot be perfused quickly enough to prevent necrosis of cells in the tissue core. To establish an organized yet dense vascular network structure that can access the entire tissue volume, the best

method may be a combination of both the top-down and bottom-up approaches.

We used a top-down method developed by Miller *et al.* to 3D-print carbohydrate-sugar filament networks to use as sacrificial molds for fabricating vascular networks.[21] 3D-printed sugar networks are encapsulated in ECM then the sugar is dissolved and washed away. This leaves hollow channels in the ECM that can be lined with endothelial cells. The original method generated vascular networks with various vessel diameters and network architectures and showed the ability to use a variety of different ECM materials to mold the surrounding tissue. Furthermore, the biocompatibility of the sugar enabled the addition of parenchymal cells at physiologic densities in the extravascular tissue. However, this method was limited in its ability to create certain complex vessel geometries or capillary-scale vasculature. Furthermore, it remained unclear whether the use of a polymer coating on the sugar networks, necessary to maintain the structure of the printed network architecture upon ECM encapsulation, could interfere with the migration of cells into the bulk ECM gel. To address these issues, we improved the 3D printer hardware, the sugar-making process, and the polymer-coating process. We further developed a method to co-print PDMS to enable more complex vascular architectures and to introduce direct flow into the networks. By integrating these advances to the 3D printing method as well as a bottom-up approach to vascular network formation, we developed a scalable approach to create thick vascularized tissues with organized multiscale vascular networks.

2.2 Results

2.2.1 Upgraded 3D printer hardware increased print capabilities

The original 3D-printer used by Miller *et al.* was a custom-modified RepRap Mendel 3D printer (Gen3, MakerBot). Although this machine was able to effectively print a variety of structures, it offered limited resolution and reproducibility for more complex architectures, mostly due to the use of plastic parts and low-precision motors. To address these hardware limitations, we modified a ShopBot Desktop, a commercial 3-axis CNC machine, to 3D-print sugar (Figure 2.1). The ShopBot was much more stable than the original printer due to a heavier metal frame, significantly reducing printing errors, and the stepper motors had a step-size resolution of 6.35 μm, much finer than the previous motors. Although this machine was more expensive than the previous printer, it is still relatively low cost (~$5000) compared to other bioprinters. We removed the CNC drill head from the ShopBot and replaced it with a heated extruder for sugar printing. To control the heating element and the ShopBot motors, we rewired the ShopBot electrical control board to connect with a RAMBo 1.3 (Ultimachine) circuit board. By doing so we were able to use the same 3D printing software and custom Python scripts to generate 3D motion control machine code (GCode) to drive the machine. The other necessary electrical and mechanical components for printing molten sugar using controlled air-pressure extrusion were also incorporated based off the previous method.[21]

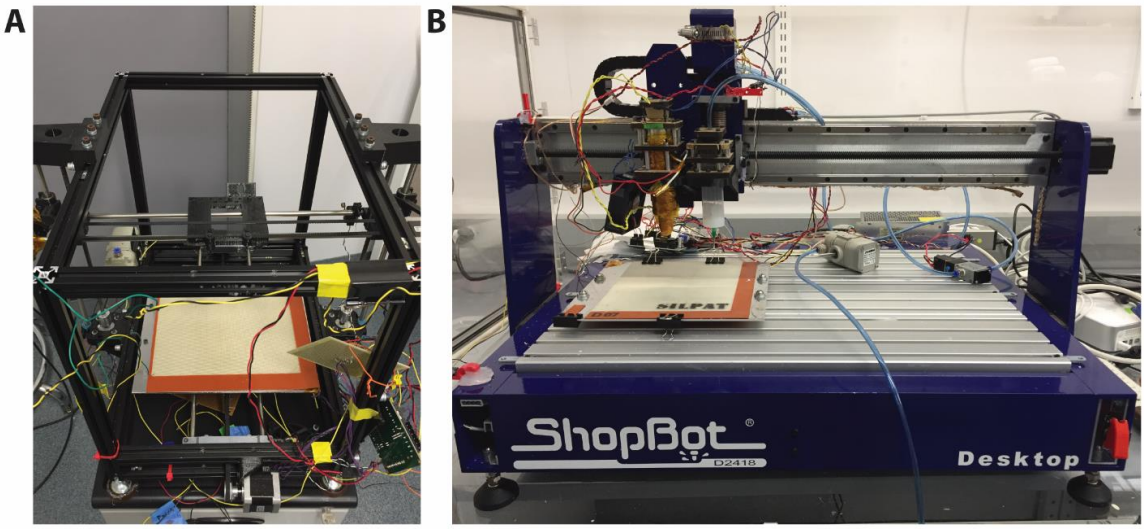

Figure 2.1: A) The custom-modified RepRap Mendel 3D printer used in the previous 3D sugar printing method. **B)** The ShopBot Desktop modified to use for 3D printing sugar.

2.2.2 Improved sugar-making process increased print robustness and throughput

We next sought to improve the sugar-making process to increase the structural stability of the printed constructs. The previous carbohydrate sugar-glass was made by dissolving glucose, sucrose, and dextran in water and then boiling off the water. Although the sucrose, glucose, and dextran mixture could be printed effectively, the resulting printed structures were often brittle once cooled and could easily break upon handling. Inspired by the food industry, we used isomalt instead of the glucose and sucrose and found that the resultant sugar structures were somewhat flexible while still maintaining their structural integrity. We mixed the isomalt with dextran to mechanically strengthen the sugar-glass and improve its temperature stability. We tested for the optimum ratio of isomalt:dextran:water by making batches with different ratios and printing sugar

constructs with each. The formula we ultimately found worked best used 70 g isomalt:7 g dextran:70 mL water. Printed structures using this sugar formula were less brittle and could be more easily handled for post-processing, making the entire process more reproducible and enabling the production of smaller diameter filaments and more complex printing geometries in the future.

We next modified the sugar preparation method so that it did not have to be made immediately prior to printing, which otherwise took about an hour each time. Instead, we heated a large volume of the isomalt, dextran, and water mixture then poured the molten sugar into 30 mL syringes and allowed them to cool, forming solid cylinders of hardened sugar. The final viscosity of the molten sugar greatly affects the sugar extrusion and is largely a product of the water content of the sugar. To compensate for changes in the water content caused by cooling and reheating the sugar, we heated the sugar to a lower temperature of 155° C before cooling rather than 165°, resulting in the ideal final molten sugar viscosity for printing. Once the sugar cylinders cooled, we could store them in a 27° oven for over a year before printing. To print with the pre-made sugar cylinders we just put one into the heated extruder for a few minutes prior to printing to melt it.

Using the improved 3D printing hardware and sugar formulation from section 2.2.1 and 2.2.2, we quantified the 3D-printed sugar fidelity by printing 10 constructs containing 5 parallel channels each. We optimized the print parameters and code to print 300 μm channels and averaged 308 μm diameter with a standard deviation of 18 μm. 2 out of the total 50 channels printed had an error, either the channel broke or was not printed straight because it didn’t properly adhere to the print bed. It took a total of 4

minutes and 52 seconds to print a single construct containing 5 parallel channels.

Average Printed Channel Diameter [μm]	308
Standard Deviation of Channel Diameter [μm]	18
Total Printed Channels	50
Failure Rate of Printed Channels [%]	4
Print Time for Parallel 5-channel Construct [mins]	4:52

Table 2.1: Quantification of 3D printing for 10 total sugar constructs containing 5 parallel channels each using the improved 3D printer hardware and sugar formulation. The print parameters were optimized to print 300 μm diameter channels. Temperature was kept constant at 130°C and pressure at 40 psi. Diameter of printed channels was measured using a micrometer with a measurement resolution of 0.01 mm.

2.2.3 Better control over polymer coating and degradation increased print reproducibility and removed the barrier to cell migration

To prevent the printed sugar constructs from immediately dissolving and losing their structure upon encapsulation by an ECM hydrogel, a polymer coating is necessary. The sugar networks were previously coated by dipping the sugar prints into a solution of poly(d-lactide-co-glycolide) (PDLGA) dissolved in chloroform, an organic solvent that doesn't dissolve the sugar. However, this method did not produce a uniform distribution of the polymer on the sugar surface and often led to defects in the coating that caused the sugar underneath to dissolve too rapidly and leak into the surrounding hydrogel before the hydrogel had polymerized. Leaked sugar disturbed the hydrogel polymerization and led to deformities in the molded channel geometry. To improve the polymer coating efficiency we modified a Badger Air-Brush Model 175-7 to spray-coat a solution of

PDLGA dissolved in chloroform. Using the air-spray method we could precisely control the coating thickness. A thicker coating could be produced by increasing the spray time or by layering a number of iterative coatings, letting the previous layer of coating dry before adding another layer. Thicker coatings slowed down the speed of sugar dissolving within the channels, allowing us to finely control the speed at which the sugar networks dissolved once an ECM hydrogel was cast onto them. The spray-coating technique also produced a more uniform coating, leading to an increased throughput for molding vascular networks. The air-spray method results in a coating that can be seen under phase-contrast microscopy and resembled a dense splatter pattern on the surface of the sugar channels (Figure 2.2 A,B). The coated sugar networks could be stored for even longer than uncoated structures since the coating protects sugar from any moisture in the air, over one year when stored in a 27°C oven.

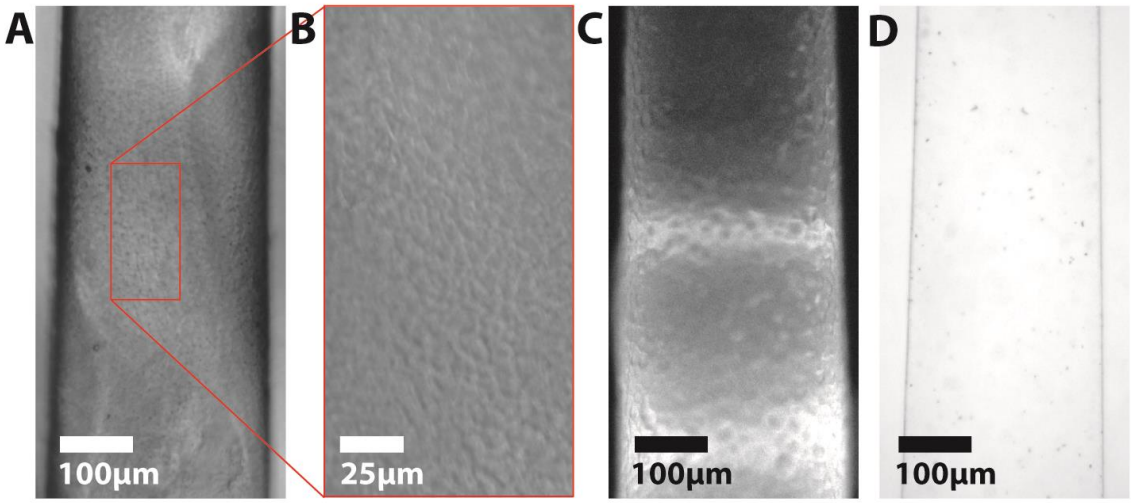

Figure 2.2: **A)** Phase-contrast microscopy image of air-sprayed PDLGA coating on the surface of a cylindrical sugar filament. **B)** High-magnification image of PDLGA coating showing the splatter-like pattern formed from the air-spray coating. **C)** Image of PCL

coating on a sugar filament taken using a dissecting microscope using reflected light. **D)** Brightfield image of a sugar filament that was coated with PCL, embedded in a fibrin hydrogel, then treated for 48 hours using lipase solution to degrade the PCL.

PDLGA is biocompatible and could be safely used with cells or for implantation, but it was unclear whether the polymer coating acted as a physical barrier for cells to prevent them from migrating into the bulk ECM. Thus, we tested a number of other polymers to replace PDLGA that could be degraded and removed afterwards. The polymers needed to prevent the sugar from dissolving too quickly and leaking into the surrounding hydrogel, but also be degradable within a few days either in aqueous solution or using another reagent. The polymer also had to be soluble in an organic solvent that did not dissolve the sugar during the coating process. Some of the polymers we tested were combinations of different ratios of sebacic acid, azeleic acid, and recenolic acid, however none of these polymers satisfied the necessary coating requirements. We found that polycaprolactone (PCL) dissolved in chloroform and could be used with the spray-coating technique to prevent sugar leakage into the ECM. After flushing out the sugar, lipase from *Pseudomonas sp.* degraded the PCL within 48 hours (Figure 2.2 C, D). We confirmed removal of the PCL layer using phase-contrast microscopy and by adding 70 kDa FITC-dextran into the channel. Prior to degrading the PCL, the dextran remained only in the channels (Figure 2.3 A,B), whereas in channels where lipase had degraded the PCL layer, the dextran was able to diffuse out into the surrounding hydrogel (Figure 2.3 C,D). Cells attached and spread faster (less than 30 minutes) in channels where PCL had

been degraded, as opposed to PDLGA coated channels where cells took about twice as long to attach. Removing the coating layer of PCL allowed ECs to attach directly to the fibrin gel and removed the potential barrier for ECs to migrate into the surrounding ECM.

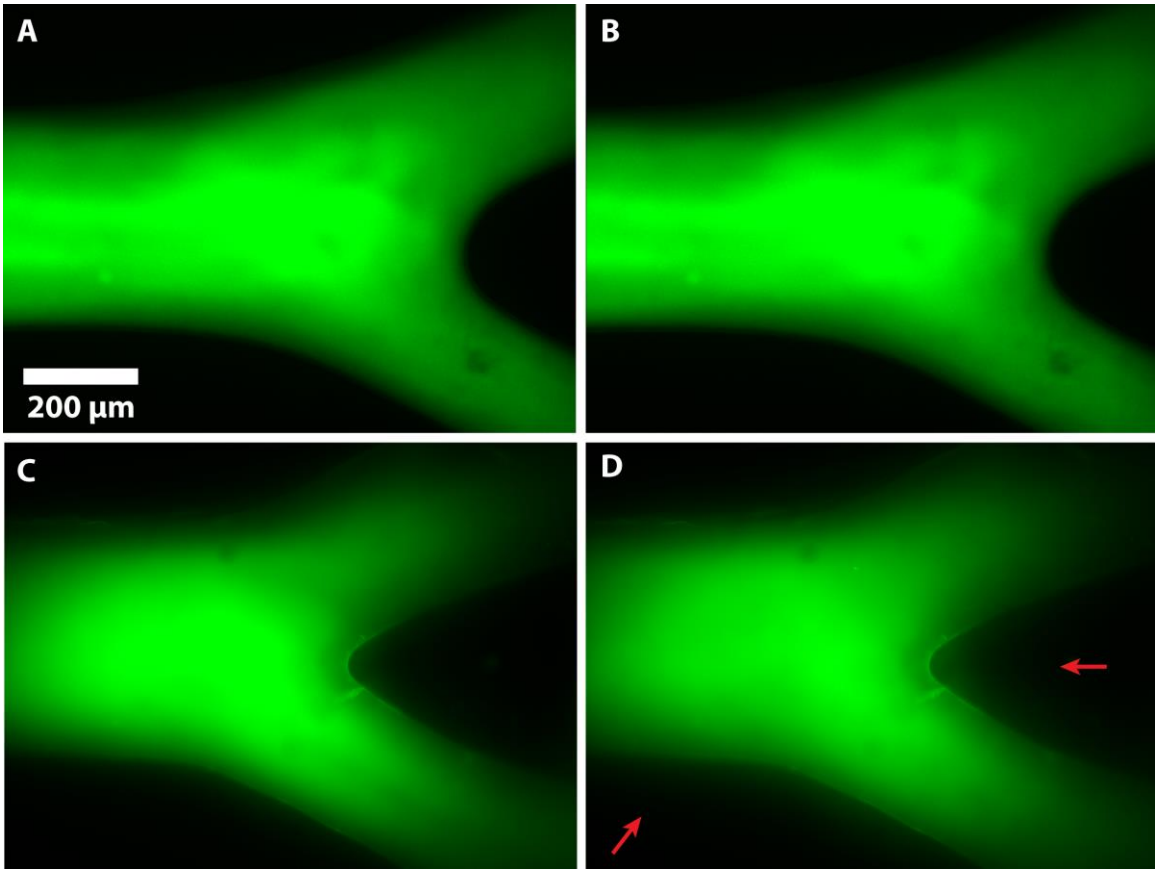

Figure 2.3: 70 kDa FITC-dextran injected into a branched channel coated with PCL and embedded in a fibrin gel at the **A)** time of injection and **B)** 5 minutes later showing no leakage of dextran out of the channel. **C,D)** A branched sugar channel coated with PCL then treated with lipase to degrade the PCL. 70 kDa FITC-dextran can be seen leaking out of the channel into the surrounding fibrin gel (indicated by the red arrows) from the **C)** time of injection to **D)** 3 minutes later.

2.2.4 Co-printing PDMS walls enabled more complex vascular networks

Although 3D printing enables spatial control of printed networks, the possible architectures of the initial method were limited by the use of sugar as both the support structure during printing and the channels themselves. To print suspended sugar cylinders that are raised off the bottom surface, we need a support wall for printed sugar filaments to rest on. In the original method the support was printed sugar that ultimately became fused with the filament network itself (Figure 2.4 B). After encapsulating the sugar in ECM, the vascularized tissues were removed from the sugar walls and then the channels were manually injected with cells using a syringe.

To print more complex geometries, we added a second print head to the ShopBot to co-print polydimethylsiloxane (PDMS) support structures (Figure 2.4 A). The PDMS support structure allowed us to keep each channel separate so that the fluid was independently controlled in each. By separating the channels, we were able to pattern different cell types or different ECM materials into the individual channels encapsulated within the hydrogel, which was not possible with the previous method (Figure 2.4 C). The PDMS support also enabled us to add direct flow into the channels and to pattern more complex vessel geometries such as branched networks.

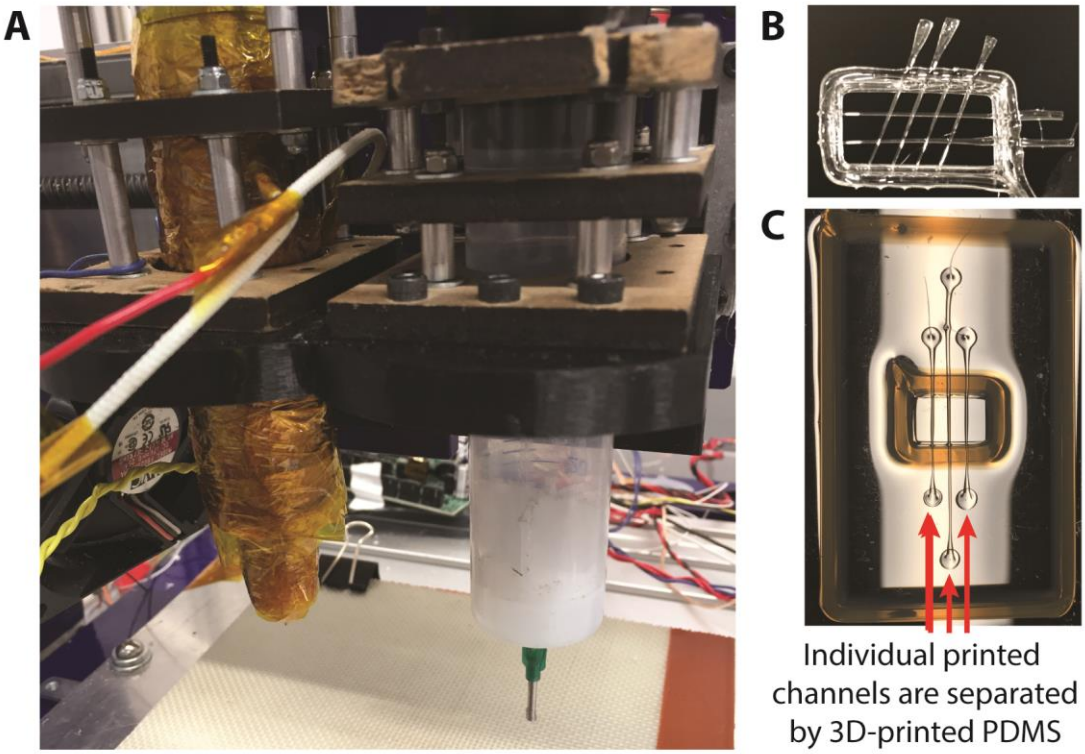

Figure 2.4: A) Sugar print head (left) and additional PDMS print head (right). **B)** The previous method of 3D printing sugar lattices used sugar as both the channels and the surrounding support structure so all the channels are connected. Sugar filament channels are raised off the bottom surface by the surrounding printed sugar walls, so that the channels become embedded in ECM upon casting. **C)** 3-channel device fabricated using PDMS 3D printing as a support structure. The PDMS is used to suspend and separate each channel so that they can be individually ported using a biopsy punch at the channel ends. Each channel can be filled with different cells or materials individually after encapsulation in ECM and evacuation of the dissolved sugar.

To 3D print PDMS we used pneumatic-driven extrusion, similar to the sugar printing method, except that the PDMS was not heated. We used Dow Corning SE 1700 PDMS, a type of PDMS that has a higher viscosity than other types of PDMS (542700 cP compared to 3900 cP, respectively) and retains its shape after extrusion through a nozzle. The PDMS was loaded into a 50 mL plastic syringe and mixed with the cross-linking catalyst before beginning printing. A 14 gauge (1.6 mm I.D.) needle tip was attached to the syringe and the syringe was pressurized with air under electronic control, extruding the PDMS layer-by-layer. The PDMS can be printed in any geometry that uses layer-by-layer addition, but to use the PDMS in conjunction with 3D-printed sugar filaments we designed a PDMS support structure with separate adjacent rectangular compartments. The sugar networks were designed so that the region of interest was contained within the single middle compartment that was later filled with ECM. After evacuating the sugar, this compartment housed the ECM with hollow channel geometries as defined by the printed sugar.

First a bottom layer of PDMS walls was printed, then sugar networks were printed on top of the PDMS wall, and then another layer of PDMS was printed on top to enclose the sugar and keep it in place (Figure 2.5). The sugar networks were then spray-coated with polymer (either PDLGA or PCL) and the outside compartments were filled with additional PDMS, encasing the ends of the sugar networks in PDMS so that they could later be directly ported. About 20 of these structures could be made within an hour and they could be stored for long periods of time prior to use. The middle compartment was filled with ECM to encapsulate the sugar lattice, then the dissolved sugar was evacuated

through ports formed using a biopsy punch in the outside PDMS compartments (Figure 2.5 A). The remaining hollow channels could then be seeded with endothelial cells to form endothelialized vessels or filled with different ECM materials.

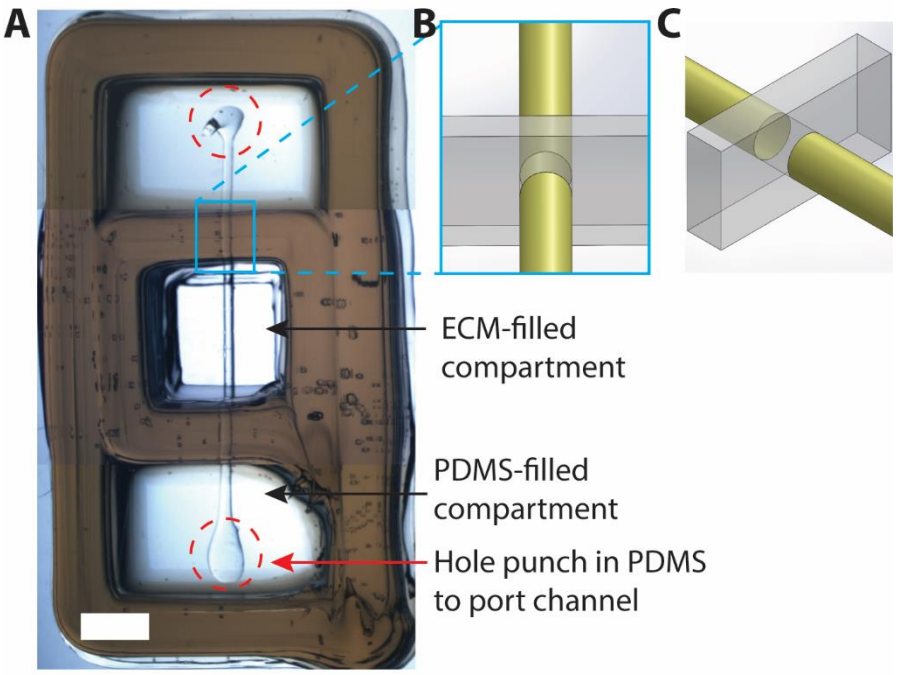

Figure 2.5: A) Picture of a single channel device supported by 3D-printed PDMS support walls. The top and bottom compartments are filled with clear PDMS (not printed) and the middle compartment is filled with ECM to encapsulate the suspended channel. Red dotted-lines indicate where holes are punched in the PDMS compartments to directly port the channels. Scale bar, 2 mm. **B,C)** 3D schematic of the channel showing it is suspended and encapsulated by the 3D-printed PDMS support walls. Yellow channels represent 3D-printed sugar, transparent grey represents the 3D-printed PDMS walls.

Using the printed PDMS support structure, we were able to fabricate complex vessel geometries that were previously impossible or impractical using the original

method, such as hierarchical branching geometries like those observed *in vitro* (Figure 2.6 C). As a simple demonstration we printed a Y-shaped branch channel with a 400 µm diameter main channel that splits into two 300 µm channels (Figure 2.6 B). These sugar branches were spray-coated with polymer and placed into printed PDMS walls with the previously described configuration (Figure 2.6 F). We filled the middle compartment with a 10 mg/mL fibrin hydrogel, ported all three ends of the channel, and evacuated the sugar, leaving a branched hollow channel in the fibrin gel. To form an endothelial cell monolayer we pipetted a HUVEC suspension into the ported channel and allowed cells to attach to the channel walls. Confocal microscopy confirmed the presence of a fully confluent endothelial cell layer with an open lumen within the branch channel after seeding (Figure 2.6 H,I,J).

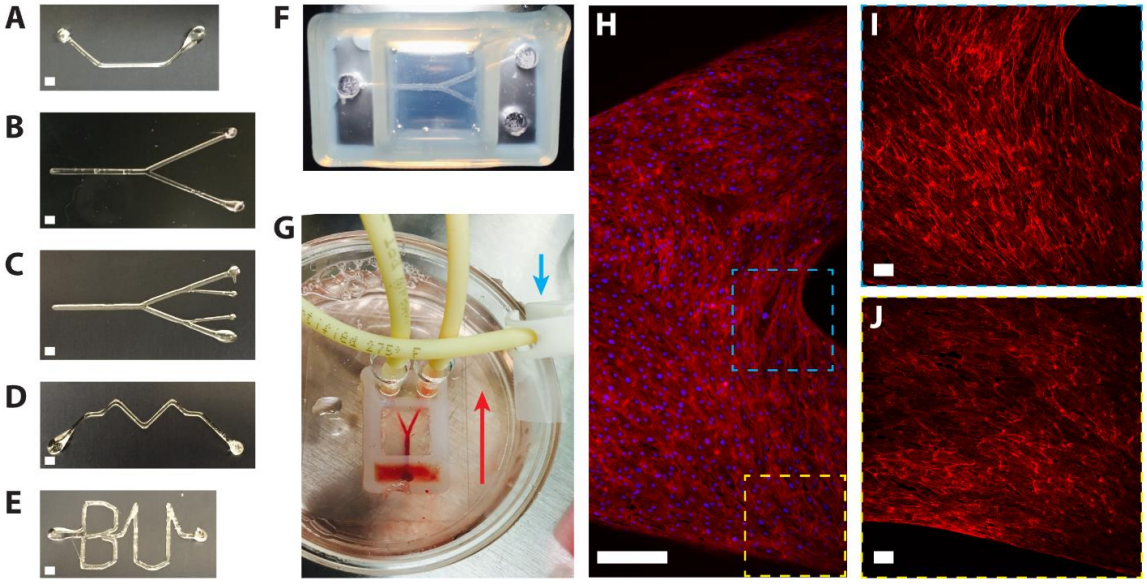

Figure 2.6: **A-E)** Examples of different sugar geometries that can be printed, then suspended using a PDMS support structure to mold hollow channel structures in ECM.

Scale bars, 400 µm. **A)** An angled channel, **B)** a single branch channel, **C)** a hierarchical double branching channel geometry, **D)** a zig-zag channel, **E)** a channel in the shape of "BU" lettering. **F)** A single branch channel embedded in a fibrin gel (central compartment) and ported at the end of each branch using a 3 mm biopsy punch (left and right compartments). **G)** Each end of the branch was directly connected to tubing which leads to a peristaltic pump. Blood was injected into the main channel port at the bottom and pulled through the branch channel. The red arrow indicates the direction of flow. Each line of flow tubing had a pinch clamp connected to it that could be used to block flow, indicated by the blue arrow. **H)** Confocal imaging (maximum projection) of a branched channel seeded with RFP-LifeAct labeled endothelial cells (red) with a DAPI stain (blue) that was under flow for 24 hours. Scale bar, 100 µm. **I)** Zoomed in image of the blue dotted-line region and the **J)** yellow dotted-line region showing only the F-actin labeled HUVECs. Scale bar, 10 µm. Endothelial cells were observed to elongate parallel to the direction of flow.

Fluid flow has been shown to impact endothelial cell morphology, migration, thrombogenicity, and permeability, but it remains challenging to integrate controlled flow into many engineered *in vitro* vascular systems.[48–54] Since the PDMS support structure allows direct insertion of tubing into the channel ports, we were able to introduce fluid flow using a peristaltic pump. To prevent bursting of the hydrogel due to pressure from fluid flow, we pulled liquid through the branches rather than pushing flow through (Figure 2.6 G). After the channel was endothelialized, media was constantly flowed

through at a rate of 1 mL/min, giving a flow rate of 0.5 mL/min in each of the branches and 1 mL/min in the main single channel. This flow rate corresponds to a shear stress of 2.65 Pa (26.5 dynes/cm^2) in the 400 μm diameter main channel and 3.14 Pa (31.4 dynes/cm^2) in the 300 μm diameter branches. Shear stresses of 5-10 dynes/cm^2 have been shown to induce cell elongation in the direction of flow.[173] To visualize the endothelial cells, we used RFP-LifeAct labeled HUVECs (RFP-labeled F-actin). Using confocal imaging we found that the channels had an open lumen, an endothelialized monolayer on the channel walls, and that ECs had aligned parallel to the direction of flow after 24 hours (Figure 2.6 H,I,J). Furthermore, we could redirect the flow pattern by blocking flow at the inlet and outlet ports of the branches, which we visualized by flowing fluorescent microbeads through the channel (Figure 2.7 B,C,D). To demonstrate a potential utility of flow control in our system, we flowed blood through the entire branch channel (Figure 2.6 G) then closed the bottom-right branch port using a pinch clamp to stop flow in the bottom-right branch. We then flowed PBS through the main and top right channel (Figure 2.7 D) to wash away the blood only in the main and top right channel, leaving the blood in the bottom right to undergo thrombosis and form a clot in the bottom-right branch channel. This ability to easily control the direction of flow through our engineered vessels could be used to control the direction of flow through a larger or more complex vascular architecture.

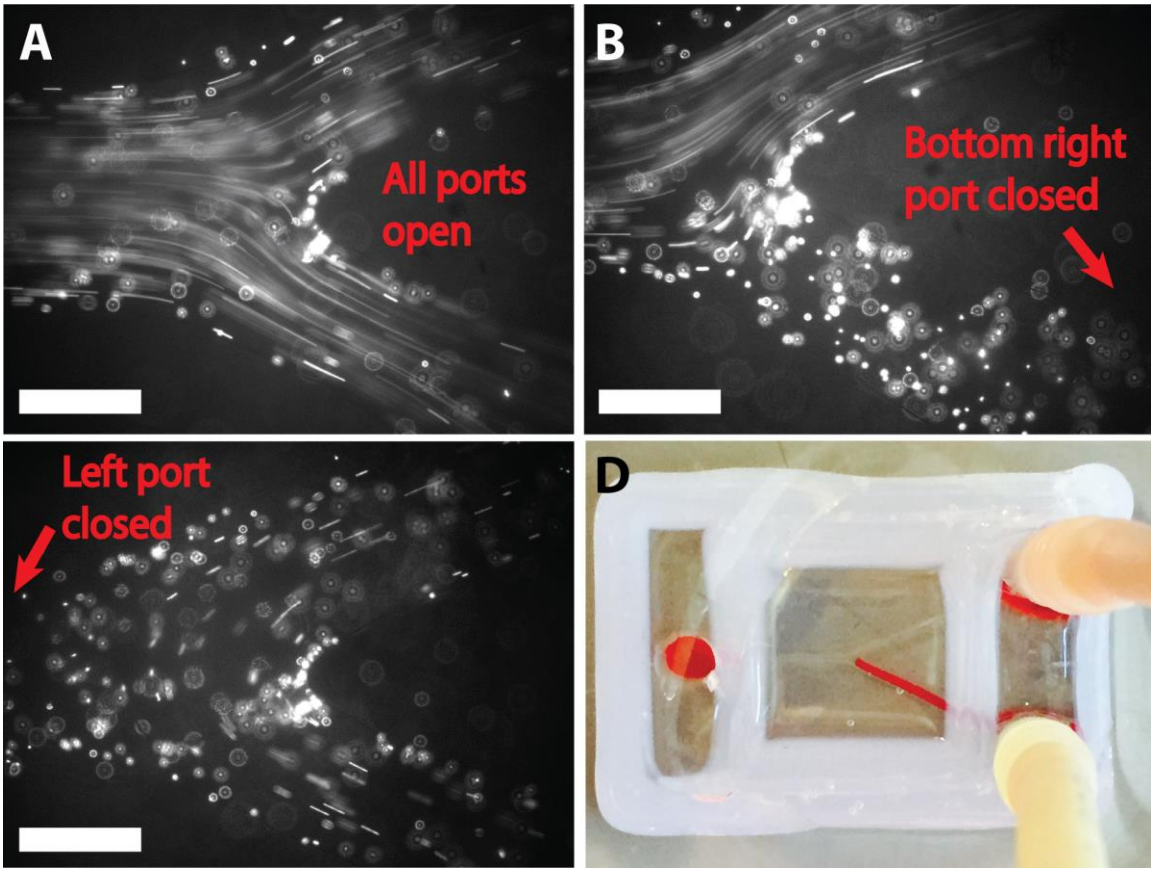

Figure 2.7: **A,B,C**) One second time lapse fluorescence microscopy images taken after flowing fluorescent microbeads into the branched network channel to demonstrate flow control. Scale bars, 300 µm. The images show flow profiles of beads when **A)** all ports are open, **B)** the bottom right port is closed beads flow from the left to the top right, and **C)** when the left port is closed beads flow from the top right to the bottom right. **D)** Branched channel device where blood was flowed into the entire channel including both branches, then flow was stopped in the bottom-right port using a pinch clamp. PBS was then flowed through the channel to clear out the main channel and the top-right branch, leaving a blood clot in the bottom-right branch.

2.2.5 Integrating top-down and bottom-up approaches to vascular engineering to create thick densely-vascularized tissues

Although the original sugar-printing method reduced cell death within a thick tissue, at high cell density the cells that were too far away from fabricated channels still experienced necrosis.[21] However, the sugar could not be printed in much denser networks to access these regions due to fabrication limitations. We sought to integrate a bottom-up approach by integrating cells in the ECM that would undergo vasculogenesis to form capillary-scale networks. If the vasculogenic networks could anastomose to our 3D-printed sugar networks, the resulting vascular network could perfuse the entire tissue volume.

Before we put cells into the entire bulk gel, we tested whether cells would undergo vasculogenesis in a smaller controlled volume and whether endothelial cells would be able to sprout through the polymer coating on the sugar networks and into the bulk ECM gel. Furthermore, in engineered larger tissues or organs, one might desire to spatially control the region of vascular formation to form specific vascular geometries. We found that a mixture of 6 million/mL HUVECs and 3 million/mL human lung fibroblasts (HLFs) co-cultured in a fibrin gel would reliably undergo vasculogenesis and form connected vascular networks with diameters ranging from about 5-30 μm. We used 3D-printed sugar to form parallel 150 μm diameter channels that we encapsulated with a 10 mg/mL bulk fibrin gel. We then filled the evacuated channels with 2.5 mg/mL fibrin gels containing the suspended HUVECs and HLFs. The fibrin polymerized in the channels, forming solid cylinders with embedded cells. Within 3 days the HUVECs

formed multicellular vascular networks with vessel diameters ranging from 10 to 30 µm. Although the vasculogenic structures were mostly confined to the original patterned channels, many cells sprouted out of the patterned vascular channels into the surrounding fibrin gels after 5 days (Figure 2.8).

If we wanted to strictly pattern vasculogenic capillary formation, we could use a thicker polymer coating on the sugar or an ECM material that is not degradable by cells to prevent the cells from sprouting into the bulk ECM. Here we patterned straight parallel channels, but the vasculogenic networks could be patterned within any geometric configuration that sugar can be 3D-printed in. Although spatial patterning of vasculogenesis may be useful in specific cases, most physiologic tissues have vasculature all throughout their volume. Furthermore, using this configuration there were no larger endothelialized vessels so we could not easily directly access or perfuse the channels.

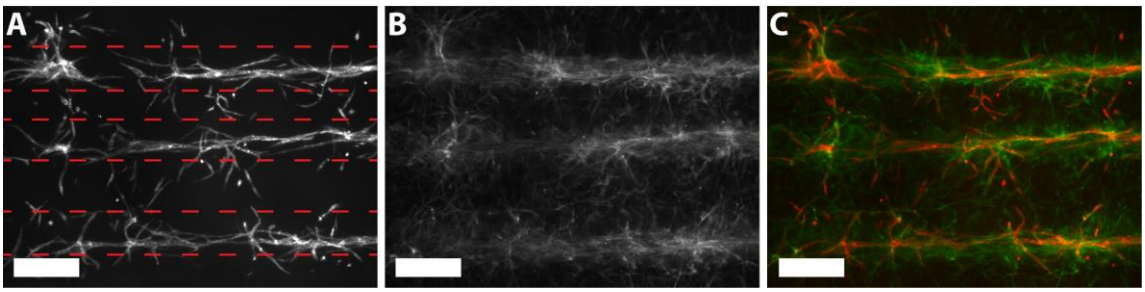

Figure 2.8: A) RFP-LifeAct labeled HUVECs and **B)** GFP-LifeAct labeled HLFs were seeded in parallel 3D-printed channels. After 5 days they formed multicellular vascular networks mostly confined to the edges of the original printed channels (between the red dotted-lines). Some cells sprouted out of the channels into the surrounding ECM. **C)** Merged image of HUVECs (red) and HLFs (green) show co-localization for the two cell

types, especially in areas where HUVECs sprouted out of the channels. Scale bars, 200 μm.

To create a tissue that was densely vascularized throughout its entire volume, we combined the top-down 3D-printed channels with the bottom-up vasculogenic networks. We printed two 400 μm diameter sugar channels and used printed PDMS support walls to separate the channels so that liquid could not flow between them (Figure 2.9 A). The printed channels were angled outwards so that we could separate their ends and later port each channel individually. We used the same mixture of suspended HUVECs and HLFs in fibrin used to form vasculogenic networks previously, but filled the entire volume encapsulating the printed channels. To seal the fibrin gel to the PDMS and to prevent contraction of the gel from cells, we added a thin layer of 20 mg/mL fibrin gel on top. We then ported the ends of the channels that were encased in PDMS and seeded HUVECs into each channel to form endothelialized monolayers.

After 6 days, we fixed the tissues and found that the HUVECs in the bulk hydrogel had formed capillary-like vascular networks throughout the tissue volume that had anastomosed to the larger 3D-printed channels to form a single network with multi-scale vascular channels. To test whether the capillary networks were directly connected to the larger pre-vascularized channels, we injected a 2 MDa dextran solution into the top channel only. Despite the fact that flow prefers to travel through the larger channels due to lower resistance, the PDMS support structure enabled control of flow through the channel ports. We created a pressure gradient by adding more volume of the dextran into

the top channel and removing liquid from the bottom channel so that flow traveled through the capillary networks between the channels. Within a few minutes we observed that the dextran was in the bottom channel and had perfused through the intermediary capillary networks (Figure 2.9 B,C). The vasculogenic capillary networks were the only path for fluid to travel between the two channels, as they were initially separated by the printed PDMS wall. Confocal imaging confirmed that the dextran was perfusing through the lumenized capillary vessels suspended within the fibrin gel (Figure 2.9 D).

By combining the top-down 3D-printing approach and the bottom-up vasculogenesis approach, we were able to create tissues with larger, immediately perfusable printed vessels that became densely vascularized with capillary-scale vessels. These capillary networks were lumenized and were able to anastomose to the printed channels to form a single connected network. Although creating a densely-vascularized tissue here shows proof that the method works, these tissues are thin enough that cells in the bulk would have adequate nutrient supply even without the 3D-printed channels. Since the vasculogenic networks were able to anastomose in this two-channel device, we scaled the method up to create thick densely-vascularized tissues.

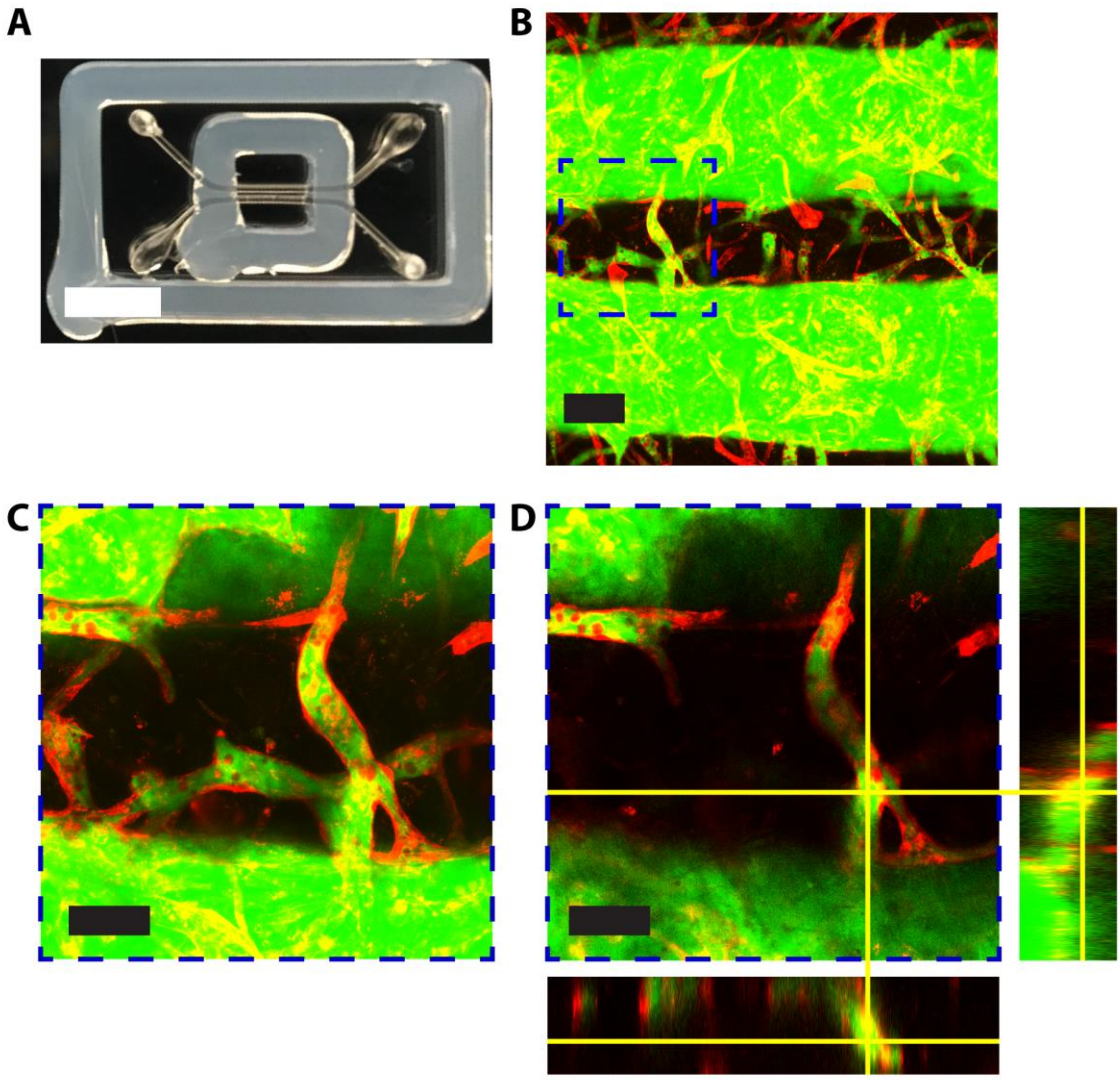

Figure 2.9: A) Picture of a printed two-channel device with PDMS support. The outside compartment is filled with PDMS and the middle compartment is filled with fibrin with embedded HUVECs and HLFs. The two channels are separated by PDMS and are ported individually. Scale bar, 10 mm. **B)** Maximum projection of a confocal image stack (295.82 µm thick) showing the fibrin gel with embedded channels (green, top and bottom) and HUVECs (red) 6 days after seeding. HUVECs in the bulk (red) formed capillary networks connecting the two printed channels. Fluorescent FITC-dextran

(green) was flowed into the top channel only and over time it flowed through the lumenized capillaries towards the other printed channel. Scale bar, 200 μm. **C)** Higher magnification confocal maximum projection of the blue dotted-line region in B (119.59 μm thick). Scale bar, 100 μm. **D)** Orthogonal views of a single confocal slice (thickness 5.69 μm) of the projection in C showing that the capillary channels are suspended within the fibrin gel and lumenized with dextran flowing through them. This particular region of the vessel has a diameter of approximately 50 μm.

To construct thicker vascularized tissues, we 3D-printed two sets of 10 parallel channels that we oriented in orthogonal directions and overlaid on top of each other (Figure 2.10 A). Each set of 10 parallel channels was printed so that all 10 channels were connected at the end by a larger reservoir. Each set of channels was suspended and separated from each other by about 1 mm using 3D-printed PDMS (Figure 2.10 A,B,C). The single connected reservoir enabled us to flow media or cells into all the connected parallel channels simultaneously, making it possible to endothelialize an entire set of 10 connected parallel channels through a single injection and gravity-driven flow after porting directly into the reservoirs.

We encapsulated all of the channels with a fibrin gel containing HUVECs and HLFs then seeded HUVECs into all the parallel channels to form endothelialized monolayers. The entire tissue was approximately 8 mm length x 8 mm width x 4 mm height. Constructs were left on a rocker for 7 days, allowing cells in the bulk fibrin gel to undergo vasculogenesis, forming capillary-scale networks in the fibrin gel between the

pre-patterned channels. After 7 days of culture we fixed the cells and performed confocal imaging to find lumenized capillary networks in the bulk gel connected to the larger channels (Figure 2.10 D). Unfortunately, due to the thickness of the tissue we were not able to image through the entire gel, and thus could not visualize dextran perfusion from one set of channels to the other. However, based on the previous results with the two-channel constructs, we presume that the vasculogenic networks were able to functionally anastomose to the 3D-printed networks to form a connected perfusable vascular network. Furthermore, we were able to flow cell media into one set of channels and out of the other set after the 7 days in culture, which was not possible at the start, implying the capillary networks had connected the two sets of channels. To further demonstrate that the 3D-printed sugar approach can be scaled to fabricate even larger vascularized tissues, we printed a parallel channel construct composed of 100 parallel channels that are 10 cm long each (Figure 2.10 E). These channels could be encapsulated and seeded using the same method we demonstrated here to create very large, densely-vascularized tissues with little additional time or effort.

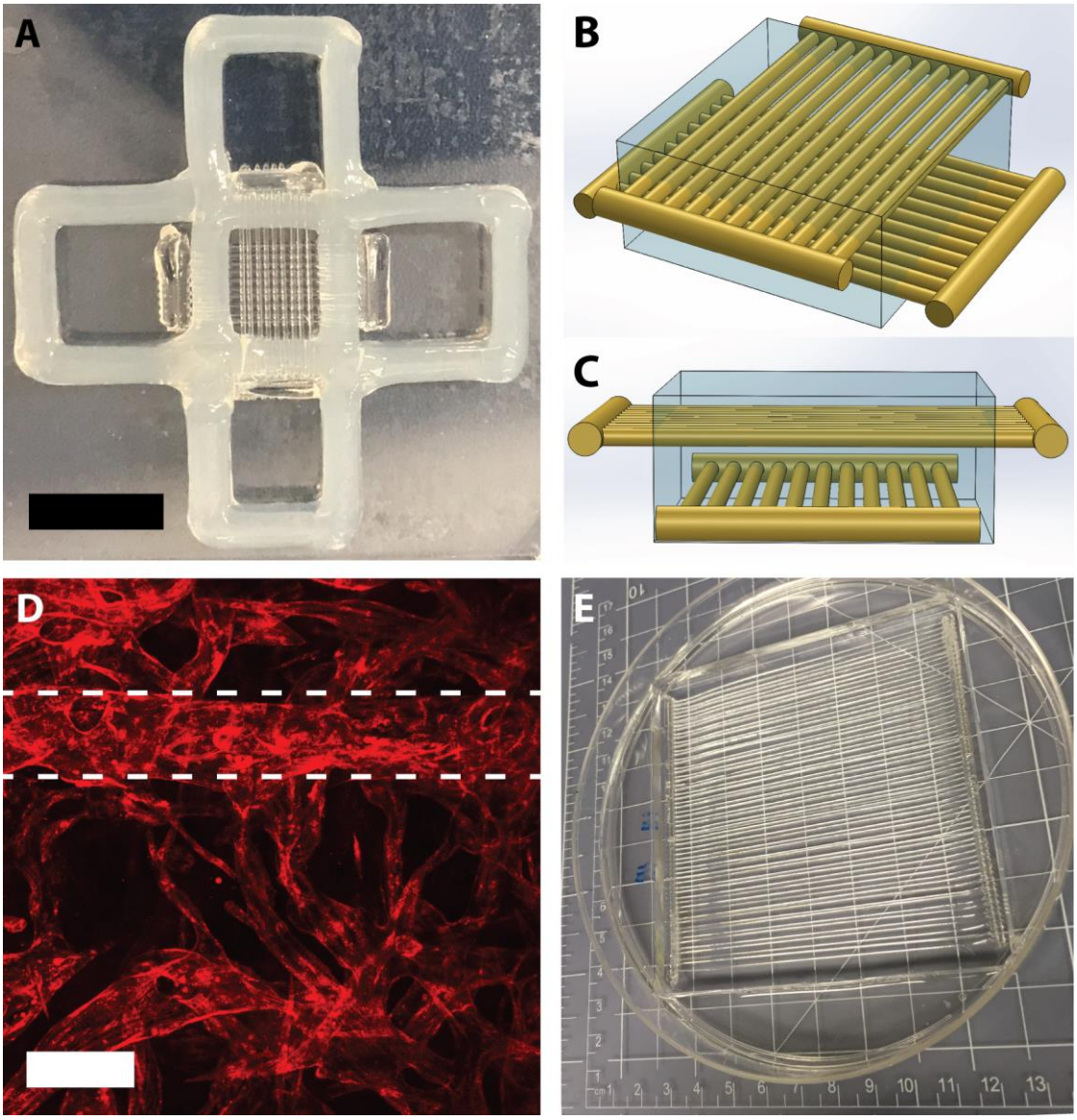

Figure 2.10: A) Multilayer cross-hatch channel geometry composed of two layers of 10 parallel channels. The four outer compartments are filled with PDMS and the central compartment is filled with fibrin, encapsulating the channels. Scale bar, 10 mm. **B,C)** 3D schematic of the sugar channels from the **B)** isometric or **C)** side view. The light blue cube in the center indicates the region that is encapsulated with fibrin. Sugar channel layers are supported and separated from each other by 3D-printed PDMS so that flow

cannot travel between them. **D)** RFP-LifeAct labeled HUVECs (red) and HLFs (not shown) were suspended in the fibrin gels. The HUVECs undergo vasculogenesis, forming multicellular vascular networks that anastomosed to the 3D-printed sugar channels. Edges of one of the 3D-printed channels are indicated by the white dotted-lines. Scale bar, 200 μm. **E)** 100 parallel 3D-printed sugar channels that are each 10 cm long, occupying a 10x10 cm area to demonstrate the scalability of the 3D-printing approach.

2.3 Discussion

Improvements in the sugar printing fabrication methods enabled the generation of vascular networks with increased control, precision, and throughput. We printed structures with higher resolution and greater structural integrity using the upgraded 3D printer hardware and sugar-making process. The spray coating method addressed a major failure mode in the previous fabrication method and allowed us to control the polymer coating thickness, enabling greater control over the dissolution rate of the sugar networks. Furthermore, using PCL we were able to degrade the coating away completely, removing the potential barrier for cells.

Using 3D-printed PDMS as a support structure, we fabricated new types of patterned tissues that were not previously possible. We demonstrated this method by making an endothelialized branched channel embedded in fibrin, but the method could also be applied to produce much more complex vascular geometries and networks. The PDMS support structure also enabled control of fluid flow through the vascular networks, empowering future *in vitro* studies of the effects of flow within vascular networks and

how these effects vary with vessel geometry.

Lastly, we demonstrated the ability to create thick tissues with embedded multi-scale vascular networks formed through a combinatorial top-down and bottom-up fabrication approach. The pre-patterned channels fabricated through 3D printing provided supply of oxygen and nutrients to the surrounding cells. The cells in the ECM surrounding the channels had sufficient perfusion to spread and undergo vasculogenesis, including cells in the center of a 4 mm thick tissue. Without prevascularization these cells would likely have formed a necrotic core as nutrients and oxygen could not diffuse that deep into the tissue. The cells undergoing vasculogenesis formed a vascular network within the tissue at a scale and density that could not be fabricated using current top-down methods. Notably, we demonstrated that the capillary-scale networks anastomosed to the larger patterned vessels to form a final vascular network that perfused throughout the entire tissue volume. This final network could be set up to resemble a network composed of arteries, capillaries, and veins. Flow could be added directly into a set of 3D-printed channels, the “arteries”, and driven through the vasculogenic “capillaries” towards another set of 3D-printed channels, the “veins”. Not only did our final vascular network perfuse the entire tissue volume, but it more closely recapitulated the multi-scale vessel hierarchy seen in physiology that is more biomechanically efficient than a network composed of only large or small diameter vessels.[174]

Our ECM contained HUVECs and HLFs, but other types of cells could also be suspended in the ECM to create a vascularized parenchyma. The 3D-printed sugar channels have previously been shown to increase the survival and function of hepatocytes

in a tissue due to enhanced perfusion.[21] However, some cell death was still observed for cells that were furthest away from the fabricated channels. The inclusion of the vasculogenic capillary networks should increase perfusion to those otherwise unperfused regions, increasing cell survival even in thicker tissues with higher cell densities.

Although the vascularized tissue we created was already larger than most engineered constructs, the 3D printing method is suitable for scaling production to even larger tissues. We have already demonstrated the ability to print channels as long as 100 mm to increase the tissue size in the x-y plane (Figure 2.10 E). To scale in the z-direction, we could add more layers of parallel channel sets on top of each other using the same method as we used for two layers here. In between each layer of channels we would print a layer of PDMS support to separate the additional set of channels from the previous set. Since all the channels within a set layer are connected, we could seed cells in larger vascular constructs just as easily and quickly as we did here regardless of the size, through a single injection of suspended cells and gravity-driven flow.

Since the construct was not enclosed in PDMS on top like most microfluidics, the vascularized tissues could easily be taken out of the PDMS support using a scalpel or biopsy punch and implanted *in vivo*. For cells within a thick engineered tissue to survive, the tissue must quickly anastomose to the host vascular networks and become perfused. Pre-vascularized tissues with organized vascular geometries have shown success in stimulating vascular invasion and integration and in restoring perfusion to ischemic tissues in a host upon implantation.[6,44,172] Thus, the organized 3D-printed channels may enhance tissue integration with a host, while the vasculogenic networks would enable a

greater extent of perfusion throughout the entire tissue. If the vascular network is sufficiently interconnected through the vasculogenic capillary networks, anastomoses at any site around the periphery of the implanted tissue could perfuse the whole tissue volume.

Combining both the top-down and bottom-up approaches to engineering vasculature imparts the major benefits without the negatives of each approach. The top-down 3D-printed networks provide immediate perfusion to the tissue, control over vascular geometry and organization, and the ability to control flow within the vessels. The bottom-up vasculogenic networks can form dense capillary-scale networks over time throughout the entire tissue with little additional effort or time to fabricate, but would not receive the necessary nutrients to survive in thicker tissues without prefabricated channels. Furthermore, the 3D printing approach can be scaled to produce larger tissues that could also include different cell types or more complicated vascular geometries. Improvements in 3D-printing technology in the future may enable fully-controlled top-down fabrication methods to generate large vascularized tissues with capillary-scale vessels, but the time required to print and the sensitivity of cells to shear stress currently limit the field. 3D-printed sacrificial sugar and the technology and methods developed here could be utilized to rapidly generate centimeter-scale vascularized tissues.

2.4 Materials and Methods

Preparation and 3D-printing of carbohydrate glass:

A mixture of 70g isomalt, 7 g dextran (86 kDa), and 70 ml reverse osmosis water

(Millipore) was warmed to 155° C to remove most of the water and form a liquid glass. The hot mixture was poured into 30 ml syringes and allowed to cool, then stored at 27° C before printing. To print, the sugar was heated to 130° C. Custom Python scripts were developed to generate the 3D motion control GCode used to drive the machine via open-source ReplicatorG software. Carbohydrate- glass lattices were printed under nitrogen pressure with pneumatic control through a 22-gauge steel nozzle.

Spray-coating:

PDLGA or PCL was dissolved in chloroform at a concentration of 5 mg/mL. A Badger Air-Brush Model 175-7 was modified to attach a 500 mL vial containing the polymer solution for spraying and a nitrogen gas line for air pressure. Printed sugar constructs were placed on a PDMS-coated 150 mm diameter glass petri dish. Each sugar construct was sprayed with the polymer solution for 2 seconds, then dried with nitrogen gas. Constructs were then rotated 90 degrees and this process was repeated three more times. Constructs were then flipped over and sprayed four more times. Constructs were stuck to a petri dish by wicking a small drop of chloroform under the sugar in contact with the petri dish, temporarily dissolving the PDLGA coating and melding it to the petri dish.

To remove the PCL coating after flushing out the sugar, lipase from *Pseudomonas sp.* (100 U/mL, PS Lipase, Sigma L9518) was added into the channels to degrade the PCL. The lipase solution was changed every 24 hours and after 48 hours the lipase was removed and washed out with PBS.

Cell seeding in device channels:

To endothelialize the channels, a suspension of HUVECs at a concentration of 16 million/mL was pipetted into the channel port. Cells were left in static culture for one hour to allow them to attach then cells that had not adhered were washed out. We flipped the devices over and repeated this process to seed the tops of the channels.

Introduction of flow in the channels:

To add controlled flow into the branch channel fabricated using PDMS support walls, we inserted tubing connectors directly into the two ports at the ends of the branch vessels. These two tubing lines each had a connected pinch clamp and were joined into a single line using a y-splitter tubing connector. The tubing was connected to a peristaltic pump at a defined flow rate of 1 mL/min. The combined flow was sent back into an EGM-2 media reservoir covering the entire construct. The reservoir setup avoided air bubbles that commonly form in a closed loop flow setup from being pulled through the vessels and damaging endothelial cells. In this setup, media was pulled from the reservoir through the single inlet port into the main channel while air bubbles harmlessly floated to the surface.

2.5 Appendix

We quantified the relation of the 3D printer motor speed to print variable sugar channel diameters. As motor speed increases during the extrusion of the printed sugar channels, the diameter of the printed channels decreases. Using a 22-gauge needle (inner diameter 0.41 mm) extrusion tip and keeping temperature and pressure constant at 129° C

and 40 psi respectively, the printed channel diameter varied from 370 µm at a motor speed of 500 mm/min to 160 µm at a motor speed of 1800 mm/min (Figure 2.11). Although smaller diameter channels could be printed at higher speeds, the handling of the sugar becomes very difficult at lower diameters.

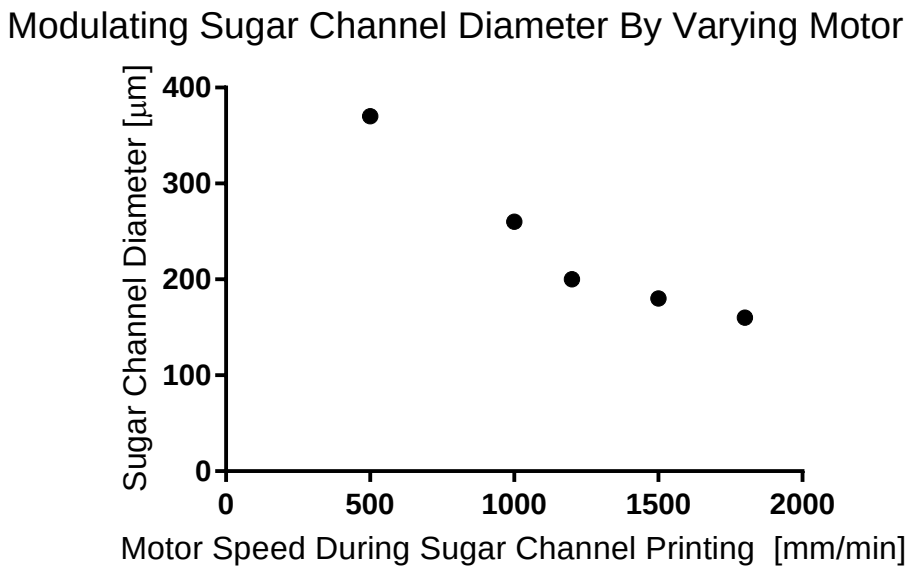

Figure 2.11: 3D-printed sugar channel diameter decreases as the motor speed increases. Each data point is n=1 as measured by a micrometer with error ± 0.01 mm.

2.6 Author Contributions and Acknowledgements

The original 3D printing sugar method, design, and programming was developed by Jordan S. Miller. The upgraded 3D printer hardware and improved sugar formulation in sections 2.2.1 and 2.2.2 were done by me in collaboration with Jordan S. Miller. The experiments in sections 2.2.5 utilizing vasculogenesis to create thick vascularized tissues were done by me in collaboration with H.H. Greco Song. All of the other work from this

chapter including cell culture, 3D printing design and programming, device and tissue fabrication, and data presentation and analysis was done by me.

CHAPTER THREE: 3D-Printed Vascular Networks Direct Therapeutic Vascular Integration in Ischemia

3.1 Introduction

Ischemic cardiovascular disease is the leading cause of morbidity and mortality in the United States. Tissue ischemia results from loss of blood supply to a tissue caused by occlusion of the vasculature that is mostly due to thrombosis, atherosclerosis, or vascular trauma. Leading treatments to restore blood perfusion for late-stage vascular disease include bypass surgery, surgical clot removal, or even amputation in severe cases.[175,176] However, there are a number of risks involved in each of these treatments and not every patient can undergo the treatments due to complicating factors. Furthermore, although large-vessel bypass remains the gold-standard, it cannot treat microvasculature insufficiencies caused by conditions such as coronary microvascular disease or diabetic wound healing.[172] In order to repair the microvasculature, recent tissue engineering research has focused on employing the body's innate vascular remodeling and angiogenesis response to stimulate regrowth of vasculature to damaged tissues. Stimulating host vascular ingrowth using a tissue engineered construct could either replace or supplement traditional treatments and may be useful in future efforts in engineering perfused tissue constructs.

Initial efforts to regrow vascular networks *in vitro* were focused on delivering angiogenic growth factors, such as vascular endothelial growth factor (VEGF) or other soluble factors, but these approaches have had little success in clinical trials, often due to

lack of controlled delivery or off-target effects.[177–179] Cell-based therapies have recently shown promise in forming long-lasting functional vasculature by implanting endothelial cells and stromal cells in mice, however these vessels took weeks to form and resulted in poorly organized vasculature.[41,180] Recently, Baranski *et al.* showed that patterning endothelial cells into aligned solid cylindrical "cords" prior to implantation in mice significantly improved the speed of host vascular invasion and integration and led to a more organized final vascular network architecture.[6,44] Importantly, the patterned geometry was critical, as randomly seeded cells had significantly worse functional outcomes.

Pre-organizing endothelial cells into patterned channels has shown promise for regenerating microvasculature, but the previously used fabrication method used a soft lithography based approach that was labor, time, and skill-intensive, relatively low-throughput, and thus was not easily scalable for creating larger vascularized tissues. It also remained unclear whether the solid cylindrical "cord" geometry used was necessary or whether hollow lumenized vessels could have similar revascularization effects, but the micro-molding fabrication approach could not be used to generate a lumenized vessel geometry. Miller *et al.* showed that 3D-printed carbohydrate-sugar could be used as a sacrificial material to rapidly pattern lumenized vascular networks with precisely controlled geometries, making it an attractive method for creating larger vascularized tissues.[21] In this method 3D-printed sugar networks are encapsulated in ECM then the sugar is dissolved and washed away, leaving hollow channels in the ECM that can be seeded with cells.

In this study we utilized the utilized the improved 3D-printing hardware and sugar-printing methods described in the previous chapter to pattern centimeter-scale vascular networks to stimulate vascular regeneration for the treatment of ischemia. We printed parallel channels and developed a method to seed cells into all the channels simultaneously, increasing the reproducibility, scalability, and ease of patterning vascular network implants. We demonstrated that both endothelialized vessels with hollow lumens and solid endothelial cords could be used to treat ischemic disease in two relevant animal models: a mouse hind limb ischemia model and a rat myocardial infarction model. We further utilized the 3D-printing approach to explore the effects of vascular network geometry in vascular regeneration and the treatment of ischemia.

3.2 Results

To increase the ease and throughput of fabricating vascular networks, we designed a 3D-printed structure where all channels within the construct were seeded with endothelial cells simultaneously. In the previous 3D-printing method, individual channels had to be manually injected with cells one at a time. We printed a sugar structure with 20 parallel 400 μm diameter channels, each 20 mm long and connected to two perpendicular 3 mm diameter reservoirs at each end (Figure 3.1 B). The parallel geometry was initially used based on previous success using parallel channels in the micropatterned endothelial cords. The perpendicular reservoirs were connected to all of the channels and formed a single connected vascular network.

The sugar prints were encapsulated with fibrin gels and sugar was evacuated from

the channels through holes made in each corner of the reservoirs with a 2 mm biopsy punch (Figure 3.1 B). To create endothelial "cords" embedded in the tissue, human umbilical cord endothelial cells (HUVECs) were suspended at a density of $3.5x10^6$ cells/mL in 1 mg/mL collagen gel solution and injected into one of the 3D-printed reservoirs. We then tilted the entire construct at a 30° angle and used gravity to flow cells from the inlet reservoir towards the outlet reservoir and through all of the parallel channels simultaneously. Cells attached to the walls within an hour, forming a confluent monolayer overnight (Figure 3.1 A). After the sugar was washed out, the cell seeding process took about 5 minutes, making it significantly faster than the previous micropatterning method. The cords polymerized at room temperature within about 10 minutes then were covered with cell media and left for approximately 4 hours to contract to roughly 50% of their original diameter, similarly to the original cord study.[181] To cut out the vascular patches for implantation, we used a 10 mm diameter biopsy punch to remove a disc of the fibrin gel encasing the channels (Figure 3.1 B). Our printed constructs covered a total area of 20 mm^2, so four 10 mm diameter vascularized fibrin discs could be cut out of a single construct, but the geometry could be scaled to produce constructs many times larger while still maintaining the same speed of cell seeding to further increase throughput.

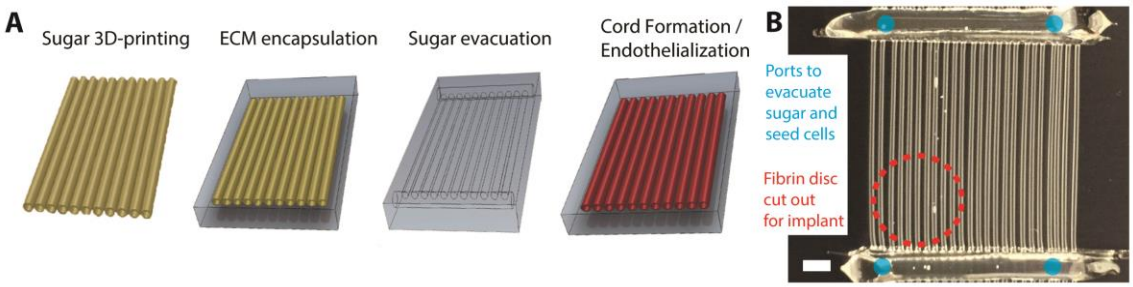

Figure 3.1: A) Schematic of vascular patch (VP) fabrication. Parallel sugar channels are 3D-printed, encapsulated in fibrin ECM gels, and then sacrificial sugar is removed. The remaining hollow channels were seeded with cells (either a collagen and EC "cord" suspension to form solid cylinders, or ECs in media to form endothelialized channels). **B)** Photo of parallel 3D-printed sugar filaments with reservoirs attached to each end. After ECM encapsulation, a biopsy punch was used to create ports (blue circles) in the reservoirs that were used to evacuate the sugar and inject endothelial cells. We injected cells into the top reservoir and used gravity to flow cells towards the bottom reservoir, seeding all parallel channels simultaneously. A 10 mm diameter biopsy punch was then used to cut out a vascularized fibrin patch for implantation (red circle). Scale bar, 2 mm.

To validate the scalability and efficacy of our 3D-printed vascular patches with embedded cords in a larger and more demanding model we used athymic rats with a surgically-induced myocardial infarction, as opposed to the parametrial fat pad of an athymic mouse where the cords were previously implanted.[181] The surgeries were performed in collaboration with vascular surgeons in the Woo lab. To collaborate with a distant lab, we had to produce the sugar constructs and ship them. To ship the constructs while maintaining their structural integrity the constructs were printed, coated with

PDLGA, adhered onto petri dishes that were flushed with dry nitrogen gas, and then sealed with parafilm. Packages were shipped with bubble wrap through commercial shipping companies. Once received, the sugar constructs were UV sterilized and then processed as described previously to create fibrin discs with embedded cord vasculature.

The fibrin discs were placed on the surface of the rat heart spanning the border between ischemic and non-ischemic zones (Figure 3.2 A). Immunohistochemical staining of von Willebrand positive vessels indicated an increase in capillary density in the ischemic zone resulting from the patterned channel gels (VP) (Figure 3.2 B). Aortic flow probe measurements also showed partial rescue of ejection fraction and cardiac output (Figure 3.2 C,D). These metrics of cardiac function were significantly better in the patterned channel experiments than in the sham saline injection control experiment. These results indicate that the cords made using 3D printing successfully recapitulated a similar vascular regrowth response as the micropatterning approach and could functionally treat ischemia in a larger rat heart model.

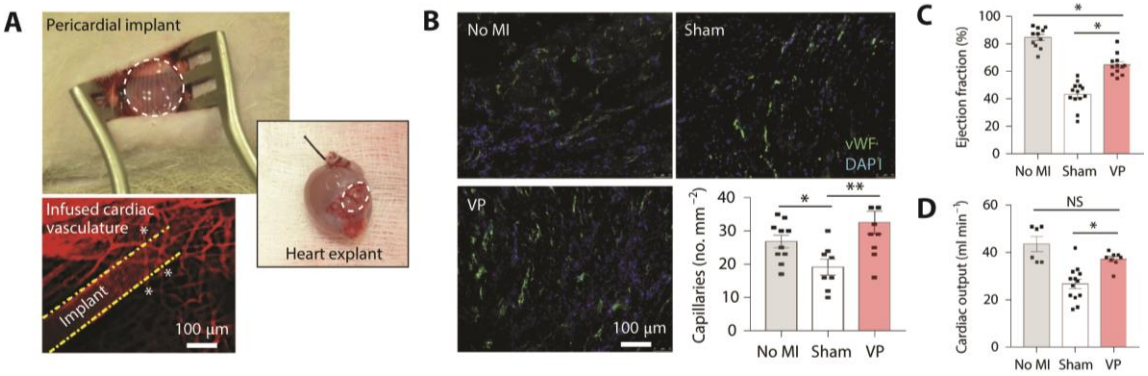

Figure 3.2: Fabricated VPs rescue cardiac function after myocardial infarction in rats. **A)** Top: angled view of a rat undergoing implantation of VPs (dashed circle), placed on the

left ventricle (LV) of the infarcted heart. Middle: an explanted heart shows the vascularized region where the implant was placed 4 weeks prior (inset, dashed circle). Bottom: the DiI-infused vasculature within the explanted patch is shown in red, with channel borders marked with dashed lines and point of connections between the channel and capillaries marked by stars. **B)** Immunofluorescence images of explanted heart sections (15 μ m thick) stained for vWF (green). Histogram shows the vascular density for the no MI, sham and VP groups, quantified as the number of vWF-positive capillaries per mm^2 of cardiac tissue. Heart capillaries were quantified in three fields per heart. Data are expressed as mean ± s.e.m.; sham group N = 8 explanted hearts; no MI and VP groups, N = 10 explanted hearts each; *P < 0.03, **P < 0.01; Mann–Whitney U-test. **C)** Ejection fraction of infarcted hearts in the no MI, sham and VP groups. **D)** Cardiac output of infarcted hearts in the no MI, sham and VP groups. In C-D, data are expressed as mean ± s.e.m.; no MI group N = 11 rats; sham and VP groups, N = 13 rats each; *P < 0.01; NS, not significant; ANOVA with Bonferroni correction.

Although previous work showed that the organized parallel channel geometry was important for stimulating vascular growth, it remained unclear whether the solid endothelial “cords” were necessary or whether endothelialized channels with hollow lumens could have similar effects. However, it was impossible to create endothelialized channels using the micropatterning approach. Using the 3D printing method, we fabricated endothelialized channels by injecting HUVECs suspended in cell media instead of collagen into the inlet reservoir. The cells flowed into all the parallel channels

simultaneously and attached to the channel walls to form confluent endothelial monolayers. 10 mm diameter vascular patches were then cut out for implantation.

To test the efficacy of the hollow endothelialized channels in a functional ischemia setting, we used a mouse hind limb ischemia model. We performed an occlusion of the left femoral artery in nude mice causing a 50% decrease in perfusion of the downstream limb as measured by laser Doppler imaging, and implants were placed onto the occluded region (Figure 3.3 A). For the mice implanted with vascular patches (VP) with parallel endothelialized channels, perfusion to the downstream ischemic limb was rescued within 5 days to be equal to the contralateral, non-ischemic limb (Figure 3.3 B,C). The increase in reperfusion for animals implanted with patterned channels was significantly higher than in sham control experiments that used a saline injection (Figure 3.3 C). Histological analysis showed that newly formed capillaries invaded from the host and directly connected to the pre-patterned channels in our implant (Figure 3.3 E). Thus, the hollow endothelialized channels were able to stimulate vascular integration leading to perfusion similarly to the previously described solid endothelial cords but in a functional ischemia model.

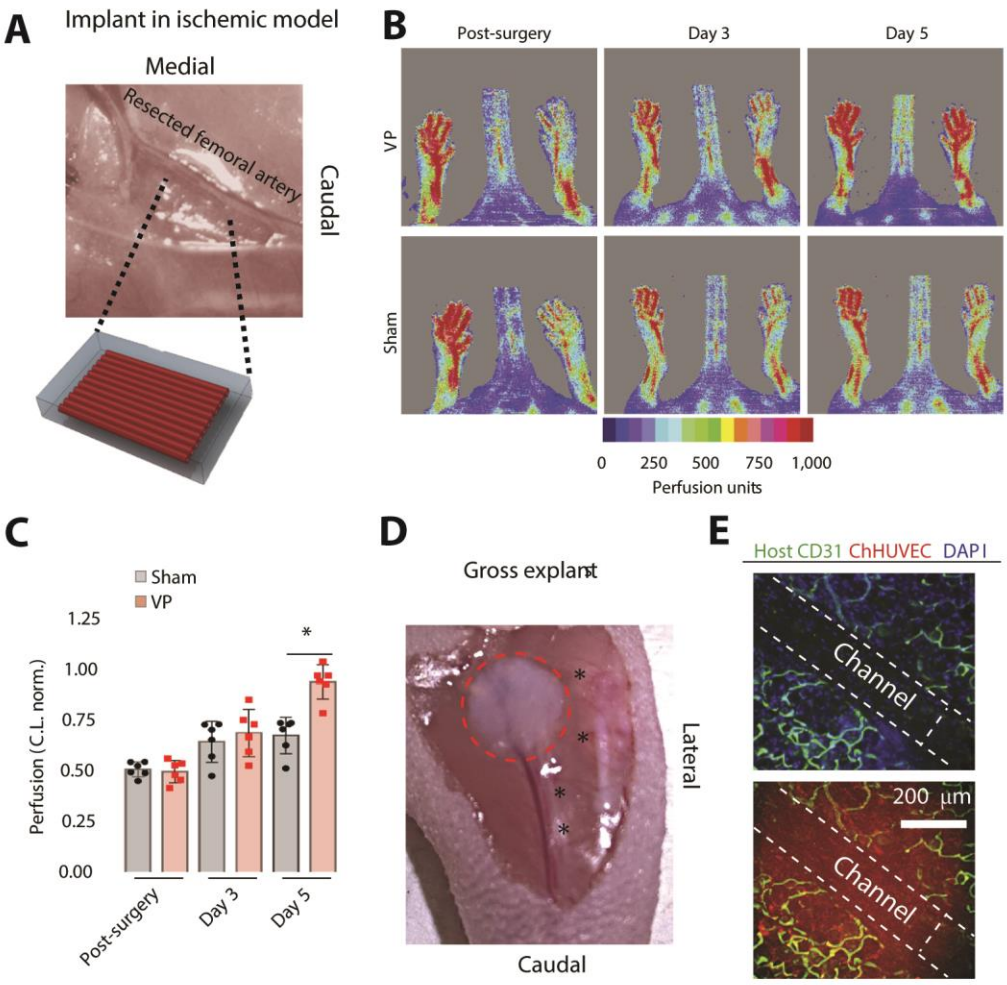

Figure 3.3: A) Image of the VP implantation site within the cauterized femoral artery space. **B)** Laser Doppler imaging of distal limbs over time (post-surgery, day 3 and day 5) in the two groups (VP and sham). **C)** Histogram of perfusion levels of the ischemic limb. Perfusion units of the ischemic limb were normalized to the perfusion units of the contralateral (non-ischemic) limb (C.L. norm.) and are expressed as the fold change. Data are expressed as mean ± s.d.; N = 6 animals per group; *P < 0.01, t-test. **D)** Image of the patches (red circle) retrieved 5 days after implantation (stars mark collateral arteries and veins). **E)** Explanted VPs at day 5 were stained for host vessels (mouse CD31, green) to

show capillary invasion. Endogenous red fluorescence of implanted mCherry HUVECs is also shown. The edges of a single patterned channel are shown with white dotted lines.

To further test the effects of channel geometry in treating ischemia, we modified the 3D-printed channel diameter and geometry (Figure 3.4). We kept the total channel volume roughly the same for the new geometries as the previously used 400 μm diameter parallel channels (Par VP). We printed channels with a higher density and smaller 200 μm diameters (Sm_D VP) and a cross-hatch channel geometry (Grid VP) which had 400 μm diameter parallel and perpendicular channels connected to four separate reservoirs for cell seeding. The grid channels were seeded in the same way as the parallel channels, except that the construct had to be tilted in both the parallel and perpendicular direction to flow cells through all the channels. We implanted the different vascular geometry patches into the ischemic mouse hind limb and compared downstream perfusion to mice implanted with the 400 μm diameter parallel channels (Par VP), 400 μm diameter channels with no endothelial cells (AP), and endothelial cells randomly embedded in a fibrin gel (EP). Although Sm_D VP and Grid VP geometries restored perfusion more than randomly embedded endothelial cells (EP) or empty channels (AP) upon implantation, neither of these vessel geometries led to fully restored perfusion to the ischemic hind limb like the Par VP geometries after 5 days (Figure 3.4). These results suggest that the organized geometric patterning of parallel vessels plays a significant role in vascular integration and that there may be some optimal geometry to induce rapid anastomoses and reperfusion to treat ischemia.

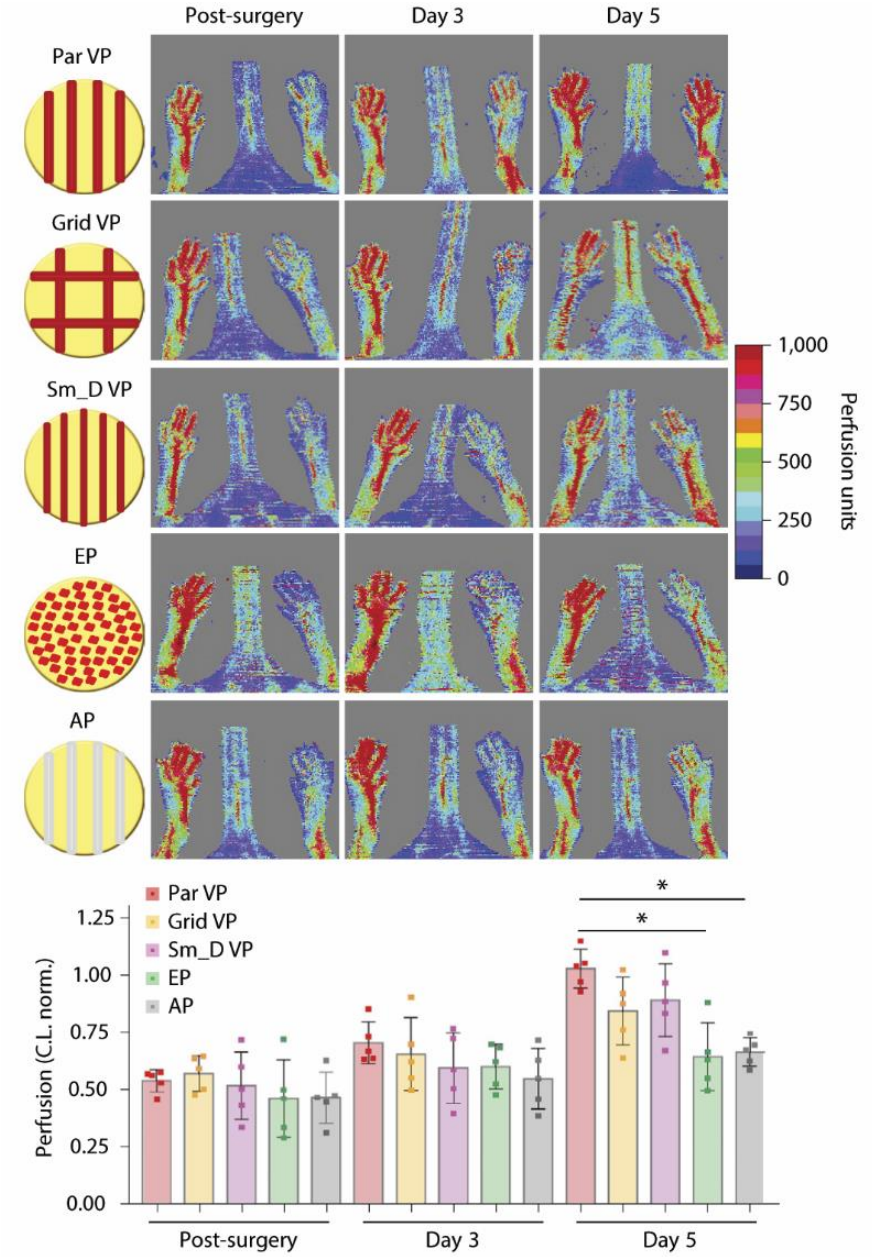

Figure 3.4: Geometric patterning within VPs impacts perfusion performance. Upper: laser Doppler imaging of distal limbs over time (post-surgery, day 3 and day 5) in the five groups: Par VP = VPs where channels were orientated parallel to each other; Grid VP = VPs where channels were orientated orthogonally to each other to form a grid; Sm_D VP = VPs with parallel channels of smaller diameter; EP = endothelial patches

where HUVECs were randomly embedded into the fibrin matrix; and AP = acellular patches containing patterned, not endothelialized channels. Lower: histograms of perfusion levels of the ischaemic limb. Perfusion units of the ischaemic limb were normalized to perfusion units of the contralateral (non-ischaemic) limb (C.L. norm.) and are expressed as the fold change. Data are expressed as mean ± s.d.; N = 5 animals per group; *P < 0.01; ANOVA with Bonferroni correction.

3.3 Discussion

The treatment of ischemia in patients has primarily focused on large caliber bypass grafts, but cell-based approaches offer promise for improving reperfusion at the microvascular level. The 3D printing fabrication method enabled high-throughput production of centimeter-scale vascularized tissue constructs while addressing the skill, time, and scaling constraints associated with micropatterning fabrication. In conjunction with our method to simultaneously seed cells through all connected channels with gravity-driven flow, we could design 3D printed constructs with more and longer channels to generate larger vascularized patches with the only additional time being printing time. Not only could the fabrication method be easily scaled, but constructs could be distributed to distant sites and stored prior to use, increasing their potential for clinical use. Although previous mice studies showed proof that endothelial cords could encourage vascular integration, here we showed the ability of endothelial cords generated using 3D printing to restore function in an infarcted rat heart, a larger animal disease model with clinical relevance.

We further demonstrated that hollow endothelialized channels could stimulate vascular invasion and reperfusion in a host similar to solid endothelial cords. Although either may be effective at stimulating vascular integration and regrowth, hollow channels may lead to different flow patterns upon perfusion and may better mimic physiology. Flow is known to regulate endothelial cell function and flow patterns within the vasculature are largely determined by the vascular geometry.[4,45–47] Thus, varying the engineered vascular geometry may have downstream effects on endothelial cell functions such as permeability and thrombogenicity.

We found that the geometry of our engineered vasculature had a significant impact on reperfusion of the ischemic hind limb, with the 400 μm diameter parallel channels achieving perfusion equal to the non-ischemic contralateral limb after 5 days. In this experiment we kept the total vascular area roughly the same between the tested geometries, but it is possible that higher density 400 μm diameter channels or a higher density cross-hatch geometry work just as well or better. During development, vascular architecture is optimized to minimize construction costs while maintaining function, but it is possible that different geometries than those observed *in vitro* may be optimal or sufficient when engineering the vasculature *de novo*.[7] Further studies on the effects of geometry on vascular integration and surrounding tissue function are needed to determine if hierarchical branching vascular structures are optimal or if a simpler geometry, such as parallel channels, could lead to better outcomes, or to sufficient outcomes at a significantly lower cost. 3D printing is a promising method for vascular tissue engineering because it not only enables scaling of these constructs to larger tissues and

animals, but also control over patterning the vascular geometry. The vascular geometry could also be customized based on the application, desired outcome, and the host vascular context. Although treatment of focal blockages in large arteries has largely been addressed through a combination of percutaneous interventions and surgical bypass grafts, approaches to enhance development of collateral circulation at the level of small vessels, as demonstrated here, could provide additional therapeutic benefit for patients in the future.

3.4 Materials and Methods

Cell culture:

Primary HUVECs (Lonza) were cultured for up to seven passages on 0.1% (wt/vol) gelatin-coated dishes in endothelial cell growth medium (EGM-2; Lonza), maintained at 37 °C in 100% humidified air containing 5% carbon dioxide, with the medium changed every other day. Certificate of analysis for source, identity and infective agents screening was provided by the vendor, and mycoplasma testing was routinely run as good practice. HUVECs labelled with the fluorophore mCherry were used for ex vivo imaging purposes

3D printing of carbohydrate glass patterns:

A mixture of 100 g isomalt, 10 g dextran (86 kDa) and 60 ml reverse osmosis water (≥ 18 MΩ ; Millipore) was warmed to 155 °C to remove most of the water and form a liquid glass. The hot mixture was poured into a 50 ml syringe that was maintained at 110 °C. The syringe was mounted on a ShopBot Desktop, custom-modified 3D printer to use for

additive layer manufacturing with an added RAMBo 1.3 (Ultimachine) circuit board. Carbohydrate glass lattices were printed at 110 °C under nitrogen pressure with pneumatic control through an 18-gauge (0.84 mm internal diameter) steel nozzle, vitrified to 50 °C, and then air-sprayed (Badger Air-Brush Model 175-7) with a 5 mg ml^{-1} solution of poly-d-lactic-glycolic acid (PDLGA; Purac) in chloroform. Glass molds were either immediately encapsulated in extracellular matrix or stored at 27° C for up to a year until use to protect hygroscopic properties.

Casting of vascular structures:

A fibrin gel solution (10 mg ml^{-1}) was generated by mixing fibrinogen, thrombin (2.5 U ml^{-1} final concentration) and phosphate-buffered saline (PBS), and then dispensed to encapsulate the printed carbohydrate glass molds. Fibrin gels were allowed to polymerize for 15 min at 37 °C, placed in PBS, then washed until the carbohydrate glass was completely dissolved. The encapsulated patterns were ported at each corner using a 2 mm biopsy punch and the dissolved sugar solution was flushed out with PBS. A suspension of 3.5×10^6 cells ml^{-1} HUVECs in medium was injected into the ports of the hollow mold architecture and allowed to attach to channel lumens in static culture for 1 h before being placed on a platform rocker in a humidified 37 °C incubator, to induce gravity-driven flow overnight. In some cases, HUVECs were co-injected with 1 mg ml^{-1} type I collagen into the molds. For experiments with randomly patterned HUVECs, cells were mixed into a bulk fibrin gel as it polymerized and then similarly placed on a platform rocker in a humidified 37 °C incubator overnight before implantation.

Rat MI model:

Athymic male rnu rats weighing 170–190 g were obtained from Charles River Laboratories. The continuous delivery of 3% isoflurane was used to anaesthetize the rats. A 16-gauge angiocatheter was used for endotracheal intubation and connected to mechanical ventilation (Hallowell EMC); 1% isoflurane was maintained throughout the operation. A thoracotomy was performed through the left 4th intercostal space, the heart was exposed, and a 7-0 polypropylene suture was placed around the left anterior descending artery 2 mm below the left atrium. The suture was briefly snared to verify the size and location of myocardial ischaemia, based on color change, and permanently tied down to produce a large anterolateral MI. The animals were then randomized to three different groups: healthy rats (no MI), untreated operated rats injected with saline (sham) and rats implanted with patterned constructs (affixed with 7-0 polypropylene suture to the center of the infarct). The thoracotomy was closed in multiple layers and tissue adhesive (VetBond; 3M) was applied over the incision, followed by recovery from anaesthesia. Buprenorphine (0.5 mg kg^{-1}) was administered for postoperative pain control. The LaMorte power calculation was adopted to estimate the sample size to detect a specific effect. All data points collected were included in the analysis. Animals were randomly assigned to groups. All outcomes were assessed disregarding of group allocation. All experiments pertaining to this investigation conformed to the “Guide for the Care and Use of Laboratory Animals”. The protocol was approved by the Institutional Animal Use and Care Committee of the University of Pennsylvania.

Hemodynamic assessment:

Four weeks after left anterior descending artery ligation, all three groups of animals underwent invasive hemodynamic measurements with a pressure– volume conductance catheter (SPR-869; Millar Instruments). The catheter was calibrated via 5-point-cuvette linear interpolation with parallel conductance subtraction by the hypertonic saline method. Rats were anaesthetized as above and the catheter was introduced into the left ventricle utilizing a closed-chest approach via the right carotid artery. Measurements were obtained before and during inferior vena cava occlusion to produce static and dynamic pressure–volume loops under varying load conditions. Data were recorded and analyzed with LabChart software (version 7; AD instruments). Finally, cardiac output was assessed by placing a 2.5 mm peri-aortic Doppler flow probe (Transonic Systems) around the ascending aorta.

Visualization and functional assessment of perfusion in the implanted vasculature:

Five days following implantation, mice were anaesthetized with 3% isoflurane continuously delivered and then intravenously injected with 200 μ l of ulex europaeus agglutinin I (UEA-I) lectin solution (Rhodamine or fluorescein isothiocyanate (FITC)-conjugated; Vectors Lab) or 500 μ l of 1 mg mL^{-1} dextran (70 KDa; FITC or Texas Red conjugated; Molecular probes). Mice were kept under anesthesia (1% isoflurane) for 15 min and then euthanized by cervical dislocation. Implants were harvested in 4% paraformaldehyde and either whole-mount imaged or submerged in OCT (TissueTek), frozen and stored at − 80 °C until imaging. Four weeks after implantation, a subset of rats

were anaesthetized with 3% isoflurane continuously delivered, endotracheally intubated with a 16-gauge angiocatheter connected to mechanical ventilation (Hallowell EMC). A median sternotomy was performed, exposing the heart and ascending aorta. The ascending aorta was clamped and then a 16-gauge needle was inserted into the proximal ascending aorta and connected to pressure tubing with a three way stopcock at its end. An atriotomy was made in the right atrium with scissors and PBS was infused through the aortic needle until effluent from the right atrium was clear. Next, 10 cc of DiI solution (D-282, Invitrogen) was infused through the aortic needle. Hearts were explanted, submerged in OCT, frozen and stored at − 80 °C. Assessment for blood vessels was conducted on cryosections of 100–200 μ m thickness.

Postmortem tissue preparation, staining and imaging:

Animals were euthanized according to protocols approved by the Institutional Animal Use and Care Committee. Tissues and implanted constructs were dissected, OCT-embedded and snap frozen in liquid nitrogen. Histology sections (15 to 100 μ m thickness), whole mount preparation, and haematoxylin and eosin (H&E) staining were performed by standard procedures. A solution of 5% goat serum and 0.1% Triton X-100 in PBS × 1 was used for the 2 h, room-temperature blocking before staining. Primary antibodies were incubated at 4 °C overnight, including rat anti-mouse Ter-119 (1:100; BD Pharmingen), monoclonal rat anti-mouse PECAM-1 (1:100; BD Pharmingen), sheep anti-vWF (conjugated to FITC, 1:100; Abcam), goat polyclonal anti-EphB4 (N-19, 1:100; Santa Cruz) and rabbit polyclonal Ephrin B2 (1:100; Novus Biologicals).

Secondary antibodies conjugated to Alexa (− 488, − 555 and − 647; Molecular Probes) were used at a 1:300 dilution in a 2 h incubation at room temperature. Isolectin B4 (1:200; Vector Labs) and Cy3 and FITC-conjugated anti-α SMA mouse mAb (1:300; Sigma Aldrich) were used under the same conditions as the secondary antibodies. Images were acquired with an LD C-Apochromat × 40, 1.1 numerical aperture water-immersion objective attached to an Axiovert 200M inverted microscope (Zeiss), equipped with a CSU10 spinning disc confocal scan head (Yokogawa Electric) and an Evolve EMCCD camera (Photometrics). A DF5000B Leica fluorescent microscope was used to image 10-μ m thick heart sections. Image processing and analysis was performed with Fiji or ImageJ software FIJI 1.49a (64-bit).

Mouse ischemic hind limb model:

Female nude mice (7- to 10-week-old; Taconic) were anaesthetized with 1–3% isoflurane at flow rate of 1 litre min^{-1} and body temperature was maintained on a circulating heated water pad, during both the surgical procedure and laser Doppler imaging monitoring. Following skin incision, the femoral neurovascular pedicle was visualized under a stereoscope and the left femoral nerve and vein were carefully separated from the femoral artery. The femoral artery abscission was executed below the deep branch by electrocauterization. In this moderate model of hind limb ischemia, the perfusion of the operated distal limb was assessed immediately post-surgery to be half of the contralateral. This model did not develop spontaneous limb necrosis or self-amputation for the duration of the study, mirroring symptoms of significant ischemia, such as the ankle–brachial

index (ABI) and histopathological features, in patients with peripheral artery disease. Once the artery was occluded, implants were positioned with channels in parallel to the downward running femoral artery and the surgical site was sutured; the site was inspected for infection and scarring for the duration of the study. Mice of the sham group underwent electrocauterization of the femoral artery to generate ischemia; no implant was inserted and the site was sutured. Laser Doppler imaging (Moor Instrument) was performed at 16 h and on day 3 and day 5 after surgery. Mice were scanned at a standardized working distance of 32 cm. Blood flow through the feet and the supine inferior limbs was documented as a two- dimensional (2D) color-coded image (scan modus settings: 4–10 ms $pixel^{-1}$, resolution 256 × 256 pixels). Results are expressed as fold increase/decrease of perfusion units, with respect to the contralateral foot (= 1). The LaMorte power calculation was adopted to estimate the sample size to detect a specific effect. All data points collected were included in the analysis. Animals were randomly assigned to groups. All outcomes were assessed disregarding of group allocation. All animal procedures were performed at the Charles River campus animal Facility, Boston University, under a protocol approved by the Institutional Animal Care and Use Committee. All experiments pertaining to this investigation conformed to the “Guide for the Care and Use of Laboratory Animals”.

Statistical analysis:

Data normality was evaluated by the Shapiro–Wilk test. Mann–Whitney U-test was used accordingly to determine statistically significant differences between groups, with a

statistical significance threshold of $P \leq 0.05$. For data assumed to be normally distributed, either a two-tailed Student's t-test or a one-way analysis of variance (ANOVA) with Bonferroni post hoc correction was used, with a statistical significance threshold of $P \leq 0.01$.

3.5 Author Contributions and Acknowledgements

All 3D printing of sugar constructs, fabrication of vascularized tissue constructs, design of different print geometries, and programming was done by me using the improved hardware developed in Chapter Two. M.T. Yang helped with conception of the perpendicular reservoir design and preparing tissues for surgery at the University of Pennsylvania. Rat heart surgeries and associated data analysis were conducted by J.W. MacArthur in Y.J Woo's lab in the Department of Surgery, University of Pennsylvania, Philadelphia, Pennsylvania. Hind-limb ischemia surgeries and associated data analysis were conducted by T. Mirabella in collaboration with C.K. Ozaki's lab at Brigham and Women's Hospital and Harvard Medical School, Boston, MA.

CHAPTER FOUR: Studies of 3D Directed Cell Migration Enabled by Direct Laser Writing of Curved Wave Topography

4.1 Introduction

Cell migration plays a central role in a large variety of biological processes including early embryonic development, immune cell trafficking and surveillance, angiogenesis and blood vessel remodeling, cancer metastasis, and tissue repair.[70–72] When cells migrate, they typically move over and across extracellular matrix (ECM), the polymerized fibrous scaffolds that provide the physical structure of our bodies. Interestingly, the structural organization of the ECM influences how cells adhere and migrate. To study this process in a more controlled setting, researchers generated surfaces patterned with aligned ridges, where it was observed that cells preferentially orient and migrate parallel to the ridges, a phenomenon termed contact guidance.[182] Modulating cell migration speed and direction using topography could be valuable for designing biomedical devices where rapid cell repopulation is critical, such as vascular stents where an endothelial cell monolayer is necessary for proper vascular barrier function and prevention of thrombosis. A major advantage of using topography as a cellular control mechanism is that it is purely physical and does not change the biochemistry of the implant environment.[106]

Cells exhibit contact guidance on a wide variety of substrate materials and feature sizes ranging from tens of nanometers to hundreds of microns.[79,107,108] In general, cells tend to migrate faster on patterned surfaces compared to flat surfaces and migration speed

decreases at longer wavelengths.[107,126–128] To fabricate these surfaces, researchers have predominantly utilized lithography-based approaches to produce square-shaped waveforms composed of flat surfaces and sharp right-angle edges, contrary to physiological settings where cells commonly encounter curved surfaces such as collagen fibers in the ECM or the lumen of a blood vessel. Yet, how cells respond to curved topographies has not been well studied, primarily due to limitations in the ability to fabricate such curved surfaces using standard methods like photolithography.

To better understand how cells migrate on curved topography, we employed an advanced fabrication technique known as Direct Laser Writing (DLW). DLW offers complete 3D spatial control to produce virtually any user-programmed surface with sub-micron resolution. The excellent 3D spatial control of DLW has made it an increasingly popular tool to study the effects of 3D microenvironments in biology and cell migration.[96,131,163–165] We used a commercial DLW system (Nanoscribe Photonic Professional GT, 780 nm) and photoresist (IP-Dip, Nanoscribe GmbH) to generate customizable 3D cell-adhesive surfaces to explore the effects of varying waveform, amplitude, and wavelength on Human Umbilical Vein Endothelial Cell (HUVEC) migration. We then examined both the effects of curved sine wave surfaces on cell migration and the differences in the molecular regulation of directional migration on topography compared to flat micropatterned lines.

4.2 Results

We designed each DLW-printed structure to have an aligned wave topography

spanning an area of 3 x 3 mm^2 and to contain a defined starting location for cells in the center of the pattern. To create the cell starting location, we fabricated a “coliseum-like” circular wall structure with a diameter of 2 mm, a height of 200 µm, and a wall thickness of 15 µm to confine a drop of media with a suspension of cells while the cells attach to the substrate (Figure 4.1 A). Importantly, 50 µm diameter semi-circular arches were designed around the base of the entire wall to allow cells to migrate out of the central region following attachment. To ensure a uniform substrate for cell attachment and migration consisting of one material, we printed a flat surface inside the coliseum walls and all surfaces were coated with 50 µg/mL fibronectin (FN) prior to seeding HUVECs inside the coliseum wall.

To investigate whether wave shape, amplitude, or wavelength had significant effects on cell migration, we printed substrates with peak-to-peak amplitudes of 3, 5 or 10 µm, wavelengths of 5, 10, or 20 µm, and three different waveforms: square, triangle, or sinusoid (Figure 4.1 B). Instead of using a full combinatorial experiment requiring 27 unique patterns, we employed a three-level Taguchi L9 factorial design to collapse the number of patterns to nine while preserving the power to determine the main effect of each parameter on cell migration. Cells were seeded in the center of these substrates and allowed to migrate for 24 hours prior to fixation and staining with crystal violet to visualize the migration front (Figure 4.1 C). On flat surfaces, cells migrated out of the walls isotropically, whereas cells on topographies migrated predominantly parallel to the waves independent of the waveform, indicating that cells were susceptible to contact guidance on DLW-printed substrates.

While the overall ellipsoidal shape of the migration front on patterned surfaces demonstrated preferential migration, it was not clear how the cells were behaving at an individual level. To characterize individual cell migration on the topographies, we tagged the nuclei of the HUVECs by expressing histone H2B-RFP via a lentiviral vector and then recorded single cell migration tracks using time lapse microscopy. Directional migration of individual cells was quantified by splitting total migration speed into its orthogonal components: parallel ($M_{\parallel}$) or perpendicular ($M_{\perp}$) migration relative to the aligned wave patterns (Figure 4.1 D). We found that varying wave shape had a significant effect on total migration speed and $M_{\parallel}$, but no effect on $M_{\perp}$ (Figure 4.1 E). Cells migrated fastest on square waves, followed by triangle waves, and lastly sine waves with average speeds of 31.6 ± 1.4, 28.7 ± 1.5, and 25.1 ± 1.7 μm/hour respectively. We also observed a significant effect of varying wavelength on $M_{\perp}$ (Table 4.S1). In contrast, varying amplitude did not precipitate significant differences for any of the response metrics. Taken together, our data indicate that topography wave shape and wavelength affect migratory behavior of endothelial cells.

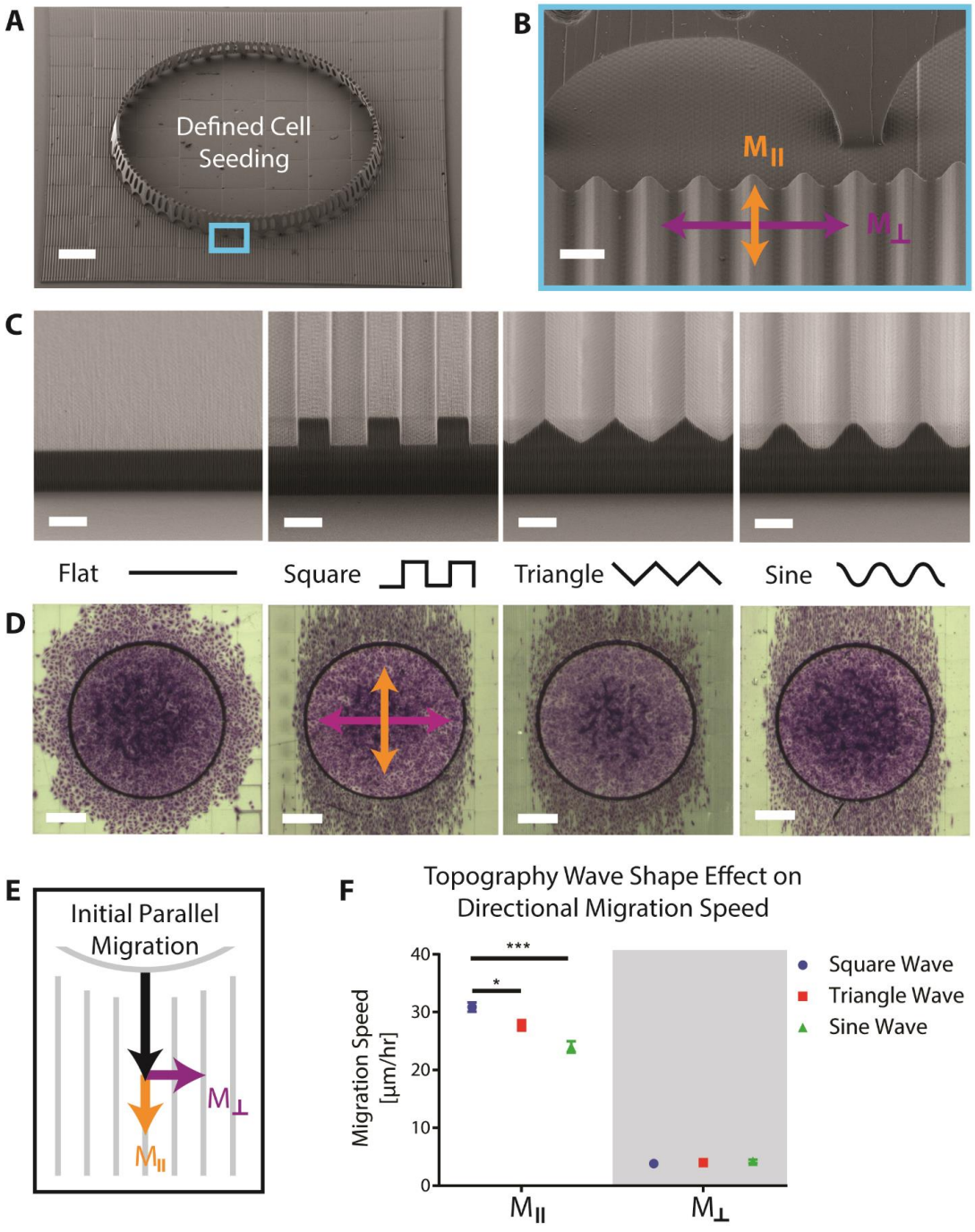

Figure 4.1: SEM images of **A)** a single printed test structure with center "coliseum" surrounded by aligned square wave topography, scalebar 300 μm, and **B)** magnified image of wall arches that allow cells to migrate out following initial seeding, scalebar 20

μm. **C)** SEM images of the outer edges of different topography waveforms with 10 μm peak-to-peak amplitude and 20 μm wavelength, scalebar 10 μm. **D)** Optical images of the cell migration fronts stained with crystal violet after 24 hours on the different topography shapes, scalebar 500 μm. **E)** Schematic of cell migration speed broken into its orthogonal components, $M_{\parallel}$ and $M_{\perp}$. **F)** Plot showing values of $M_{\parallel}$ and $M_{\perp}$ for different waveform shapes (error bars represent mean ± SEM).

Whereas a number of studies have shown that square wave features with dimensions as small as 35 nm can direct cell migration, the upper limit of feature sizes that a cell will respond to is not well defined, especially for curved topographies.[124] We proceeded to explore longer wavelength sine wave topographies by printing sine waves with a fixed 10 μm peak-to-peak amplitude and wavelengths of 20, 50, 100, or 150 μm (Figure 4.2 A). We observed that as wavelength increased, the shape of the cell migration front transitioned from visibly elliptical to a more isotropic migration pattern resembling that of a flat surface (Figure 4.2 B). These findings were corroborated by single-cell analysis, which showed slower $M_{\parallel}$ and faster $M_{\perp}$ migration speeds as wavelength increased (Figure 4.2 C,E). Variability of the angle of migration, visualized by rose plot histograms, also increased at longer wavelengths (Figure 4.2 D). Although $M_{\parallel}$ was only significantly faster on the 20 μm wavelength compared to the flat print, $M_{\perp}$ was significantly decreased at all wavelengths (Figure 4.2 E). Even though the magnitude of the effect of topography on cell migration decreased at longer wavelengths, cells were

still able to sense and respond to sinusoidal topographies with 150 μm wavelength, roughly three to four times the diameter of a single cell.

To quantify the anisotropy of migration we calculated the anisotropy ratio, defined as $M_{\parallel} / M_{\perp}$. The anisotropy ratio was highest for the 20 μm wavelength (~5) and decreased at longer wavelengths, approaching the isotropic ratio of a flat pattern (Figure 4.2 F). Although the anisotropy ratio was lowest for the flat printed patterns, it was not the expected value of one. We compared flat patterns printed using DLW with those with a flat spin coated surface and found differences in $M_{\parallel}$ between the two (Figure 4.2 E,F). SEM imaging of the flat printed topographies showed the presence of aligned nanoscale topography formed from incomplete voxel overlap between printed lines (Figure 4.S1). These small aligned grooves were approximately 100 nm deep and spaced at the width of one voxel (300 nm) from each other and were enough to significantly increase $M_{\parallel}$ speed on "flat" printed patterns when compared to the spin coated migration (Figure 4.2 E). Nonetheless, the topographies of all substrates were printed in the same orientation using the same printing parameters, allowing us to make controlled comparisons within our system framework.

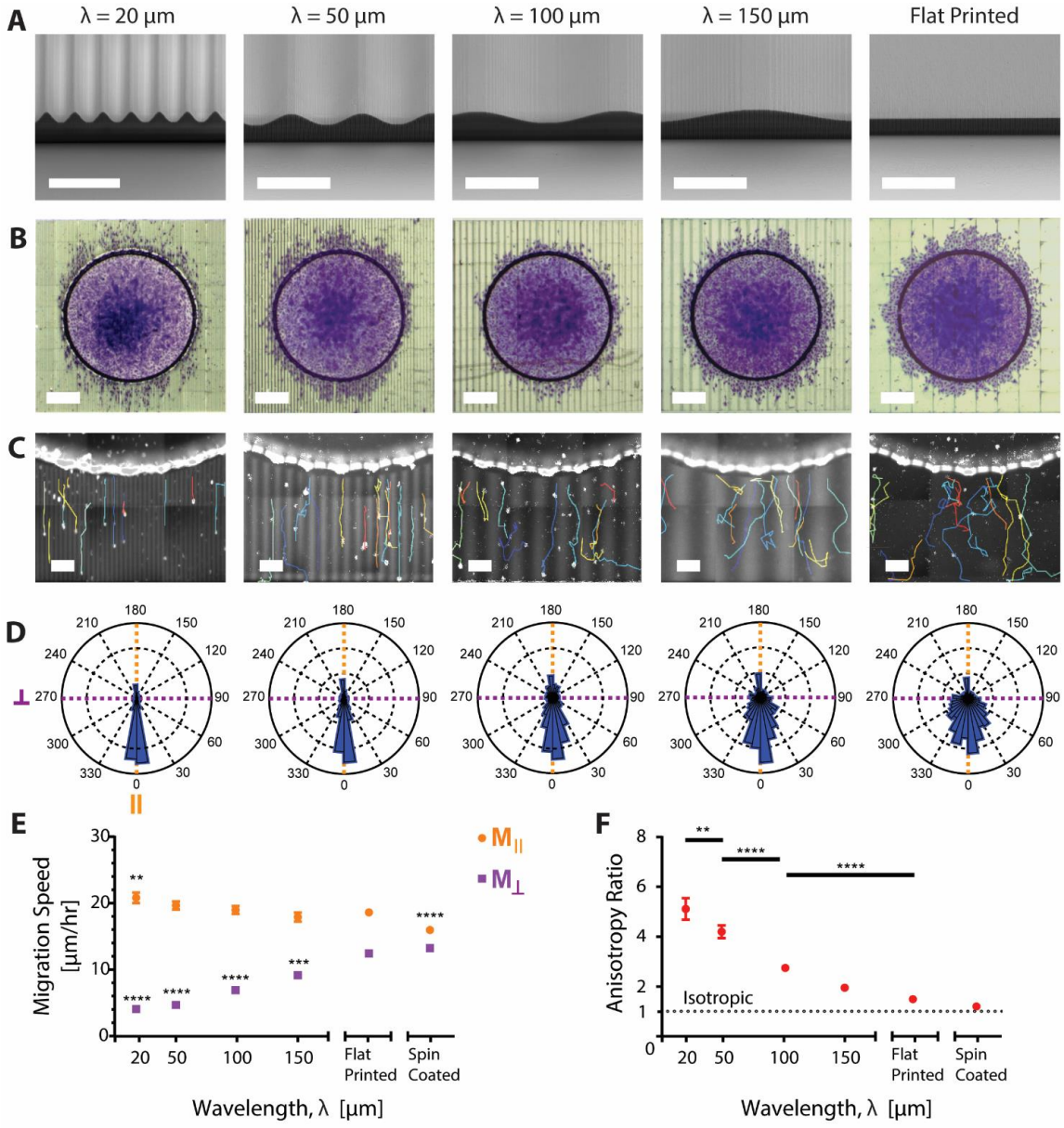

Figure 4.2: **A)** SEM images of sine-wave topography prints with varying wavelength. Scale bar, 50 µm. **B)** Optical images of the cell migration front on the varied wavelength (λ) sine waves. Cells were fixed and stained with crystal violet. Scale bar, 300 µm. **C)** Representative single cell tracks output from Trackmate overlaid onto an image of H2B-RFP tagged cell nuclei. Printed patterns are autofluorescent and thus visible along with cell nuclei. Higher intensity areas denote the peaks of the sine waves while lower

intensity areas denote the troughs. Scale bar, 50 μm. **D)** Rose plot histograms of the angle of cell migration over one-hour time intervals for each wavelength. Angle of migration was rotated so that the initial direction of migration out of the walls was in the 0° direction. Each plot shows combined data with n=8. **E)** $M_{\parallel}$ (orange) and $M_{\perp}$ (purple) cell migration speed with varying wavelength. * indicates significance as compared to the flat printed condition. **F)** Migration speed anisotropy ratio: the ratio of $M_{\parallel}$ / $M_{\perp}$ migration across the various wavelengths. An anisotropy ratio of 1 indicates isotropic migration. *, **, ***, or **** indicate p-value less than 0.05, 0.01, 0.001, and 0.0001 respectively. All error bars represent mean ± SEM.

Directional cell migration arises from cell polarization where cells have a protrusive front and a contractile rear, but the molecular pathways involved are not fully understood. A number of the molecular pathways involved have been revealed by 2D cell migration studies using microcontact printing, a form of soft lithography, to pattern adhesive ligands. These studies have found that three of the major molecular drivers in directional migration are non-muscle myosin IIB (MIIB), which forms contractile actomyosin bundles at the cell rear and locally inhibits protrusion initiation, phosphoinositide 3-kinase (PI3K), which regulates a number of pathways involved in actin cytoskeletal remodeling in cell migration, and Rac1, which locally concentrates actin polymerization and lamellipodial protrusion to the cell front.[70,80]

To explore whether directional migration induced by topography uses the same mechanisms as previously described for flat substrates, we added inhibitors of NMMII, PI3K, and Rac1 to cells on the 20 μm wavelength sine waves and compared the relative change in migration to cells treated with the same inhibitors on flat substrates patterned with fibronectin-coated lines. We approximated a flattened 20 μm wavelength topography by microcontact-printing alternating 10 μm wide lines of cell-adhesive FN and non-adhesive Pluronic (Figure 4.3 A**)**. The flat lines induced cell elongation and directional migration in the parallel direction analogous to our topographies and similar previous reports (Figure 4.3 B).[96,128] Cell seeding density was kept constant and seeding was confined using PDMS rings to keep conditions as similar as possible to that of cells on the sine waves.

As expected, the NMMII inhibitor blebbistatin decreased $M_{\parallel}$ and $M_{\perp}$ on both sine waves and flat lines (Figure 4.3 C,F). The PI3k inhibitor wortmannin reduced cell elongation and modestly decreased directional cell migration (decreased $M_{\parallel}$, increased $M_{\perp}$) for both the sine waves and flat lines (Figure 4.3 D,G). Interestingly, the Rac1 inhibitor NSC increased directional migration of cells on the flat lines, consistent with previous reports, but had the opposite effect for cells on the sine waves.[96] On flat lines NSC increased $M_{\parallel}$ and decreased $M_{\perp}$, but on sine waves NSC decreased $M_{\parallel}$ and increased $M_{\perp}$ (Figure 4.3 E,H). These findings suggest that endogenous Rac1 may

suppress directional migration on flat surfaces, but is in fact important for mediating topography-induced directional migration (Figure 4.3 H).

One of the hypothesized underlying causes of contact guidance is the regulation of focal adhesion (FA) area by physical topography, where FA elongation is constrained in the perpendicular direction, leading to proportionally more parallel FAs.[125,142,147] Results showed that cells on the sine waves had significantly less FA formation along the peaks of the waves when treated with NSC (Figure 4.3 I). Quantification revealed significantly higher average FA area and length for control versus NSC conditions (Figure 4.3 K,L). In contrast, cells on flat FN lines had the same amount of FA formation in the control and NSC conditions (Figure 4.3 J,K,L). Thus, the reduction in directional migration caused by NSC may be mediated by a reduction of FA area and length leading to diminished cell polarization.

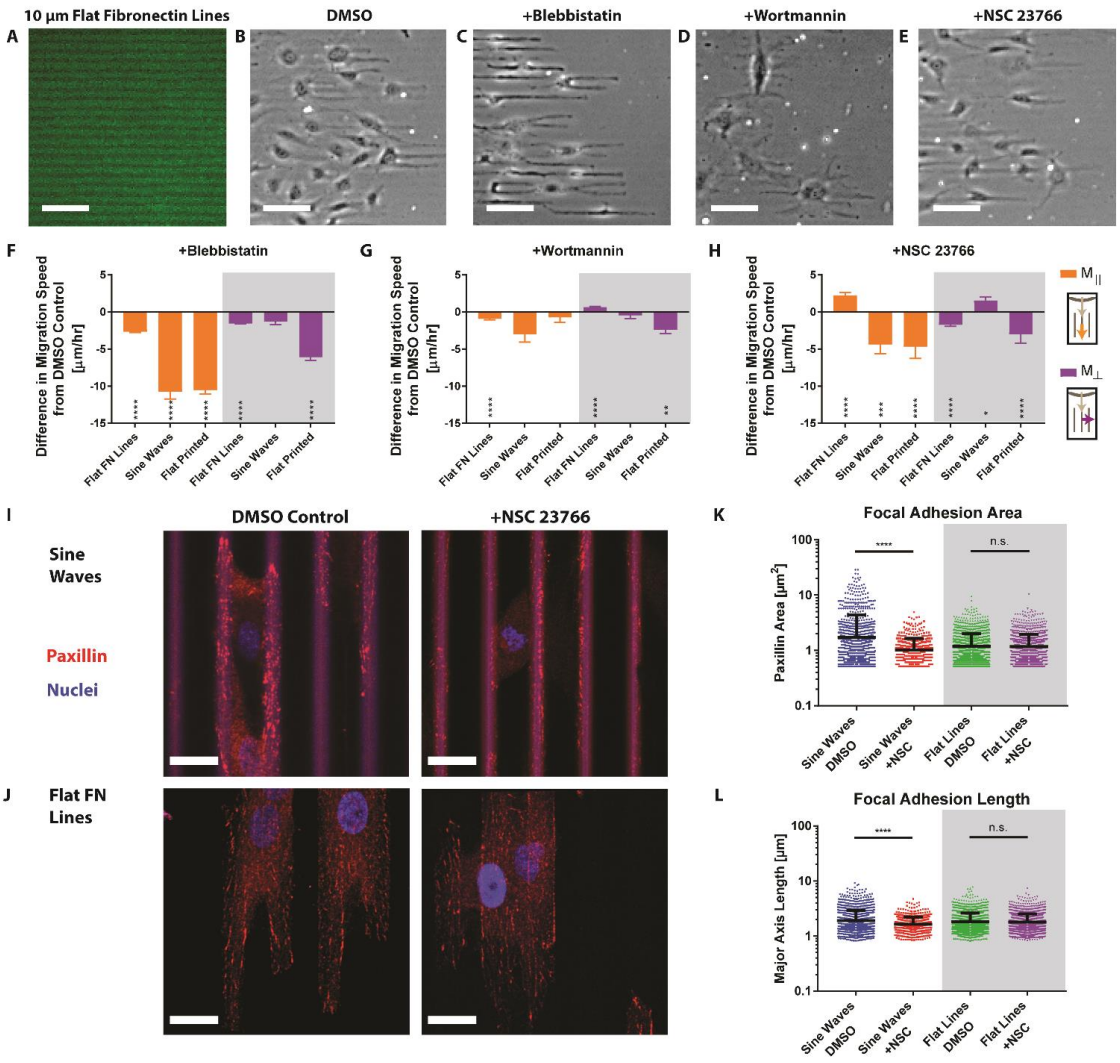

Figure 4.3: **A)** Microcontact-printed flat fluorescent green fibronectin lines of 10 µm width. **B)** Cells were seeded in a circle then migrated out along the lines, left to right. Scale bar, 100 µm. **B)** DMSO, **C)** blebbistatin, **D)** wortmannin, or **E)** NSC 23766 was added 6 hours after seeding. Cell migration on flat FN lines, sine waves, or flat printed patterns was recorded and compared to the DMSO control for **F)** blebbistatin, **G)** wortmannin, or **H)** NSC (error bars represent mean ± SEM). **I)** Confocal imaging of cells migrating on sine waves stained for paxillin and cell nuclei with either DMSO (left) or

NSC (right) added. Scale bar, 20 μm. **J)** Cells migrating on flat FN lines stained for paxillin and cell nuclei with either DMSO (left) or NSC (right) added. Scale bar, 20 μm. Quantification of **K)** focal adhesion area and **L)** focal adhesion length for each condition (error bars represent mean ± SD). *,**,***, or **** indicate p-value less than 0.05, 0.01, 0.001, and 0.0001 respectively.

4.3 Conclusions

This study highlights that cell migration is different on curved topographies compared to the traditional square wave topographies and that DLW is an excellent tool for producing such curved structures at the relevant length scales. This approach enabled us to rapidly identify how different parameters such as waveform, wavelength, and amplitude impact contact guidance. While the field has largely presumed that guidance by adhesive patterns such as parallel lines and by topographic features would occur via a common mechanism, our results suggest important differences between the two processes, specifically emphasizing an important role for the Rac1 GTPase in topography-induced guidance of cell migration. Given the prominence of curved features in native tissues, for example the cylindrical fibers of different extracellular matrix scaffoldings or natural folds of various planes separating different tissue compartments such as blood vessel or intestinal lumens, a deeper understanding of how cells sense and respond to such features will be important to further elucidate.

4.4 Materials and Methods

Printing:

Structures were programmed in MATLAB with 500 nm z-steps and 300 nm steps in the x-y plane. Structures were printed using IP-Dip photoresist (Nanoscribe GmbH) onto PET substrates (Melinex 561 1000 gauge, Dupont) to ensure surface adhesion in aqueous solutions for duration of the testing time. After printing, structures were soaked in PGMEA for 40 min. to dissolve any remaining unpolymerized photoresist, then briefly rinsed in NOVEC 7100 (3M) solvent. To ensure complete structure polymerization, prints were exposed to UV light for 20 seconds. The minimum feature sizes, or voxel dimensions for the IP-Dip photoresist with the 25x magnification, 1.4 NA objective used in this study are approximately 500 nm in the x-y plane and 1.5 um along the z axis.

Cell Culture and Seeding:

HUVECs (Lonza) were cultured in EGM-2 media (Lonza) at 37˚ C in a humidified 5% CO2 incubator. Prior to seeding, the surfaces were coated with 50 µg/mL of human fibronectin (FisherSci) for 1 hour then dried using compressed air. To seed cells, a 2 µL droplet of cells (P5-10) at a concentration of 3.3 million cell/mL (6,600 total cells) in EGM-2 was pipetted into the circular wall and allowed to adhere for thirty minutes at 37° C in a humidified dish. Surface tension caused the liquid droplet, and therefore the cells, to remain confined within the walls. After 30 minutes, media was added to the entire dish and cells began to migrate out of the walls through the arches. Cell migration fronts were visualized using phase contrast imaging or fixed with 4% paraformaldehyde and stained with crystal violet (FisherSci).

To reuse DLW structures, cells were removed with 0.05% trypsin and substrates were subsequently cleaned using 10% sodium dodecyl sulfate (SDS) solution left on an orbital shaker for at least 24 hours followed by multiple washes with 70% ethanol and distilled water.

Fractional factorial experimental design:

We used JMP statistical software package to design a fractional factorial experimental design to screen for significant effects of varying wave shape, amplitude, or wavelength on cell migration. Instead of using a full combinatorial experiment requiring 27 unique patterns, we employed a three-level Taguchi L9 factorial design to collapse the number of patterns to nine while preserving the power to determine the main effect of each parameter on cell migration. We used peak-to-peak amplitudes of 3, 5 or 10 μm, wavelengths of 5, 10, or 20 μm, and three different waveforms: square, triangle, or sinusoid, creating nine combinations with the three set points for each of the three variables. The initial amplitude and wavelength values were taken as the range of dimensions from previous literature that showed the highest magnitude and most robust effect on cell migration speed from topography.[107,126–128]

Single-cell tracking experiments:

Cells were recorded using live fluorescence imaging, then cell position tracks were output using the FIJI plugin Trackmate.[183,184] Cell tracks were filtered to only keep those with good fidelity, as measured through Trackmate's "quality" filter. A custom

MATLAB script was used to analyze the tracks. Average migration speeds were calculated for each cell by calculating the total distance traveled for each hour time interval, then averaging all the time intervals together for each single cell track. To get the final value shown in figures, we averaged values for all cell tracks together over multiple experiments. The angle of migration was calculated for each one-hour interval for each cell and plotted as rose plot histograms.

Microcontact Printing:

We used microcontact printing to fabricate coverslips with alternating 10 μm wide parallel lines of cell-adhesive fibronectin and 10 μm wide lines of non cell-adhesive Pluronic F-127. 10 μm width raised lines were molded in PDMS from silicon wafers. 50 mg mL^{-1} fibronectin with 1% Alexa-Fluor-488 conjugated FN was adsorbed to PDMS stamps for one hour before inverting onto a UV-ozone treated glass coverslip. Coverslips were then treated with 0.2% Pluronic F-127 solution and subsequently washed in PBS. A 2 μL droplet of cells at a concentration of 3.3 million cells/mL (6,600 total cells) in EGM-2 was seeded in a 2 mm diameter PDMS ring. The PDMS ring was removed after 30 minutes, allowing cells to migrate outward.

Inhibitor Studies:

NSC23766 (50 μM), blebbistatin (50 μM), and wortmannin (50 nM) (Tocris Bioscience), were reconstituted and stored in DMSO. Drugs were added in cell media 6 hours after initial cell seeding and left for 24 hours during imaging.

Focal Adhesion Quantification:

Cells were stained using anti-paxillin antibody (diluted 1:100, BD Biosciences #610568) and an Alexa-647 goat anti-mouse secondary antibody (1:400, Invitrogen #A21236). Confocal imaging was taken using 0.8 µm slice thickness. Four image slices (total 3.2 µm height) encompassing the peaks of the sine waves were stacked using max projection, processed using FIJI's threshold and watershed functions, then analyzed using the "analyze particles" function in FIJI. Data from 10 image stacks was averaged, encompassing 20-30 cells total. To quantify focal adhesion length, particles were fitted with an ellipsoid and the major axis length was measured.

Statistics:

The fractional factorial experimental design was set up and analyzed using JMP statistical software package (SAS) using a least squares fit model. Statistical testing and graphing was done using GraphPad Prism software. Single-cell statistics were conducted using two-way ANOVA with a post-hoc Dunnett test. Focal adhesion quantification statistics were conducted using students t-test to compare DMSO and NSC conditions.

4.5 Supporting Information

Effect on $M_{\perp}$ Migration

Source	t Ratio	Pvalue
Amplitude (3,10)	-1.82	0.0859
Wavelength (5,20)	-2.71	0.0148
Shape [Square]	-0.46	0.6505
Shape [Triangle]	-0.08	0.9405
Shape [Sine]	0.49	0.6300

Table 4.S1: Effect of varying amplitude (3-10 µm), wavelength (5-20 µm), and waveform shape (square, triangle, sine) on $M_{\perp}$ migration speed. Statistical analysis was performed using JMP's linear fit model.

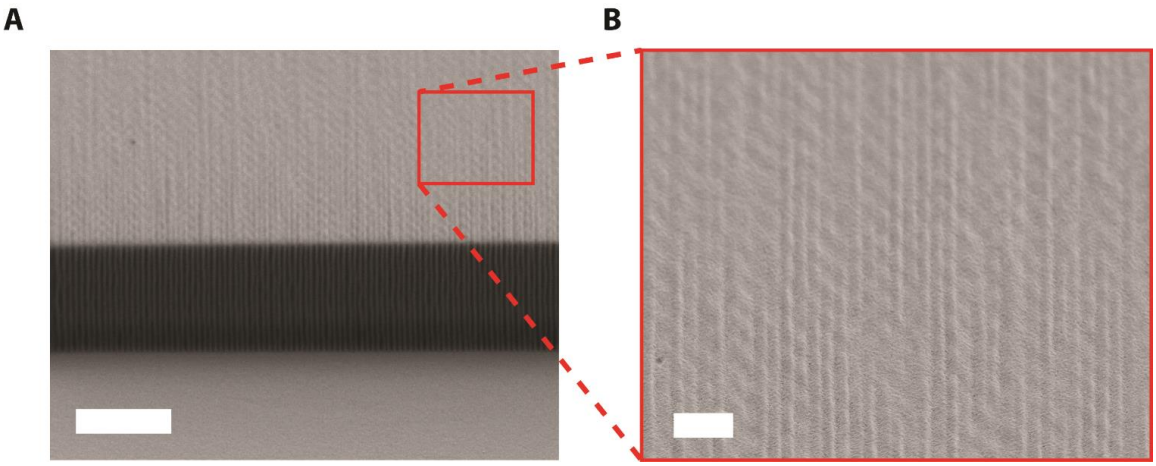

Figure 4.S1: A) SEM image of "flat printed" surface, scale bar 10 µm. B) Higher magnification SEM image showing aligned lines due to incomplete voxel overlap are spaced at roughly the width of one voxel, 300 nm. Scale bar, 2 µm.

4.6 Appendix

Additional data from the previous chapter's project are placed here. We

previously showed the effect of different molecular inhibitors on directional migration including Wortmannin, an inhibitor of PI3k. Wortmannin decreased $M_{\parallel}$ and increased $M_{\perp}$ migration speed on flat fibronectin lines, but did not have significant effects on cells on 20 μm wavelength sine waves (Figure 4.4 B). However, wortmannin is known to have inhibitory effects on pathways other than PI3k including DNA-dependent protein kinase (DNA-PK)[185] and myosin light chain kinase (MLCK)[186]. To test whether the effects of wortmannin were due to PI3k inhibition, we used a more PI3k-specific inhibitor, LY294002. The addition of 10 μM LY294002 had different effects on cell migration than wortmannin. LY decreased both $M_{\parallel}$ and $M_{\perp}$ migration speeds for flat FN lines, sine waves, and flat printed conditions. All of these decreases in migration speed were significant except for sine wave $M_{\perp}$ migration (Figure 4.4 A).

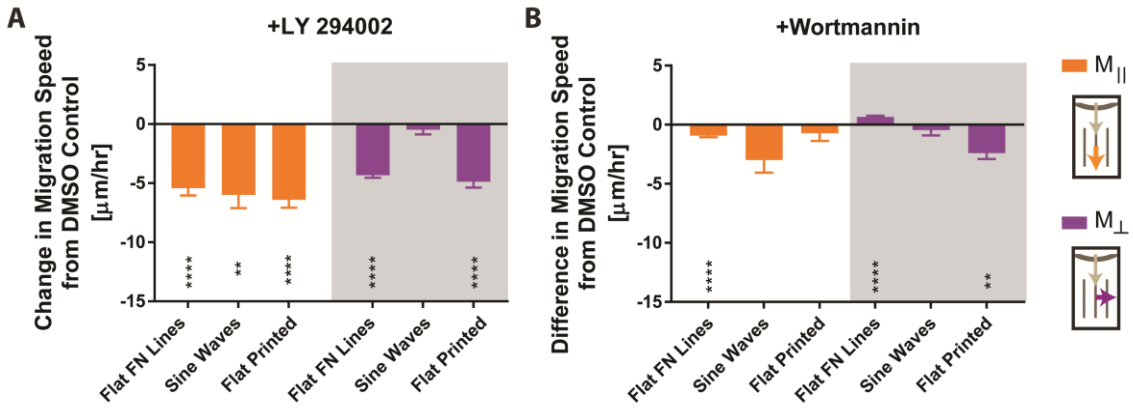

Figure 4.4: Cell migration on flat FN lines, sine waves, or flat printed patterns was recorded and compared to the DMSO control for **A)** LY 294002 (10 µM) or **B)** Wortmannin (50 nM). *,**,***, or **** indicate p-value less than 0.05, 0.01, 0.001, and 0.0001 respectively.

We found that the largest effect on cell migration speed from the sine wave topography was from the 20 µm wavelength patterns so we patterned flat FN lines to approximate that wavelength topography. However, we also investigated the effects of adding different molecular inhibitors on cell migration on longer wavelength sine waves (Figure 4.5). The general trends observed were fairly consistent at all wavelengths for NSC, blebbistatin, and LY. NSC caused a decrease in $M_{\parallel}$ and an increase in $M_{\perp}$ and both blebbistatin and LY decreased both $M_{\parallel}$ and $M_{\perp}$. (Figure 1.5 A,B,D) Wortmannin didn't cause any significant effects on migration speed at any wavelength, but did cause a decrease in $M_{\perp}$ on flat printed patterns (Figure 4.5 C). Thus, the difference in the effect

of migration speed between Wortmannin and LY was not isolated to the 20 µm wavelength sine waves.

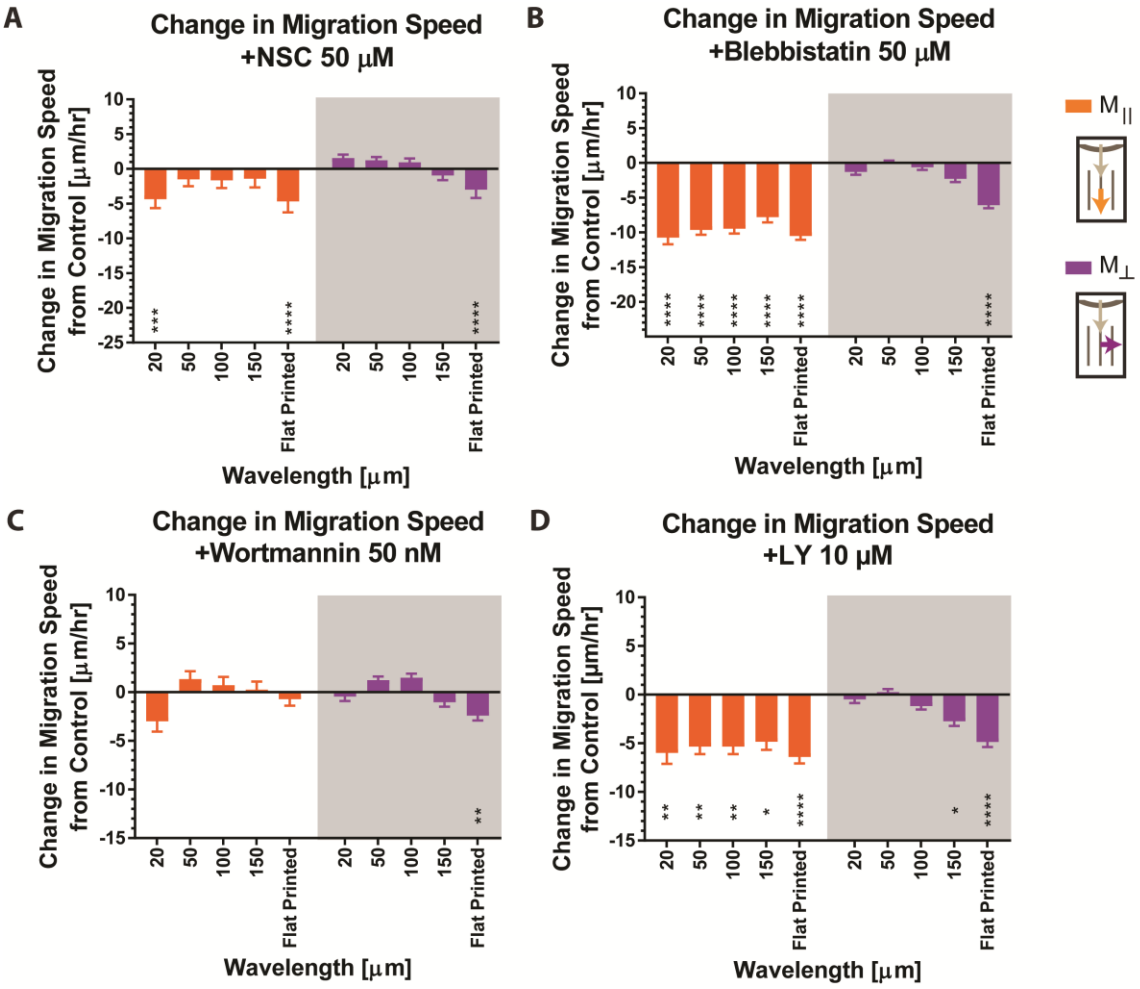

Figure 4.5: Cell migration on sine waves with wavelengths from 20-150 µm or flat printed patterns was measured and compared to the appropriate DMSO control condition to measure the difference in migration speed with the addition of **A)** NSC, **B)** Blebbistatin, **C)** Wortmannin, or **D)** LY. *,**,***, or **** indicate p-value less than 0.05, 0.01, 0.001, and 0.0001 respectively.

To test whether the differential effects of Wortmannin and LY on cell migration was due to dosing concentration, we varied the dosages of Wortmannin from the previously used 50 nM to either 500 nM or 1 µM and varied LY dosage from 10 µM to either 1 or 25 µM. The various dosages showed fairly consistent effects for both Wortmannin and LY, with generally increasing magnitude of the effect at higher dosages (Figure 4.6, 2.7). Wortmann showed small non-significant decreases in $M_{\parallel}$ and an increase in $M_{\perp}$, while LY generally showed a decrease in both. These results indicate that the effect of Wortmannin on directional cell migration in this context is most likely not the result of PI3k inhibition, but on some unknown off-target effect.

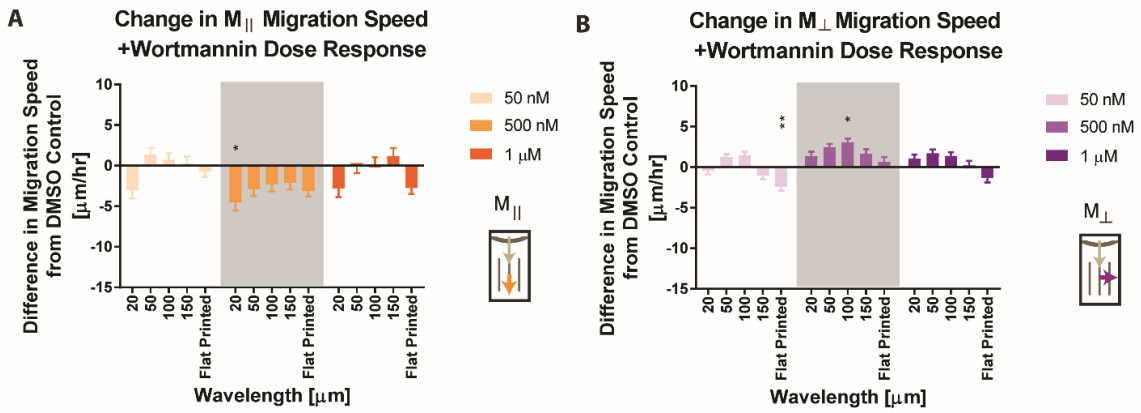

Figure 4.6: Dose response on the difference in cell migration speeds from a DMSO control with the addition of either 50 nM, 500 nM, or 1 µM wortmannin for **A)** $M_{\parallel}$ or **B)** $M_{\perp}$**.** *,**,***, or **** indicate p-value less than 0.05, 0.01, 0.001, and 0.0001 respectively.

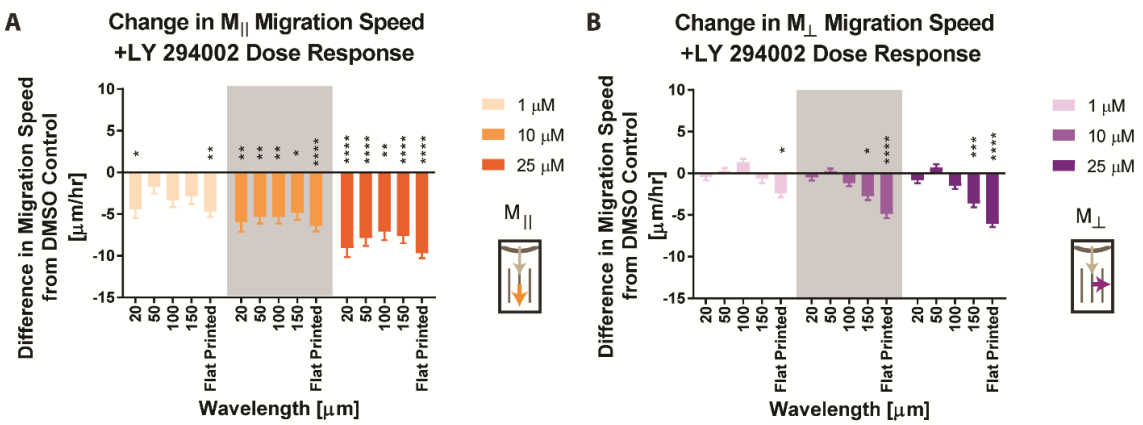

Figure 4.7: Dose response on the difference in cell migration speeds from a DMSO control with the addition of either 1, 10, or 25 µM LY294002 for **A)** $M_{||}$ or **B)** $M_{\perp}$.

*,**,***, or **** indicate p-value less than 0.05, 0.01, 0.001, and 0.0001 respectively.

We also calculated the previously described anisotropy ratio with the added inhibitors NSC, wortmannin, and blebbistatin. All conditions showed a general trend of decreasing anisotropy ratio at longer wavelengths. NSC significantly decreased the anisotropy ratio on the 20 µm wavelength sine waves and blebbistatin decreased anisotropy at 20, 50, and 100 µm wavelengths, but wortmannin did not have any significant effects compared to the control DMSO condition (Figure 4.8).

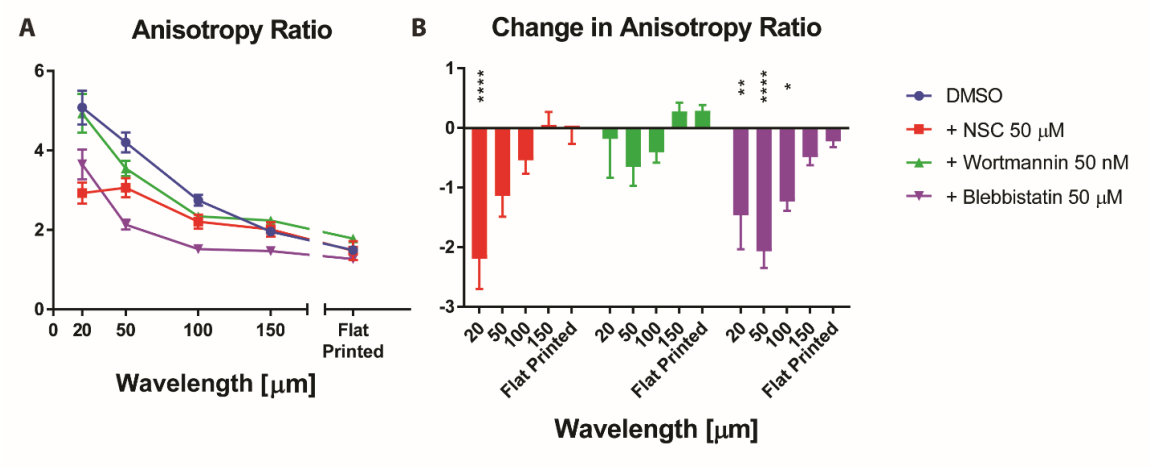

Figure 4.8: A) Anisotropy ratio ($M_{\parallel}$ / $M_{\perp}$) for cells on the different wavelength sine waves and flat printed patterns with the addition of either NSC (50 μM, red), wortmannin (50 nM, green), or blebbistatin (50 μM, purple). **B)** Change in anisotropy ratio for each wavelength from the DMSO control condition with the addition of either NSC (50 μM, red), wortmannin (50 nM, green), or blebbistatin (50 μM, purple). *,**,***, or **** indicate p-value less than 0.05, 0.01, 0.001, and 0.0001 respectively and are only shown in B.

To quantify directional migration in cells in a different way, we used the ratio of cell displacement from the start to end point of a time course divided by the total path distance the cell traveled over that same time. This ratio is commonly referred to as the directionality ratio. A directionality ratio of 1 indicates that the cell traveled in a perfectly straight line while lower values indicate a more meandering cell path and less directional migration. We calculated the directionality ratio for $M_{\parallel}$ cell migration on the different sine wave wavelengths. The directionality ratio was highest for cells on the 20 μm

wavelength sine waves and significantly decreased at 100 or 150 μm wavelength, as well as flat printed or spin coated patterns (Figure 4.9 A). We also investigated how the directionality ratio changed with the addition of the inhibitors NSC, wortmannin, and blebbistatin. Both NSC and wortmannin significantly decreased the directionality ratio compared to the DMSO control only on the 20 μm wavelength sine waves (Figure 4.9 B,C). These results indicate that either the drugs did not have much effect on directionality for the longer wavelengths, or the initial effect of topography on directionality was not enough in the control condition to show a difference once the drugs were added. However, blebbistatin decreased the directionality at all wavelengths, indicating that blebbistatin generically decreases cell directionality regardless of topography (Figure 4.9 D).

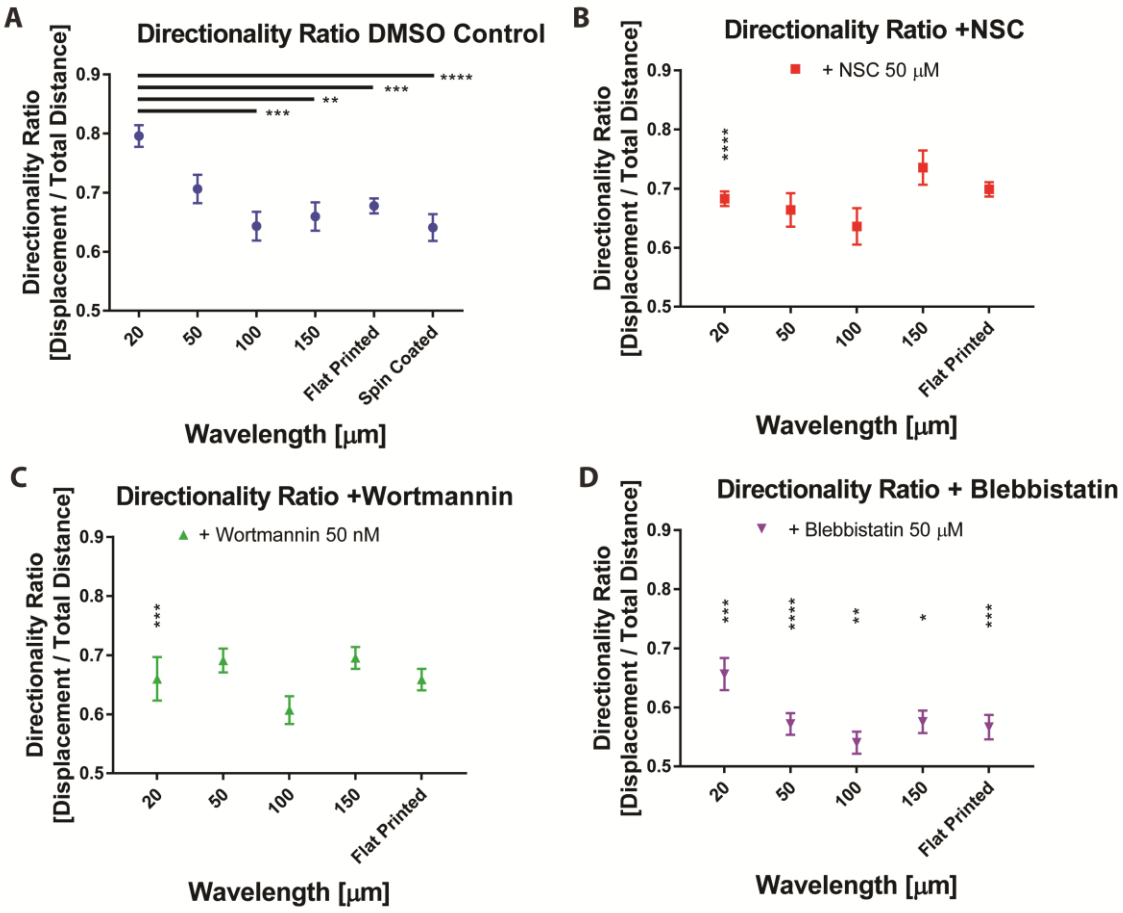

Figure 4.9: Directionality of $M_{||}$ migration on sine waves of different wavelength, flat printed, or spin coated patterns for the **A)** DMSO control condition, or with the addition of **B)** NSC (50 μM, red), **C)** wortmannin (50 nM, green), or **D)** blebbistatin (50 μM, purple). Significance values for A are comparing to other sine wave wavelengths with DMSO but for B, C, or D are comparing the inhibitor condition to the DMSO condition of the same wavelength. *,**,***, or **** indicate p-value less than 0.05, 0.01, 0.001, and 0.0001 respectively.

Using the Nanoscribe with a 25x NA 1.4 objective, the available printing region was a total of 330 μm^2. To print the millimeter-sized coliseum-like wall and the topography, we split the entire print into separate square print tiles. These tiles were printed in sequence to form the entire construct. The individual square tile areas can be seen under microscopy (Figure 4.10 A). Although the interfaces can be seen, each tile's features were printed so that they were flush with the next tile.

Since we printed relatively large constructs, small differences in height or tilt of the print substrate surface could lead to print defects. To avoid parts of the print from getting cut off and to ensure a uniform substrate for cell attachment and migration, a flat 10 µm thick layer of photoresist was printed onto the substrates prior to printing the wall (Figure 4.10 B). The wall and topography was printed on top of this flat base layer. Together, the tiling and base-layer approach allowed printing at high resolution yet across large areas.

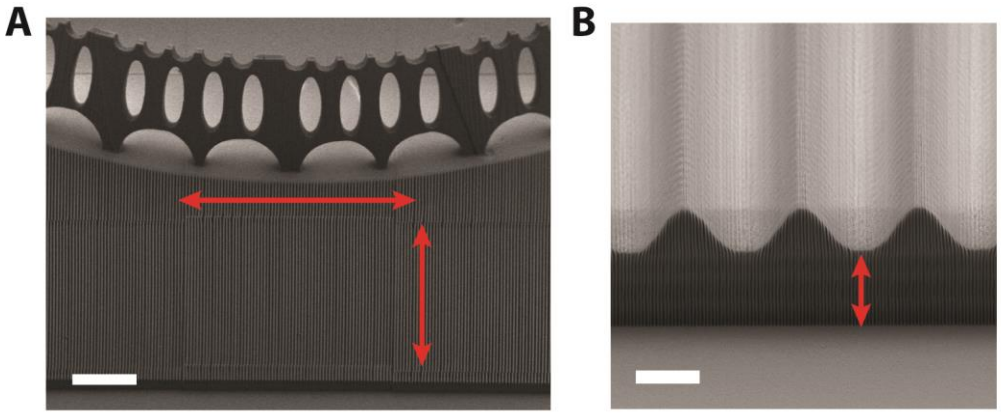

Figure 4.10: A) SEM image of printed constructs. Red arrows show the dimensions of an individual print tile used to print large multi-millimeter scale prints. Scale bar, 100 µm. **B)** SEM image of the edge of a printed construct. The red arrow shows the height of the

10 µm base layer printed underneath the entire construct to avoid issues of surface tilt and flatness during printing over a large area. Scale bar, 10 µm.

4.7 Author Contributions and Acknowledgements

All the DLW printing, design, and programming was done by Rachael K. Jayne, with input from me on overall design of the coliseum wall structure. Experimental design and figure presentation was done in collaboration from R.K Jayne and J. Eyckmans. All the cell experiment work, time-lapse microscopy, and data analysis was done by me, with some assistance from Alessio Tamborini. SEM imaging was done by R.K. Jayne.

CHAPTER FIVE: Conclusions and Future Work

In this dissertation we present three studies of how 3D printing can be utilized for biological applications. The 3D-printed sugar method was improved and used to fabricate complex vascular geometries and thick, densely vascularized tissues. We went on to show that the tissues vascularized using 3D-printed sugar integrated into a host vasculature upon implantation and could restore perfusion to ischemic tissues. We utilized direct laser writing to study the effects of curved wave topography on cell migration. These studies demonstrate the use of different 3D printing technologies for both *in vivo* tissue engineering and *in vitro* studies of cell biology.

5.1 3D printing enables fabrication of complex vascular geometries and densely-vascularized thick tissues

In chapter two we described advances in the method for 3D printing sugar as a sacrificial material to mold vascular networks. We made improvements to the 3D printing hardware, the sugar-making process, and the polymer coating process to protect the sugar during ECM casting. These improvements enabled the generation of vascular networks with increased control, precision, and throughput. We also developed a method to use PCL as the polymer coating and then degrade it away after sugar evacuation to remove any potential barrier for cells.

We then developed a method to 3D-print PDMS to use as a support structure to fabricate more complex vascular networks. Using the printed PDMS walls, we

demonstrated the ability to create various channel geometries including a branched channel that we endothelialized to form a confluent monolayer of cells. Although we demonstrated the method by creating a branched channel embedded in fibrin, we could produce a number of other vascular geometries in the future using the same method due to its flexibility. Any channel geometry that can be printed using sugar can be embedded in a number of different ECM materials, with or without suspended cells, and then endothelialized.

The PDMS wall support structure could also separate channels and enable independent control of fluid flow through each channel. Future work could use this method to spatially pattern different ECM materials, cell types, or soluble growth factors in each channel, allowing for the creation of complex tissue geometries or chemokine gradients within the tissue. The control of channel geometry and direct flow using a peristaltic pump could be used for future *in vitro* studies of how vascular geometry and flow synergistically regulate vascular function. For example, one could study the molecular mechanisms causing atherosclerosis to preferentially occur at branch points *in vivo* or how vascular remodeling is affected by flow patterns and vessel geometry.

In addition to developing the method of using 3D-printed sugar to fabricate vasculature, we integrated a bottom-up approach utilizing vasculogenesis to form capillary networks between the printed vessels. The pre-fabricated 3D-printed channels immediately perfused the tissue to keep cells within it alive while ECs formed capillary-scale vascular networks throughout the rest of the tissue. We showed that the capillary channels anastomosed to the pre-patterned channels, resulting in a perfusable vascular

network that has a high density of vessels ranging from tens to hundreds of microns in diameter. Without the 3D-printed channels, ECs within the core of the thick tissue would likely die and never form capillary networks to perfuse throughout the tissue. Furthermore, the 3D-printed channels may provide a degree of organization to the final vascular network as opposed to networks composed purely through vasculogenesis.

Future work using these vascularized tissues can be conducted to explicitly test the efficacy of the multi-scale vascularized tissues at keeping cells in the thick tissues viable and functional. Parenchymal cells can be added to the ECM, and cell survival and function in the tissue can be compared between a tissue with no vascularization, only 3D-printed vessels, only vasculogenic vessels, and the combinatorial approach. While a number of these experiments can be conducted *in vitro*, the different vascularized tissues can also be cut out of the PDMS support and implanted *in vivo*. Previous results have shown that the tissues with pre-organized vascular networks will rapidly integrate and anastomose into the host vasculature.[6,172,181] Thus, the networks with 3D-printed channels might anastomose faster than tissues without the 3D-printed vasculature when implanted. If the vascular network is sufficiently interconnected through the vasculogenic capillary networks, anastomoses at any site around the periphery of the implanted tissue could perfuse the whole tissue volume. The survival of thick tissues densely laden with cells after implantation would be a significant step for the field of tissue engineering towards the creation of functional tissue replacements. We hypothesize that our densely-vascularized tissues will enhance vascular integration and increase cell survival and function within engineered tissues.

Our 3D printing approach could also be scaled to create even larger vascularized tissues with little additional time or effort. Using the ECM casting and method of simultaneous seeding of the channels through a single connected reservoir, creating larger tissues and seeding more or larger vascular channels would require no additional time. The biggest addition in construction time would be to 3D print larger sugar constructs, which is automated and occurs before cells are introduced so there is no risk for damaging cells with long handling times. We have already demonstrated the ability to print sugar networks as large as 10 x 10 cm^2, and thicker tissues could be created by merely stacking more layers of parallel channels, separated by 3D-printed PDMS, on top of each other. Thus we could fabricate centimeter scale tissues that are pre-vascularized with larger channels using 3D-printed sugar and that form interconnected capillary networks in a matter of days.

5.2 3D-printed vascular networks direct therapeutic vascular integration in ischemia

In chapter three we used the improved 3D printing hardware and methods developed in chapter two to test the efficacy of the 3D-printed vascular channels in integrating into a host vasculature upon implantation and in treating ischemia in two functional animal models. We 3D-printed channels with an attached reservoir so that all the channels could be seeded simultaneously, enabling the fabrication of larger vascularized tissues with very little additional time or effort. We tested the effectiveness of the 3D-printed channels for fabricating solid endothelial “cords” that had previously been shown to stimulate vascular integration and invasion upon implantation in mice.

Cords produced through 3D printing significantly improved vascular function in a more demanding infarcted rat heart model. Our 3D printing method reduced the fabrication time, skill, and effort needed compared to the previous micropatterning method, and was able to restore perfusion in a larger functional ischemia animal model.

We also showed that hollow endothelial channels, as opposed to the solid cylindrical cords, could anastomose into the host vasculature and restore perfusion to an ischemic mouse hind limb. Vascular patches composed of parallel endothelialized channels fully restored perfusion to the ischemic limb within 5 days. The 3D printing approach also enabled us to test the effects of different printed vascular geometries in treating ischemia. We found that the larger 400 μm diameter parallel channels were more effective at restoring perfusion to the ischemic limb than smaller diameter parallel channels or cross-hatch geometry channels. However, in this experiment we kept the total vascular area roughly the same between the tested geometries. Future studies could test the efficacy of tissues with different vascular densities or other more complex vascular geometries at treating ischemia.

Here we demonstrated that vessels constructed using the 3D-printed sugar can integrate into a host vasculature upon implantation, become perfused, and act as a functional conduit to restore blood flow to downstream ischemic tissue. Together with our findings in chapter two, future studies can test the efficacy of tissues with capillary vessels formed through vasculogenesis in addition to the 3D-printed vessels in treating ischemia. These engineered tissues can integrate the organized channels tested here with densely interconnected capillary networks and may be able to treat ischemia more

effectively or more rapidly in more demanding models. Furthermore, our fabrication method can be scaled to create larger tissues that can also include other cell types. Future studies will be needed to test the efficacy of these engineered tissues, or the potential function of any additional cell types upon implantation *in vivo*. The ability to fabricate tissues that can rapidly anastomose upon implantation will enable the generation of larger and more complex engineered tissues that may eventually be able to functionally replace diseased or damaged tissue.

5.3 Studies of 3D directed cell migration enabled by direct laser writing of curved wave topography

As described in chapter four, we used Direct Laser Writing (DLW) to create well-defined curved waveforms similar to those found in physiological settings. Our study demonstrated the potential of using DLW to investigate how a variety of surface features and 3-dimensional structures impacted cell adhesion and migration, a capability that was previously limited using conventional fabrication techniques. We found that directional migration of cells decreased with longer sine wave topography wavelength. Interestingly, directionally migrating cells on 3D sine waves appeared to use different molecular pathways to sense curved topographies than on micropatterned lines. Rac1 inhibition led to decreased directional migration on the sine waves but increased directional migration was observed on 2D patterned fibronectin lines. The field has long presumed that directional cell migration could be studied on 2D surfaces, however our finding suggests that some of the molecular mechanisms may change in 3D. Our results imply that Rac1

differentially affects focal adhesion formation that regulates contact guidance in the 2D and 3D settings, but future studies are needed to fully understand the exact molecular pathways involved.

Using our experimental setup, we can test the effects of different molecular inhibitors or different cell types on the directional migration of cells. To further determine the role of Rac1 on 3D sine waves, future studies could engineer cells that have been genetically modified to express different levels of Rac1 to more specifically target the Rac1 pathway. Further studies could use cells with fluorescently-labeled Rac1 to spatially localize where active Rac1 is in the cells. Other drugs or cell modifications could be used to alter the activity of molecules that are known to be associated with Rac1, to figure out what part of the pathway is affected by topography. All of these perturbations could be compared to cells on 2D FN lines to determine the molecular differences in 2D versus 3D directional migration. Furthermore, it would be interesting to test whether Rac1 plays a similar role in migration on 3D square wave topographies, or if the curvature of the sine wave topography was critical.

DLW grants spatial control over the fabrication of cell-adhesive surfaces that could be used to study a variety of other biological systems and phenomena in the future. We have printed other types of geometries such as porous wall structures for studying cell migration or cancer cell metastasis through a porous ECM, but the DLW has potential to create almost any arbitrary geometry. Although systems with higher complexity are not always necessary or desired for studying specific biological processes, the fabrication ability of DLW makes it attractive for a wide variety of biological studies,

not only in studies of cell biology but also for biomedical device fabrication or *in vitro* platform development.

BIBLIOGRAPHY

1. Feinberg AW, Miller JS. Progress in three-dimensional bioprinting. *MRS Bulletin*. 2017;42(8):557-562. doi:10.1557/mrs.2017.166.

2. Alimperti S, Mirabella T, Bajaj V, et al. Three-dimensional biomimetic vascular model reveals a RhoA, Rac1, and N -cadherin balance in mural cell–endothelial cell-regulated barrier function. *Proceedings of the National Academy of Sciences of the United States of America*. 2017;114(33):201618333. doi:10.1073/pnas.1618333114.

3. Claesson-Welsh L. Vascular permeability—the essentials. *Upsala Journal of Medical Sciences*. 2015;120(3):135-143. doi:10.3109/03009734.2015.1064501.

4. Mehta D, Malik AB. Signaling mechanisms regulating endothelial permeability. *Physiological Reviews*. 2006;86(1):279-367. doi:10.1152/physrev.00012.2005.

5. Griffith CK, Miller C, Sainson RCA, et al. Diffusion Limits of an in Vitro Thick Prevascularized Tissue. *Tissue Engineering.* 2005;11(1-2):257-266.

6. Baranski JD, Chaturvedi RR, Stevens KR, et al. Geometric control of vascular networks to enhance engineered tissue integration and function. *Proceedings of the National Academy of Sciences of the United States of America*. 2013;110(19):7586-7591. doi:10.1073/pnas.1217796110.

7. Kassab GS. Scaling laws of vascular trees: of form and function. *AJP: Heart and Circulatory Physiology*. 2005;290(2):H894-H903. doi:10.1152/ajpheart.00579.2005.

8. Nguyen D-HT, Stapleton SC, Yang MT, et al. Biomimetic model to reconstitute angiogenic sprouting morphogenesis in vitro. *Proceedings of the National Academy of Sciences of the United States of America*. 2013;110(17):6712-6717. doi:10.1073/pnas.1221526110.

9. Zhang B, Montgomery M, Chamberlain MD, et al. Biodegradable scaffold with built-in vasculature for organ-on-a-chip engineering and direct surgical anastomosis. *Nature Materials*. 2016;15(6):669-678. doi:10.1038/nmat4570.

10. Zheng Y, Chen J, Craven M, et al. In vitro microvessels for the study of angiogenesis and thrombosis. *Proceedings of the National Academy of Sciences of the United States of America*. 2012;109(24):9342-9347. doi:10.1073/pnas.1201240109.

11. Kolesky DB, Truby RL, Gladman AS, Busbee TA, Homan KA, Lewis JA. 3D Bioprinting of Vascularized, Heterogeneous Cell-Laden Tissue Constructs.

Advanced Materials. 2014;26(19):3124-3130. doi:10.1002/adma.201305506.

12. Hollister SJ. Porous scaffold design for tissue engineering. *Nature Materials*. 2005;4(7):518-524. doi:10.1038/nmat1421.

13. Hutmacher DW. Scaffolds in tissue engineering bone and cartilage. *Biomaterials*. 2000;21(24):2529-2543. doi:10.1016/S0142-9612(00)00121-6.

14. Reiffel AJ, Kafka C, Hernandez KA, et al. High-Fidelity Tissue Engineering of Patient-Specific Auricles for Reconstruction of Pediatric Microtia and Other Auricular Deformities. *PLoS ONE*. 2013;8(2):e56506. doi:10.1371/journal.pone.0056506.

15. Cohen DL, Malone E, Lipson H, Bonassar LJ. Direct Freeform Fabrication of Seeded Hydrogels in Arbitrary Geometries. *Tissue Engineering.* 2006;12(5):1325-1335

16. Mironov V, Visconti RP, Kasyanov V, Forgacs G, Drake CJ, Markwald RR. Organ printing: Tissue spheroids as building blocks. *Biomaterials*. 2009;30(12): 2164-2174. doi:10.1016/j.biomaterials.2008.12.084.

17. Mannoor MS, Jiang Z, James T, et al. 3D Printed Bionic Ears. *Nano Letters.* 2013;13(6):2634-2639.

18. Norotte C, Marga FS, Niklason LE, Forgacs G. Scaffold-free vascular tissue engineering using bioprinting. *Biomaterials*. 2009;30(30):5910-5917. doi:10.1016/j.biomaterials.2009.06.034.

19. Murphy S V, Atala A. 3D bioprinting of tissues and organs. *Nature Biotechnology*. 2014;32(8):773-785. doi:10.1038/nbt.2958.

20. Shengjie Li S, Zhuo Xiong Z, Xiaohong Wang X, Yongnian Yan Y, Haixia Liu H, Renji Zhang R. Direct Fabrication of a Hybrid Cell/Hydrogel Construct by a Double-nozzle Assembling Technology. *Journal of Bioactive and Compatible Polymers*. 2009;24(3):249-265. doi:10.1177/0883911509104094.

21. Miller JS, Stevens KR, Yang MT, et al. Rapid casting of patterned vascular networks for perfusable engineered three-dimensional tissues. *Nature Materials*. 2012;11(9):768-774. doi:10.1038/nmat3357.

22. Sooppan R, Paulsen SJ, Han J, et al. In Vivo Anastomosis and Perfusion of a Three-Dimensionally-Printed Construct Containing Microchannel Networks. *Tissue Engineering Part C: Methods*. 2016;22(1):1-7. doi:10.1089/ten.tec.2015.0239.

23. Bertassoni LE, Cecconi M, Manoharan V, et al. Hydrogel bioprinted microchannel networks for vascularization of tissue engineering constructs. *Lab on a Chip*. 2014; 14(13):2202-2211. doi:10.1039/C4LC00030G.

24. Abaci HE, Guo Z, Coffman A, et al. Human Skin Constructs with Spatially Controlled Vasculature Using Primary and iPSC-Derived Endothelial Cells. *Advanced Healthcare Materials*. 2016;5(14):1800-1807. doi:10.1002/adhm.201500936.

25. Kolesky DB, Homan KA, Skylar-Scott MA, Lewis JA. Three-dimensional bioprinting of thick vascularized tissues. *Proceedings of the National Academy of Sciences of the United States of America*. 2016;113(12):3179-3184. doi:10.1073/pnas.1521342113.

26. DeForest CA, Polizzotti BD, Anseth KS. Sequential click reactions for synthesizing and patterning three-dimensional cell microenvironments. *Nature Materials*. 2009;8(8):659-664. doi:10.1038/nmat2473.

27. Brown TE, Marozas IA, Anseth KS. Amplified Photodegradation of Cell-Laden Hydrogels via an Addition-Fragmentation Chain Transfer Reaction. *Advanced Materials*. 2017;29(11):1605001. doi:10.1002/adma.201605001.

28. Heintz KA, Bregenzer ME, Mantle JL, Lee KH, West JL, Slater JH. Fabrication of 3D Biomimetic Microfluidic Networks in Hydrogels. *Advanced Healthcare Materials*. 2016;5(17):2153-2160. doi:10.1002/adhm.201600351.

29. Davis GE, Camarillo CW. An α2β1 Integrin-Dependent Pinocytic Mechanism Involving Intracellular Vacuole Formation and Coalescence Regulates Capillary Lumen and Tube Formation in Three-Dimensional Collagen Matrix. *Experimental Cell Research*. 1996;224(1):39-51. doi:10.1006/EXCR.1996.0109.

30. Davis GE, Speichinger KR, Norden PR, Kim DJ, Bowers SLK. Endothelial cell polarization during lumen formation, tubulogenesis, and vessel maturation in 3D extracellular matrices. In: *Cell Polarity 1: Biological Role and Basic Mechanisms*. Cham: Springer International Publishing; 2015:205-220. doi:10.1007/978-3-319-14463-4_9.

31. Davis GE, Camarillo CW. An α2β1 integrin-dependent pinocytic mechanism involving intracellular vacuole formation and coalescence regulates capillary lumen and tube formation in three-dimensional collagen matrix. *Experimental Cell Research*. 1996;224(1):39-51. doi:10.1006/excr.1996.0109.

32. Whisler JA, Chen MB, Kamm RD. Control of Perfusable Microvascular Network Morphology Using a Multiculture Microfluidic System. *Tissue Engineering Part C: Methods*. 2014;20(7):543-552. doi:10.1089/ten.tec.2013.0370.

33. Moya ML, Hsu Y-H, Lee AP, Hughes CCW, George SC. In Vitro Perfused Human Capillary Networks. *Tissue Engineering Part C: Methods*. 2013;19(9):730-737. doi:10.1089/ten.tec.2012.0430.

34. Lin SL, Kisseleva T, Brenner DA, Duffield JS. Pericytes and perivascular fibroblasts are the primary source of collagen-producing cells in obstructive fibrosis of the kidney. *American Journal of Pathology*. 2008;173(6):1617-1627. doi:10.2353/ajpath.2008.080433.

35. Kim S, Lee H, Chung M, Jeon NL. Engineering of functional, perfusable 3D microvascular networks on a chip. *Lab on a Chip*. 2013;13(8):1489. doi:10.1039/c3lc41320a.

36. Jeon JS, Bersini S, Whisler JA, et al. Generation of 3D functional microvascular networks with human mesenchymal stem cells in microfluidic systems. *Integrative Biology*. 2014;6(5):555-563. doi:10.1039/C3IB40267C.

37. Stratman AN, Davis GE. Endothelial cell-pericyte interactions stimulate basement membrane matrix assembly: Influence on vascular tube remodeling, maturation, and stabilization. In: *Microscopy and Microanalysis*. Vol 18. Cambridge University Press; 2012:68-80. doi:10.1017/S1431927611012402.

38. Chen X, Aledia AS, Ghajar CM, et al. Prevascularization of a Fibrin-Based Tissue Construct Accelerates the Formation of Functional Anastomosis with Host Vasculature. *Tissue Engineering Part A*. 2009;15(6):1363-1371. doi:10.1089/ten.tea.2008.0314.

39. Zhang B, Montgomery M, Chamberlain MDD, et al. Biodegradable scaffold with built-in vasculature for organ-on-a-chip engineering and direct surgical anastomosis. *Nature Materials*. 2016;15(6):669-678. doi:10.1038/nmat4570.

40. Levenberg S, Golub JS, Amit M, Itskovitz-Eldor J, Langer R. Endothelial cells derived from human embryonic stem cells. *Proceedings of the National Academy of Sciences of the United States of America*. 2002;99(7):4391-4396. doi:10.1073/pnas.032074999.

41. Koike N, Fukumura D, Gralla O, Au P, Schechner JS, Jain RK. Creation of long-lasting blood vessels. *Nature*. 2004;428(6979):138-139. doi:10.1038/428138a.

42. Bauer SM, Bauer RJ, Liu Z-J, Chen H, Goldstein L, Velazquez OC. Vascular endothelial growth factor-C promotes vasculogenesis, angiogenesis, and collagen constriction in three-dimensional collagen gels. *Journal of Vascular Surgery*. 2005;41(4):699-707. doi:10.1016/j.jvs.2005.01.015.

43. Andrae J, Gallini R, Betsholtz C. Role of platelet-derived growth factors in

physiology and medicine. *Genes & Development*. 2008;22(10):1276-1312. doi:10.1101/gad.1653708.

44. Chaturvedi RR, Stevens KR., Solorzano RD, et al. Patterning Vascular Networks In Vivo for Tissue Engineering Applications. *Tissue Engineering. Part C: Methods.* 2015;21(5):509-517.

45. Lee RT, Kamm RD. Vascular mechanics for the cardiologist. *Journal of the American College of Cardiology*. 1994;23(6):1289-1295. doi:10.1016/0735-1097(94)90369-7.

46. Galbraith CG, Skalak R, Chien S. Shear stress induces spatial reorganization of the endothelial cell cytoskeleton. *Cell Motility and the Cytoskeleton*. 1998;40(4):317-330. doi:10.1002/(SICI)1097-0169(1998)40:4<317::AID-CM1>3.0.CO;2-8.

47. Tarbell JM, Tarbell J, Simionescu M, et al. Shear stress and the endothelial transport barrier. *Cardiovascular Research*. 2010;87(2):320-330. doi:10.1093/cvr/cvq146.

48. Gebala V, Collins R, Geudens I, Phng LK, Gerhardt H. Blood flow drives lumen formation by inverse membrane blebbing during angiogenesis in vivo. *Nature Cell Biology*. 2016;18(4):443-450. doi:10.1038/ncb3320.

49. Lenard A, Ellertsdottir E, Herwig L, et al. In vivo analysis reveals a highly stereotypic morphogenetic pathway of vascular anastomosis. *Developmental Cell*. 2013;25(5):492-506. doi:10.1016/j.devcel.2013.05.010.

50. Song JW, Munn LL. Fluid forces control endothelial sprouting. *Proceedings of the National Academy of Sciences of the United States of America*. 2011;108(37): 15342-15347. doi:10.1073/pnas.1105316108.

51. Galie PA, Nguyen D-HT, Choi CK, Cohen DM, Janmey PA, Chen CS. Fluid shear stress threshold regulates angiogenic sprouting. *Proceedings of the National Academy of Sciences of the United States of America*. 2014;111(22):7968-7973. doi:10.1073/pnas.1310842111.

52. Vickerman V, Kamm RD. Mechanism of a flow-gated angiogenesis switch: early signaling events at cell–matrix and cell–cell junctions. *Integrative Biology*. 2012;4(8):863. doi:10.1039/c2ib00184e.

53. Kyrle PA, Eichinger S. Deep vein thrombosis. *The Lancet*. 2005;365(9465):1163-1174. doi:10.1016/S0140-6736(05)71880-8.

54. Kang H, Bayless KJ, Kaunas R. Fluid shear stress modulates endothelial cell invasion into three-dimensional collagen matrices. *American Journal of*

Physiology. Heart and Circulatory Physiology. 2008;295(5):H2087-2097. doi:10.1152/ajpheart.00281.2008.

55. Chiu J-J, Chien S. Effects of disturbed flow on vascular endothelium: Pathophysiological basis and clinical perspectives. *Physiological Reviews*. 2011; 91(1):327-387. doi:10.1152/physrev.00047.2009.

56. Wong KHK, Chan JM, Kamm RD, Tien J. Microfluidic models of vascular functions. *Annual Review of Biomedical Engineering*. 2012;14:205-230. doi:10.1146/annurev-bioeng-071811-150052.

57. Fowkes FGR, Rudan D, Rudan I, et al. Comparison of global estimates of prevalence and risk factors for peripheral artery disease in 2000 and 2010: A systematic review and analysis. *The Lancet*. 2013;382(9901):1329-1340. doi:10.1016/S0140-6736(13)61249-0.

58. Slovut DP, Lipsitz EC. Surgical technique and peripheral artery disease. *Circulation*. 2012;126(9):1127-1138. doi:10.1161/CIRCULATIONAHA.111.059048.

59. Kakkar AM, Abbott JD. Percutaneous Versus Surgical Management of Lower Extremity Peripheral Artery Disease. *Current Atherosclerosis Reports*. 2015; 17(2):2. doi:10.1007/s11883-014-0479-0.

60. Beningo KA, Dembo M, Wang Y -l. Responses of fibroblasts to anchorage of dorsal extracellular matrix receptors. *Proceedings of the National Academy of Sciences of the United States of America*. 2004;101(52):18024-18029. doi:10.1073/pnas.0405747102.

61. Engler AJ, Sen S, Sweeney HL, Discher DE. Matrix Elasticity Directs Stem Cell Lineage Specification. *Cell*. 2006;126(4):677-689. doi:10.1016/j.cell.2006.06.044.

62. Benya PD, Shaffer JD. Dedifferentiated chondrocytes reexpress the differentiated collagen phenotype when cultured in agarose gels. *Cell*. 1982;30(1):215-224. doi:10.1016/0092-8674(82)90027-7.

63. Huebsch N, Arany PR, Mao AS, et al. Harnessing traction-mediated manipulation of the cell/matrix interface to control stem-cell fate. *Nature Materials*. 2010;9(6): 518-526. doi:10.1038/nmat2732.

64. Khetan S, Guvendiren M, Legant WR, Cohen DM, Chen CS, Burdick JA. Degradation-mediated cellular traction directs stem cell fate in covalently crosslinked three-dimensional hydrogels. *Nature Materials*. 2013;12(5):458-465. doi:10.1038/nmat3586.

65. Friedl P. Prespecification and plasticity: Shifting mechanisms of cell migration. *Current Opinion in Cell Biology*. 2004;16(1):14-23. doi:10.1016/j.ceb.2003.11.001.

66. Pelham RJ, Wang YL. Cell locomotion and focal adhesions are regulated by the mechanical properties of the substrate. *Biological Bulletin*. 1998;194:348-350. doi:10.2307/1543109.

67. Pelham RJ, Wang Y -l. Cell locomotion and focal adhesions are regulated by substrate flexibility. *Proceedings of the National Academy of Sciences of the United States of America*. 1997;94(25):13661-13665. doi:10.1073/pnas.94.25.13661.

68. Hoffman BD, Grashoff C, Schwartz MA. Dynamic molecular processes mediate cellular mechanotransduction. *Nature*. 2011;475(7356):316-323. doi:10.1038/nature10316.

69. Eyckmans J, Boudou T, Yu X, Chen CS. A Hitchhiker's Guide to Mechanobiology. *Developmental Cell*. 2011;21(1):35-47. doi:10.1016/j.devcel.2011.06.015.

70. Petrie RJ, Doyle AD, Yamada KM. Random versus directionally persistent cell migration. *Nature Reviews. Molecular Cell Biology*. 2009;10(8):538-549. doi:10.1038/nrm2729.

71. Friedl P, Wolf K. Tumour-cell invasion and migration: diversity and escape mechanisms. *Nature Reviews. Cancer*. 2003;3(5):362-374. doi:10.1038/nrc1075.

72. Daley WP, Yamada KM. ECM-modulated cellular dynamics as a driving force for tissue morphogenesis. *Current Opinion in Genetics and Development*. 2013;23(4): 408-414. doi:10.1016/j.gde.2013.05.005.

73. Ridley AJ, Schwartz MA, Burridge K, et al. Cell Migration: Integrating Signals from Front to Back. *Science*. 2003;302(5651):1704-1709. doi:10.1126/science.1092053.

74. Bourne HR, Weiner O. Cell polarity: A chemical compass. *Nature*. 2002; 419(6902):21-21. doi:10.1038/419021a.

75. Arrieumerlou C, Meyer T. A local coupling model and compass parameter for eukaryotic chemotaxis. *Developmental Cell*. 2005;8(2):215-227. doi:10.1016/j.devcel.2004.12.007.

76. Carter SB. Principles of cell motility: The direction of cell movement and cancer invasion. *Nature*. 1965;208(5016):1183-1187. doi:10.1038/2081183a0.

77. Lo CM, Wang HB, Dembo M, Wang YL. Cell movement is guided by the rigidity of the substrate. *Biophysical Journal*. 2000;79(1):144-152. doi:10.1016/S0006-3495(00)76279-5.

78. Zhao M. Electrical fields in wound healing-An overriding signal that directs cell migration. *Seminars in Cell and Developmental Biology*. 2009;20(6):674-682. doi:10.1016/j.semcdb.2008.12.009.

79. Nikkhah M, Edalat F, Manoucheri S, Khademhosseini A. Engineering microscale topographies to control the cell–substrate interface. *Biomaterials*. 2012;33(21): 5230-5246. doi:10.1016/j.biomaterials.2012.03.079.

80. Jiménez C, Portela RA, Mellado M, et al. Role of the PI3K regulatory subunit in the control of actin organization and cell migration. *Journal of Cell Biology*. 2000;151(2):249-261. doi:10.1083/jcb.151.2.249.

81. Vicente-Manzanares M, Newell-Litwa K, Bachir AI, Whitmore LA, Horwitz AR. Myosin IIA/IIB restrict adhesive and protrusive signaling to generate front-back polarity in migrating cells. *Journal of Cell Biology*. 2011;193(2):381-396. doi:10.1083/jcb.201012159.

82. Case LB, Waterman CM. Integration of actin dynamics and cell adhesion by a three-dimensional, mechanosensitive molecular clutch. *Nature Cell Biology*. 2015;17(8):955-963. doi:10.1038/ncb3191.

83. Doyle AD, Kutys ML, Conti MA, Matsumoto K, Adelstein RS, Yamada KM. Micro-environmental control of cell migration--myosin IIA is required for efficient migration in fibrillar environments through control of cell adhesion dynamics. *Journal of Cell Science*. 2012;125(Pt 9):2244-2256. doi:10.1242/jcs.098806.

84. Case LB, Waterman CM. Integration of actin dynamics and cell adhesion by a three-dimensional, mechanosensitive molecular clutch. *Nature Cell Biology*. 2015;17(8):955-963. doi:10.1038/ncb3191.

85. Verkhovsky AB, Svitkina TM, Borisy GG. Self-polarization and directional motility of cytoplasm. *Current Biology*. 1999;9(1):11-20, S1. doi:10.1016/S0960-9822(99)80042-6.

86. Kolsch V, Charest PG, Firtel RA. The regulation of cell motility and chemotaxis by phospholipid signaling. *Journal of Cell Science*. 2008;121(5):551-559. doi:10.1242/jcs.023333.

87. Agudelo-Garcia PA, De Jesus JK, Williams SP, et al. Glioma Cell Migration on Three-dimensional Nanofiber Scaffolds Is Regulated by Substrate Topography and Abolished by Inhibition of STAT3 Signaling. *Neoplasia*. 2011;13(9):831-840,

IN15-IN22. doi:10.1593/neo.11612.

88. Ferguson GJ, Milne L, Kulkarni S, et al. PI(3)Kγ has an important context-dependent role in neutrophil chemokinesis. *Nature Cell Biology*. 2007;9(1):86-91. doi:10.1038/ncb1517.

89. Pankov R, Endo Y, Even-Ram S, et al. A Rac switch regulates random versus directionally persistent cell migration. *Journal of Cell Biology*. 2005;170(5): 793-802. doi:10.1083/jcb.200503152.

90. Graupera M, Guillermet-Guibert J, Foukas LC, et al. Angiogenesis selectively requires the p110α isoform of PI3K to control endothelial cell migration. *Nature*. 2008;453(7195):662-666. doi:10.1038/nature06892.

91. Martini FJ, Valiente M, Lopez Bendito G, et al. Biased selection of leading process branches mediates chemotaxis during tangential neuronal migration. *Development*. 2009;136(1):41-50. doi:10.1242/dev.025502.

92. Fischer RS, Gardel M, Ma X, Adelstein RS, Waterman CM. Local Cortical Tension by Myosin II Guides 3D Endothelial Cell Branching. *Current Biology*. 2009;19(3):260-265. doi:10.1016/j.cub.2008.12.045.

93. Xia N, Thodeti CK, Hunt TP, et al. Directional control of cell motility through focal adhesion positioning and spatial control of Rac activation. *The FASEB Journal*. 2008;22(6):1649-1659. doi:10.1096/fj.07-090571.

94. Glogauer M, Marchal CC, Zhu F, et al. Rac1 deletion in mouse neutrophils has selective effects on neutrophil functions. *Journal of Immunology*. 2003;170(11): 5652-5657. doi:10.4049/JIMMUNOL.170.11.5652.

95. Vicente-Manzanares M, Newell-Litwa K, Bachir AI, Whitmore LA, Horwitz AR. Myosin IIA/IIB restrict adhesive and protrusive signaling to generate front-back polarity in migrating cells. *Journal of Cell Biology*. 2011;193(2):381-396. doi:10.1083/jcb.201012159.

96. Doyle AD, Wang FW, Matsumoto K, Yamada KM. One-dimensional topography underlies three-dimensional fibrillar cell migration. *Journal of Cell Biology*. 2009;184(4):481-490. doi:10.1083/jcb.200810041.

97. Baker BM, Chen CS. Deconstructing the third dimension – how 3D culture microenvironments alter cellular cues. *Journal of Cell Science*. 2012;125(13): 3015-3024. doi:10.1242/jcs.079509.

98. Verkhovsky AB, Svitkina TM, Borisy GG. Self-polarization and directional motility of cytoplasm. *Current Biology*. 1999;9(1):11-20, S1. doi:10.1016/S0960-

9822(99)80042-6.

99. Cukierman E, Pankov R, Stevens DR, Yamada KM. Taking cell-matrix adhesions to the third dimension. *Science*. 2001;294(5547):1708-1712. doi:10.1126/science.1064829.

100. Clark P, Connolly P, Curtis AS, Dow JA, Wilkinson CD. Topographical control of cell behaviour: II. Multiple grooved substrata. *Development*. 1990;108(4):635-644.

101. Oakley C, Brunette DM. The sequence of alignment of microtubules, focal contacts and actin filaments in fibroblasts spreading on smooth and grooved titanium substrata. *Journal of Cell Science*. 1993;106(1):343-354.

102. Uttayarat P, Toworfe GK, Dietrich F, Lelkes PI, Composto RJ. Topographic guidance of endothelial cells on silicone surfaces with micro- to nanogrooves: Orientation of actin filaments and focal adhesions. *Journal of Biomedical Materials Research Part A*. 2005;75A(3):668-680. doi:10.1002/jbm.a.30478.

103. Provenzano PP, Inman DR, Eliceiri KW, Trier SM, Keely PJ. Contact Guidance Mediated Three-Dimensional Cell Migration is Regulated by Rho/ROCK-Dependent Matrix Reorganization. *Biophysical Journal*. 2008;95(11):5374-5384. doi:10.1529/biophysj.108.133116.

104. Provenzano PP, Inman DR, Eliceiri KW, et al. Collagen density promotes mammary tumor initiation and progression. *BMC Medicine*. 2008;6(1):11. doi:10.1186/1741-7015-6-11.

105. Sidani M, Wyckoff J, Xue C, Segall JE, Condeelis J. Probing the Microenvironment of Mammary Tumors Using Multiphoton Microscopy. *Journal of Mammary Gland Biology and Neoplasia*. 2006;11(2):151-163. doi:10.1007/s10911-006-9021-5.

106. Miyoshi H, Adachi T, Ju J, et al. Characteristics of motility-based filtering of adherent cells on microgrooved surfaces. *Biomaterials*. 2012;33(2):395-401. doi:10.1016/j.biomaterials.2011.09.094.

107. Kaiser J-P, Reinmann A, Bruinink A. The effect of topographic characteristics on cell migration velocity. *Biomaterials*. 2006;27(30):5230-5241. doi:10.1016/j.biomaterials.2006.06.002.

108. Teixeira AI, McKie GA, Foley JD, Bertics PJ, Nealey PF, Murphy CJ. The effect of environmental factors on the response of human corneal epithelial cells to nanoscale substrate topography. *Biomaterials*. 2006;27(21):3945-3954. doi:10.1016/j.biomaterials.2006.01.044.

109. Karuri NW, Nealey PF, Murphy CJ, Albrecht RM. Structural organization of the cytoskeleton in SV40 human corneal epithelial cells cultured on nano- and microscale grooves. *Scanning*. 2008;30(5):405-413. doi:10.1002/sca.20123.

110. Oakley C, Jaeger NAF, Brunette DM. Sensitivity of Fibroblasts and Their Cytoskeletons to Substratum Topographies: Topographic Guidance and Topographic Compensation by Micromachined Grooves of Different Dimensions. *Experimental Cell Research*. 1997;234(2):413-424. doi:10.1006/excr.1997.3625.

111. Lu X, Leng Y. Quantitative analysis of osteoblast behavior on microgrooved hydroxyapatite and titanium substrata. *Journal of Biomedical Materials Research*. 2003;66A(3):677-687. doi:10.1002/jbm.a.10022.

112. Scheideler L, Geis-Gerstorfer J, Kern D, et al. Investigation of cell reactions to microstructured implant surfaces. *Materials Science and Engineering: C*. 2003; 23(3):455-459. doi:10.1016/S0928-4931(02)00321-1.

113. Rajnicek A, Britland S, McCaig C. Contact guidance of CNS neurites on grooved quartz: influence of groove dimensions, neuronal age and cell type. *Journal of Cell Science*. 1997;110(23):2905-2913.

114. Lu X, Leng Y. Comparison of the osteoblast and myoblast behavior on hydroxyapatite microgrooves. *Journal of Biomedical Materials Research Part B: Applied Biomaterials*. 2008;90B(1):438-445. doi:10.1002/jbm.b.31304.

115. Walboomers XF, Croes HJE, Ginsel LA, Jansen JA. Contact guidance of rat fibroblasts on various implant materials. *Journal of Biomedical Materials Research*. 1999;47(2):204-212. doi:10.1002/(SICI)1097-4636(199911)47:2<204::AID-JBM10>3.0.CO;2-H.

116. Walboomers XF, Monaghan W, Curtis ASG, Jansen JA. Attachment of fibroblasts on smooth and microgrooved polystyrene. *Journal of Biomedical Materials Research*. 1999;46(2):212-220. doi:10.1002/(SICI)1097-4636(199908)46:2<212::AID-JBM10>3.0.CO;2-Y.

117. Li J, McNally H, Shi R. Enhanced neurite alignment on micro-patterned poly-L-lactic acid films. *Journal of Biomedical Materials Research Part A*. 2008;87A(2): 392-404. doi:10.1002/jbm.a.31814.

118. Charest JL, García AJ, King WP. Myoblast alignment and differentiation on cell culture substrates with microscale topography and model chemistries. *Biomaterials*. 2007;28(13):2202-2210. doi:10.1016/j.biomaterials.2007.01.020.

119. Bettinger CJ, Orrick B, Misra A, Langer R, Borenstein JT. Microfabrication of poly (glycerol–sebacate) for contact guidance applications. *Biomaterials*. 2006;

27(12):2558-2565. doi:10.1016/j.biomaterials.2005.11.029.

120. Franco D, Klingauf M, Bednarzik M, et al. Control of initial endothelial spreading by topographic activation of focal adhesion kinase. *Soft Matter*. 2011;7(16):7313. doi:10.1039/c1sm05191a.

121. Biela SA, Su Y, Spatz JP, Kemkemer R. Different sensitivity of human endothelial cells, smooth muscle cells and fibroblasts to topography in the nano–micro range. *Acta Biomaterialia*. 2009;5(7):2460-2466. doi:10.1016/j.actbio.2009.04.003.

122. den Braber ET, de Ruijter JE, Smits HTJ, Ginsel LA, von Recum AF, Jansen JA. Quantitative analysis of cell proliferation and orientation on substrata with uniform parallel surface micro-grooves. *Biomaterials*. 1996;17(11):1093-1099. doi:10.1016/0142-9612(96)85910-2.

123. den Braber ET, de Ruijter JE, Ginsel LA, von Recum AF, Jansen JA. Orientation of ECM protein deposition, fibroblast cytoskeleton, and attachment complex components on silicone microgrooved surfaces. *Journal of Biomedical Materials Research*. 1998;40(2):291-300. doi:10.1002/(SICI)1097-4636(199805)40:2<291::AID-JBM14>3.0.CO;2-P.

124. Loesberg WA, te Riet J, van Delft FCMJM, et al. The threshold at which substrate nanogroove dimensions may influence fibroblast alignment and adhesion. *Biomaterials*. 2007;28(27):3944-3951. doi:10.1016/j.biomaterials.2007.05.030.

125. Ray A, Lee O, Win Z, et al. Anisotropic forces from spatially constrained focal adhesions mediate contact guidance directed cell migration. *Nature Communications*. 2017;8:14923. doi:10.1038/ncomms14923.

126. Kim D-H, Han K, Gupta K, Kwon KW, Suh K-Y, Levchenko A. Mechanosensitivity of fibroblast cell shape and movement to anisotropic substratum topography gradients. *Biomaterials*. 2009;30(29):5433-5444. doi:10.1016/j.biomaterials.2009.06.042.

127. Dalton BA, Walboomers XF, Dziegielewski M, et al. Modulation of epithelial tissue and cell migration by microgrooves. *Journal of Biomedical Materials Research*. 2001;56(2):195-207. doi:10.1002/1097-4636(200108)56:2<195::AID-JBM1084>3.0.CO;2-7.

128. Li S, Bhatia S, Hu Y, et al. Effects of morphological patterning on endothelial cell migration. *Biorheology*. 2001;38(2,3):101-108.

129. Kaiser J-P, Reinmann A, Bruinink A. The effect of topographic characteristics on cell migration velocity. *Biomaterials*. 2006;27(30):5230-5241. doi:10.1016/j.biomaterials.2006.06.002.

130. Mai J, Sun C, Li S, Zhang X. A microfabricated platform probing cytoskeleton dynamics using multidirectional topographical cues. *Biomedical Microdevices*. 2007;9(4):523-531. doi:10.1007/s10544-007-9060-8.

131. Jeon H, Hidai H, Hwang DJ, Healy KE, Grigoropoulos CP. The effect of micronscale anisotropic cross patterns on fibroblast migration. *Biomaterials*. 2010; 31(15):4286-4295. doi:10.1016/j.biomaterials.2010.01.103.

132. Kim D-H, Seo C-H, Han K, Kwon KW, Levchenko A, Suh K-Y. Guided Cell Migration on Microtextured Substrates with Variable Local Density and Anisotropy. *Advanced Functional Materials*. 2009;19(10):1579-1586. doi:10.1002/adfm.200990041.

133. Le Saux G, Magenau A, Böcking T, Gaus K, Gooding JJ. The Relative Importance of Topography and RGD Ligand Density for Endothelial Cell Adhesion. Johannes L, ed. *PLoS ONE*. 2011;6(7):e21869. doi:10.1371/journal.pone.0021869.

134. Hamilton DW, Chehroudi B, Brunette DM. Comparative response of epithelial cells and osteoblasts to microfabricated tapered pit topographies in vitro and in vivo. *Biomaterials*. 2007;28(14):2281-2293. doi:10.1016/j.biomaterials.2007.01.026.

135. Wan Y, Wang Y, Liu Z, et al. Adhesion and proliferation of OCT-1 osteoblast-like cells on micro- and nano-scale topography structured poly(l-lactide). *Biomaterials*. 2005;26(21):4453-4459. doi:10.1016/j.biomaterials.2004.11.016.

136. Wang L, Murthy SK, Fowle WH, Barabino GA, Carrier RL. Influence of micro-well biomimetic topography on intestinal epithelial Caco-2 cell phenotype. *Biomaterials*. 2009;30(36):6825-6834. doi:10.1016/j.biomaterials.2009.08.046.

137. Kolind K, Dolatshahi-Pirouz A, Lovmand J, Pedersen FS, Foss M, Besenbacher F. A combinatorial screening of human fibroblast responses on micro-structured surfaces. *Biomaterials*. 2010;31(35):9182-9191. doi:10.1016/j.biomaterials.2010.08.048.

138. Kidambi S, Udpa N, Schroeder SA, Findlan R, Lee I, Chan C. Cell Adhesion on Polyelectrolyte Multilayer Coated Polydimethylsiloxane Surfaces with Varying Topographies. *Tissue Engineering*. 2007;13(8):2105-2117.

139. Ghibaudo M, Trichet L, Le Digabel J, Richert A, Hersen P, Ladoux B. Substrate Topography Induces a Crossover from 2D to 3D Behavior in Fibroblast Migration. *Biophysical Journal*. 2009;97(1):357-368. doi:10.1016/j.bpj.2009.04.024.

140. Frey MT, Tsai IY, Russell TP, Hanks SK, Wang Y. Cellular Responses to Substrate Topography: Role of Myosin II and Focal Adhesion Kinase. *Biophysical*

Journal. 2006;90(10):3774-3782. doi:10.1529/biophysj.105.074526.

141. Turner AMP, Dowell N, Turner SWP, et al. Attachment of astroglial cells to microfabricated pillar arrays of different geometries. *Journal of Biomedical Materials Research*. 2000;51(3):430-441. doi:10.1002/1097-4636(20000905)51:3<430::AID-JBM18>3.0.CO;2-C.

142. Ventre M, Natale CF, Rianna C, Netti PA. Topographic cell instructive patterns to control cell adhesion, polarization and migration. *Journal of The Royal Society Interface*. 2014;11(100):20140687-20140687. doi:10.1098/rsif.2014.0687.

143. Saito AC, Matsui TS, Ohishi T, Sato M, Deguchi S. Contact guidance of smooth muscle cells is associated with tension-mediated adhesion maturation. *Experimental Cell Research*. 2014;327(1):1-11. doi:10.1016/j.yexcr.2014.05.002.

144. Wang J, Schneider IC. Myosin phosphorylation on stress fibers predicts contact guidance behavior across diverse breast cancer cells. *Biomaterials*. 2017;120:81-93. doi:10.1016/j.biomaterials.2016.11.035.

145. Brown MC, Turner CE. Paxillin: Adapting to Change. *Physiological Reviews*. 2004;84(4):1315-1339. doi:10.1152/physrev.00002.2004.

146. Balaban NQ, Schwarz US, Riveline D, et al. Force and focal adhesion assembly: a close relationship studied using elastic micropatterned substrates. *Nature Cell Biology*. 2001;3(5):466-472. doi:10.1038/35074532.

147. Kubow KE, Conrad SK, Horwitz AR. Matrix microarchitecture and myosin II determine adhesion in 3D matrices. *Current Biology*. 2013;23(17):1607-1619. doi:10.1016/j.cub.2013.06.053.

148. Sheets K, Wunsch S, Ng C, Nain AS. Shape-dependent cell migration and focal adhesion organization on suspended and aligned nanofiber scaffolds. *Acta Biomaterialia*. 2013;9(7):7169-7177. doi:10.1016/J.ACTBIO.2013.03.042.

149. Kubow KE, Shuklis VD, Sales DJ, Horwitz AR. Contact guidance persists under myosin inhibition due to the local alignment of adhesions and individual protrusions. *Scientific Reports*. 2017;7(1):14380. doi:10.1038/s41598-017-14745-7.

150. Wójciak‐Stothard B, Curtis ASG, McGrath M, Sommer I, Wilkinson CDW, Monaghan W. Role of the cytoskeleton in the reaction of fibroblasts to multiple grooved substrata. *Cell Motility and the Cytoskeleton*. 1995;31(2):147-158. doi:10.1002/cm.970310207.

151. Gerecht S, Bettinger CJ, Zhang Z, Borenstein JT, Vunjak-Novakovic G, Langer R.

The effect of actin disrupting agents on contact guidance of human embryonic stem cells. *Biomaterials*. 2007;28(28):4068-4077. doi:10.1016/j.biomaterials.2007.05.027.

152. Frey MT, Tsai IY, Russell TP, Hanks SK, Wang Y. Cellular Responses to Substrate Topography: Role of Myosin II and Focal Adhesion Kinase. *Biophysical Journal*. 2006;90(10):3774-3782. doi:10.1529/biophysj.105.074526.

153. Kulangara K, Yang Y, Yang J, Leong KW. Nanotopography as modulator of human mesenchymal stem cell function. *Biomaterials*. 2012;33(20):4998-5003. doi:10.1016/j.biomaterials.2012.03.053.

154. Ferrari A, Cecchini M, Serresi M, Faraci P, Pisignano D, Beltram F. Neuronal polarity selection by topography-induced focal adhesion control. *Biomaterials*. 2010;31(17):4682-4694. doi:10.1016/J.BIOMATERIALS.2010.02.032.

155. Ramirez-San Juan GR, Oakes PW, Gardel ML. Contact guidance requires spatial control of leading-edge protrusion. Forscher P, ed. *Molecular Biology of the Cell*. 2017;28(8):1043-1053. doi:10.1091/mbc.E16-11-0769.

156. Franco D, Klingauf M, Bednarzik M, et al. Control of initial endothelial spreading by topographic activation of focal adhesion kinase. *Soft Matter*. 2011;7(16):7313. doi:10.1039/c1sm05191a.

157. Calzado-Martín A, Méndez-Vilas A, Multigner M, et al. On the role of RhoA/ROCK signaling in contact guidance of bone-forming cells on anisotropic Ti6Al4V surfaces. *Acta Biomaterialia*. 2011;7(4):1890-1901. doi:10.1016/j.actbio.2010.11.035.

158. Rajnicek AM, Foubister LE, McCaig CD. Prioritising guidance cues: Directional migration induced by substratum contours and electrical gradients is controlled by a rho/cdc42 switch. *Developmental Biology*. 2007;312(1):448-460. doi:10.1016/j.ydbio.2007.09.051.

159. Rajnicek AM, Foubister LE, McCaig CD. Alignment of corneal and lens epithelial cells by co-operative effects of substratum topography and DC electric fields. *Biomaterials*. 2008;29(13):2082-2095. doi:10.1016/j.biomaterials.2008.01.015.

160. Lämmermann T, Sixt M. Mechanical modes of “amoeboid” cell migration. *Current Opinion in Cell Biology*. 2009;21(5):636-644. doi:10.1016/j.ceb.2009.05.003.

161. Anselme K, Davidson P, Popa AM, Giazzon M, Liley M, Ploux L. The interaction of cells and bacteria with surfaces structured at the nanometre scale. *Acta Biomaterialia*. 2010;6(10):3824-3846. doi:10.1016/J.ACTBIO.2010.04.001.

162. Dalby MJ, Riehle MO, Sutherland DS, Agheli H, Curtis ASG. Use of nanotopography to study mechanotransduction in fibroblasts – methods and perspectives. *European Journal of Cell Biology*. 2004;83(4):159-169. doi:10.1078/0171-9335-00369.

163. Tayalia P, Mendonca CR, Baldacchini T, Mooney DJ, Mazur E. 3D cell-migration studies using two-photon engineered polymer scaffolds. *Advanced Materials*. 2008;20(23):4494-4498. doi:10.1002/adma.200801319.

164. Richter B, Hahn V, Bertels S, et al. Guiding Cell Attachment in 3D Microscaffolds Selectively Functionalized with Two Distinct Adhesion Proteins. *Advanced Materials*. 2017;29(5):1604342. doi:10.1002/adma.201604342.

165. Song KH, Park SJ, Kim DS, Doh J. Sinusoidal wavy surfaces for curvature-guided migration of Tlymphocytes. *Biomaterials*. 2015;51:151-160. doi:10.1016/j.biomaterials.2015.01.071.

166. Wolf K, Müller R, Borgmann S, Bröcker E-B, Friedl P. Amoeboid shape change and contact guidance: T-lymphocyte crawling through fibrillar collagen is independent of matrix remodeling by MMPs and other proteases. *Blood*. 2003; 102(9):3262-3269. doi:10.1182/blood-2002-12-3791.

167. Guvendiren M, Yang S, Burdick JA. Swelling-Induced surface patterns in hydrogels with gradient crosslinking density. *Advanced Functional Materials*. 2009;19(19):3038-3045. doi:10.1002/adfm.200900622.

168. Yang P, Baker RM, Henderson JH, Mather PT. In vitro wrinkle formation via shape memory dynamically aligns adherent cells. *Soft Matter*. 2013;9(18):4705. doi:10.1039/c3sm00024a.

169. Lam MT, Sim S, Zhu X, Takayama S. The effect of continuous wavy micropatterns on silicone substrates on the alignment of skeletal muscle myoblasts and myotubes. *Biomaterials*. 2006;27(24):4340-4347. doi:10.1016/j.biomaterials.2006.04.012.

170. Lee J, Chung S, Song H, Kim S, Hong Y. Lateral-crack-free, buckled, inkjet-printed silver electrodes on highly pre-stretched elastomeric substrates. *Journal of Physics D: Applied Physics*. 2013;46(10):105305. doi:10.1088/0022-3727/46/10/105305.

171. Brau F, Vandeparre H, Sabbah A, Poulard C, Boudaoud A, Damman P. Multiple-length-scale elastic instability mimics parametric resonance of nonlinear oscillators. *Nature Physics*. 2011;7(1):56-60. doi:10.1038/nphys1806.

172. Mirabella T, Macarthur JW, Cheng D, et al. 3D-printed vascular networks direct

therapeutic angiogenesis in ischaemia. *Nature Biomedical Engineering*. 2017;1(6): 0083. doi:10.1038/s41551-017-0083.

173. Dewey CF, Bussolari SR, Gimbrone MA, Davies PF. The Dynamic Response of Vascular Endothelial Cells to Fluid Shear Stress. *Journal of Biomechanical Engineering*. 1981;103(3):177. doi:10.1115/1.3138276.

174. Kassab GS. Scaling laws of vascular trees: of form and function. *AJP: Heart and Circulatory Physiology*. 2005;290(2):H894-H903. doi:10.1152/ajpheart.00579.2005.

175. Haruguchi H, Teraoka S. Intimal hyperplasia and hemodynamic factors in arterial bypass and arteriovenous grafts: a review. *Journal of Artificial Organs*. 2003;6(4): 227-235. doi:10.1007/s10047-003-0232-x.

176. Wolberg AS, Rosendaal FR, Weitz JI, et al. Venous thrombosis. *Nature Reviews. Disease Primers*. 2015;1:15006. doi:10.1038/nrdp.2015.6.

177. Giacca M, Zacchigna S. VEGF gene therapy: therapeutic angiogenesis in the clinic and beyond. *Gene Therapy*. 2012;19(6):622-629. doi:10.1038/gt.2012.17.

178. Simons M, Annex BH, Laham RJ, et al. Pharmacological treatment of coronary artery disease with recombinant fibroblast growth factor-2: double-blind, randomized, controlled clinical trial. *Circulation*. 2002;105(7):788-793. doi:10.1161/HC0802.104407.

179. Henry TD, Annex BH, McKendall GR, et al. The VIVA trial: Vascular endothelial growth factor in ischemia for vascular angiogenesis. *Circulation*. 2003;107(10): 1359-1365. doi:10.1161/01.CIR.0000061911.47710.8A.

180. Au P, Tam J, Fukumura D, Jain RK. Bone marrow derived mesenchymal stem cells facilitate engineering of long-lasting functional vasculature. *Blood*. 2008; 111(9):4551-4558. doi:10.1182/blood-2007-10-118273.

181. Chaturvedi RR, Stevens KR, Solorzano RD, et al. Patterning Vascular Networks In Vivo for Tissue Engineering Applications. *Tissue Engineering Part C: Methods*. 2015;21(5):509-517. doi:10.1089/ten.tec.2014.0258.

182. Weiss P. Experiments on cell and axon orientation in vitro: The role of colloidal exudates in tissue organization. *Journal of Experimental Zoology*. 1945;100(3): 353-386. doi:10.1002/jez.1401000305.

183. Tinevez JY, Perry N, Schindelin J, et al. TrackMate: An open and extensible platform for single-particle tracking. *Methods*. 2017;115:80-90. doi:10.1016/j.ymeth.2016.09.016.

184. Schindelin J, Arganda-Carreras I, Frise E, et al. Fiji: An open-source platform for biological-image analysis. *Nature Methods*. 2012;9(7):676-682. doi:10.1038/nmeth.2019.

185. Sarkaria JN, Tibbetts RS, Busby EC, Kennedy AP, Hill DE, Abraham RT. Inhibition of phosphoinositide 3-kinase related kinases by the radiosensitizing agent wortmannin. *Cancer Research*. 1998;58(19):4375-4382.

186. Nakanishi S, Kakita S, Takahashi I, et al. Wortmannin, a microbial product inhibitor of myosin light chain kinase. *Journal of Biological Chemistry*. 1992; 267(4):2157-2163.

CURRICULUM VITAE